Energy Flow and Rapidity Gaps Between Jets in Photoproduction

Angela Wyatt

October 2001

THE UNIVERSITY
of MANCHESTER

Particle Physics Group
Department of Physics and Astronomy

A thesis submitted to The University of Manchester for the degree of
Doctor of Philosophy in the Faculty of Science and Engineering

Contents

Abstract

Data from the H1 detector at HERA have been used to study photoproduction events which have two or more jets. The data were taken in 1996 and correspond to an integrated luminosity of $6.63\,\mathrm{pb}^{-1}$. Events were studied in the photon-proton centre of mass energy range 165 GeV $< W <$ 243 GeV and with $Q^2 < 0.01$ GeV^2. Jets were defined using the longitudinally invariant k_t algorithm. Events selected had one jet with $P_T > 6$ GeV and a second with $P_T > 5$ GeV; these jets were required to have a pseudorapidity separation of $2.5 < \Delta\eta < 4.0$.

The cross section was measured differentially in $\Delta\eta$; x_p^{jets}, the fraction of the proton's momentum entering the hard scatter; x_γ^{jets}, the fraction of the photon's momentum entering the hard scatter; and E_T^{gap}, the sum of the transverse energy between the two highest P_T jets. Rapidity gap events were defined as events in which $E_T^{gap} < E_T^{cut}$, where the parameter E_T^{cut} was varied in the range $0.5 < E_T^{cut} < 2.0$ GeV. The cross section for rapidity gap events and the gap fraction, defined as the fraction of dijet events with a rapidity gap, were measured differentially in $\Delta\eta$, x_p^{jets}, and x_γ^{jets}.

An excess of events with a rapidity gap is observed over that expected from standard photoproduction processes. This excess can be explained as a result of the exchange of a strongly interacting colour singlet object between the jets. There are large theoretical uncertainties in the predictions from the photoproduction models, and the data currently show little sensitivity to the underlying dynamics of the exchange. However, the data can be described by the exchange of the leading logarithmic approximation of the BFKL pomeron, with a choice of $\alpha_s = 0.18$. This is consistent with the gap fraction observed at the Tevatron in $p\bar{p}$ collisions at 1800 GeV.

Declaration

No portion of the work referred to in this thesis has been submitted in support of an application for another degree or qualification of this or any other university or any other institute of learning.

This work was supported financially by the Particle Physics and Astronomy Research Council (P.P.A.R.C.) between October 1998 and September 2001.

Chapter 1

Introduction

In the standard model, the strong force is described by the gauge theory quantum chromodynamics, QCD. The value of the coupling constant of QCD, α_s, depends on the energy scale of the interaction. It rises dramatically at energy scales smaller than $\Lambda_{\rm QCD}$ or, equivalently, at large distance scales. This property of the coupling constant leads to the confinement of quarks into colourless hadrons. Perturbative calculations can only be made when α_s is sufficiently small, that is, when a hard scale is present.

Perturbative QCD (pQCD) has been very successful in describing short distance physics. Total hadronic cross sections, however, are dominated by long distance physics. These can be successfully described by the phenomenological model of Regge theory. At high energies the total cross section is dominated by the diffractive exchange of an object with the quantum numbers of the vacuum, the pomeron.

Diffractive events are characterised by large rapidity gaps in the hadronic final state, due to the colour singlet exchange. The study of these events in the presence of a hard scale enables a perturbative approach to be taken. Events with a rapidity gap between two jets have a hard scale at both ends of the exchange, the large momentum transfer. The gap production mechanism itself is then dominated by

short distance physics. Hence, these events prove an interesting area in which to use pQCD to understand the pomeron and are the subject of the analysis in this thesis. Existing measurements of this process use rapidity gap definitions which have some theoretical and experimental problems. An alternative definition is used here which is able to overcome some of these problems.

Photoproduction data taken in 1996 by the H1 detector at HERA are analysed. Differential dijet cross section measurements are made for an inclusive data sample and for subsets of events that have a rapidity gap between the jets. The ratio of these measurements, the gap fraction is also presented.

In chapter 2 the electron-proton (ep) collider, HERA and the H1 detector are described, with an emphasis placed on those detector components used to make the measurements presented. Chapter 3 discusses the relevant ep physics at H1, including topics such as deep inelastic scattering (DIS), photoproduction and jet physics. A review of diffraction is given in chapter 4 which sets in context the motivation for this analysis. This concludes with the definition of a rapidity gap event that is used in this thesis. The full event selection procedure is given in chapter 5. Chapter 6 then describes the correction procedure used to determine the cross section measurements. In chapter 7 the measurements are presented and discussed. Finally, a summary of the results and an outlook are given.

Chapter 2

The H1 Detector at HERA

The H1 detector [1] is one of two experiments used to study electron-proton collisions in the Hadron-Electron Ring Accelerator, HERA, at the DESY laboratory in Hamburg. In this chapter a brief description of HERA and the layout of the H1 detector are given. The detector components are then described in more detail, with emphasis on those components relevant to the measurements presented in this thesis.

2.1 The Hadron-Electron Ring Accelerator

HERA, the world's first electron[1]-proton collider, is composed of two separate storage rings of 6.3 km circumference. In these rings electrons and protons are accelerated to 27.6 GeV and 820 GeV respectively[2]. The beams are brought into collision at two interaction points, where the H1 and ZEUS detectors are located. The electron-proton centre of mass energy is 300 GeV, a factor of 10 higher than that of previous *ep* scattering experiments which used fixed targets. Two further

[1]HERA can run with either electrons or positrons, in this thesis no distinction need be made, and the beam is always referred to as the electron beam.

[2]Since 1998 the proton beam energy has been 920 GeV.

experiments, HERMES and HERA-B are also situated on the HERA ring. HERMES collides the polarised electron beam with polarised gas targets (H_2, D, ^{3}He and ^{4}He) to study the spin structure of nucleons. HERA-B inserts fixed wire targets into the edge of the proton beam to investigate CP violation through the study of the $B^0 - \bar{B}^0$ system.

The electrons and protons are stored in around 170 colliding bunches with typical currents of 20 mA of electrons and 60 mA of protons. The bunch crossing interval is 96 ns. Some bunches are left empty so that an electron or proton bunch may arrive at the interaction point alone. These pilot bunches enable the background from interactions between the beam and residual gas (beam-gas) and from interactions between the beam and the beam pipe (beam-wall) to be estimated.

2.2 The H1 Detector

The main physics aims of H1 are to measure the structure of the proton, to study fundamental interactions between particles and to search for physics beyond the Standard Model. This has led to the design of a detector with good identification of leptons, particularly the scattered electron, and an excellent hadronic calorimeter with high resolution for jets and good hermeticity to recognize missing transverse energy.

The H1 detector is shown in figure 2.1. Tracking devices (see section 2.4) surround the interaction point and outside these are the calorimeters (see section 2.3). A superconducting solenoid provides a 1.15 T magnetic field. The detector is then enclosed in iron, which acts as the return yoke for the magnetic field and is instrumented for further particle detection. In front of the iron is the forward muon detector (see section 2.5). Further instrumentation to detect particles scattered at very low angles is situated further down the beam pipe and is not shown in figure 2.1.

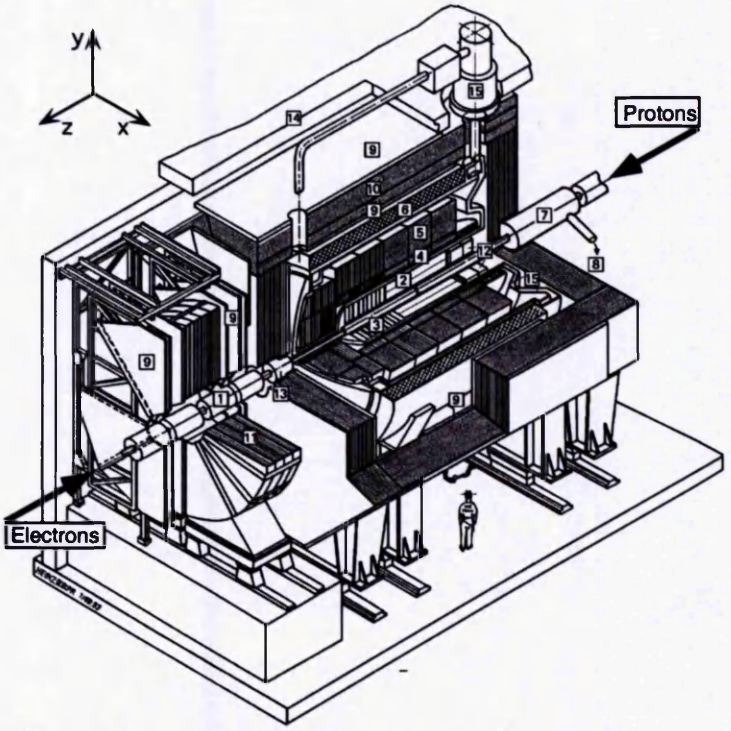

Figure 2.1: The H1 Detector.

A sophisticated trigger system (see section 2.8) is implemented to distinguish *ep* collisions from the very high rate of background events from beam-gas and beam-wall interactions.

To describe points within the detector, a right-handed Cartesian coordinate system (x, y, z) is used in which the origin is defined by the nominal interaction point, the positive z direction[3] by the incoming proton beam direction and the positive

[3]The positive z direction is also referred to as the forward direction.

y direction as vertically upwards. A spherical coordinate system (r, θ, ϕ) is defined with reference to this such that $\theta = 0°$ corresponds to the positive z direction and $\phi = 0°$ corresponds to the positive x direction. It is also useful to define the pseudo-rapidity of a particle, η:

$$\eta = -\ln \tan\left(\frac{\theta}{2}\right) \tag{2.1}$$

which approximates to its true rapidity, Y,

$$Y = \frac{1}{2}\ln\left(\frac{E + P_z}{E - P_z}\right) \tag{2.2}$$

in the limit that the mass is zero, where E is the energy and P_z is the longitudinal momentum of the particle.

2.3 Calorimeters

The H1 calorimeter system consists of four calorimeters: the liquid argon (LAr) calorimeter, the SpaCal, the PLUG calorimeter and the tail catcher. Only data from the LAr calorimeter and the SpaCal are used in this thesis and these detectors are described in the following sections. The PLUG calorimeter closes the gap between the edge of the LAr calorimeter and the beam pipe ($0.6° < \theta < 3.5°$). It consists of nine copper absorbing plates alternating with eight sampling layers of silicon and can be used to veto forward activity and minimise the unmeasured total transverse momentum. The magnet return yoke is instrumented with limited streamer tubes (the tail catcher) and can be used to provide a very coarse measurement of the energy of hadronic showers leaking out of the LAr calorimeter.

2.3.1 The Liquid Argon Calorimeter

The main calorimeter at H1 is the liquid argon calorimeter [2]. Its main purposes are the measurement of scattered electrons in high Q^2 ($> 100\,\mathrm{GeV}^2$) events[4] and

[4] Q^2 is the 4-momentum transferred in the ep collision, and is discussed further in section 3.1.

measuring the energy of the hadronic final state. It is fully hermetic in ϕ and covers the range $4° < \theta < 154°$ (3.35> η > -1.43). The LAr calorimeter consists of an electromagnetic calorimeter (EMC) and a hadronic calorimeter (HAC) contained within a single liquid argon cryostat. To reduce the amount of dead material that particles pass through before reaching the calorimeter, the LAr calorimeter is within the solenoid magnet. The LAr calorimeter comprises eight wheels each divided into octants. The most backward wheel has only an electromagnetic calorimeter.

The LAr calorimeter is a sampling calorimeter; it is constructed from plates of absorber material separated by gaps filled by a sampling material, liquid argon. A high voltage is placed across the gaps and readout pads are placed on the grounded side. An incident particle interacts with the absorber material producing a shower of particles. Electromagnetic particles (electrons and photons) interact via pair production and bremsstrahlung processes. Hadrons interact via elastic and inelastic scattering with the nuclei of the material. The particles produced also interact and this cascade process produces a shower of particles. The energy of the shower is converted into a signal by the sampling material. Charged particles from the shower ionise the argon atoms and the number of ionised particles produced is proportional to the shower energy. The charge produced is collected at the electrodes and read out.

Liquid argon is used as the sampling material because its high atomic density results in large ionisation. Argon is also a noble gas and this reduces the probability of inelastic collisions between the argon atoms and the ionised particles so that a lower voltage is required. The EMC is made from thin (2.4 mm) lead plates; the gaps between the plates are of similar size. The HAC is made from 19 mm steel plates with gaps of 5 mm between them. Electrons and photons will lose almost all their energy in the thin layers of the EMC; hadrons are only absorbed in the much thicker plates of the HAC.

The thickness of the EMC varies from $\sim$30 radiation lengths in the forward direction

to ~20 radiation lengths in the backward direction. The total thickness of the EMC and HAC varies from 8 interaction lengths in the forward direction to 5 interaction lengths in the backward direction. These parameters reflect the larger particle multiplicities in the forward direction.

There are around 45,000 readout channels. The granularity is optimised to provide fine and approximately uniform segmentation in η and ϕ. This high segmentation enables noise to be reduced. The fine granularity of the LAr calorimeter also allows the shower shapes of electrons and hadrons to be distinguished, resulting in an e/π discrimination better than one part in a thousand [3]. The channels are combined into 256 towers which point towards the nominal interaction point. The summation of energy in each tower is used for the LAr calorimeter trigger.

The LAr calorimeter is a non-compensating calorimeter, i.e. its response to electromagnetic and hadronic particles is different. The charge output from hadrons is around 30% less than that from electrons of the same energy. The majority of this 'invisible' energy is lost to nuclear excitation or break-up in the absorber. Hence, an additional correction is applied to hadronic clusters in their reconstruction [4].

The energy resolution of the LAr calorimeter has been measured using test beams. The energy[5] resolution of the EMC for electrons is $\frac{\sigma(E)}{E} \sim \frac{0.12}{\sqrt{E}} \oplus 0.01$ [5] and the resolution for pions in both sections is $\frac{\sigma(E)}{E} \sim \frac{0.50}{\sqrt{E}} \oplus 0.02$ [6]. The electromagnetic energy scale is determined with an uncertainty of 1.5% [7] by comparing the energy measurement of the scattered electron in ep events with the corresponding track momentum. The transverse momentum balance between the hadronic final state and the scattered electron in high Q^2 events enables the hadronic energy scale to be measured and this is known to 4% [8] for measurements of exclusive final states.

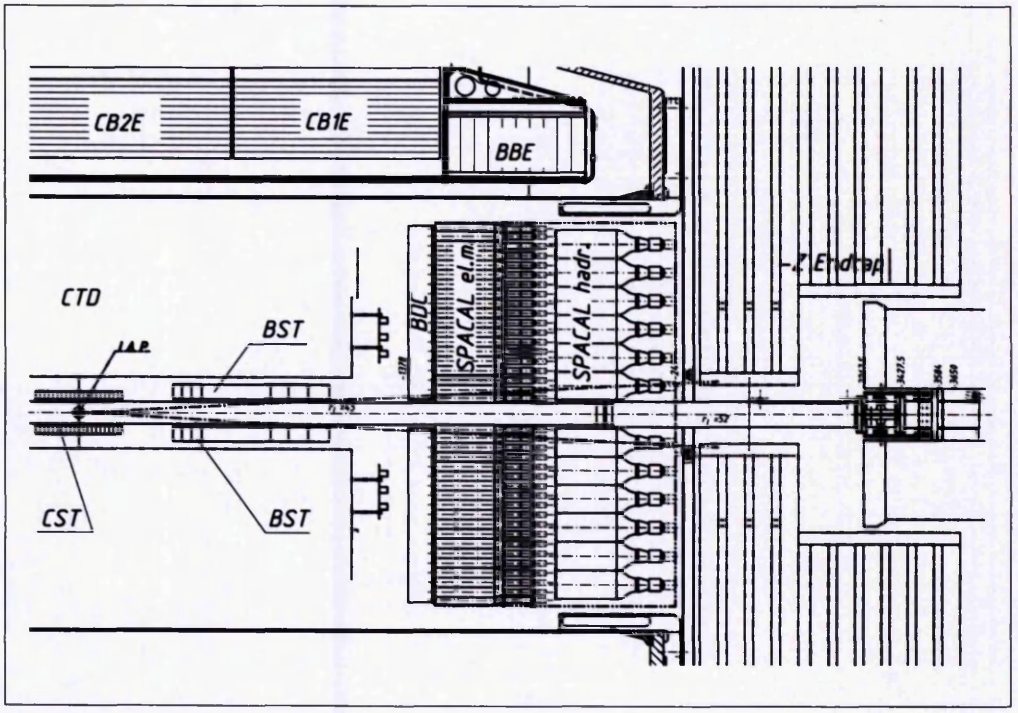

Figure 2.2: A side view of the backward part of the H1 detector, showing the location of the SpaCal.

2.3.2 The SpaCal

The backward region of the H1 detector, 153° < θ < 177.5° (-1.43 < η <-3.82), is covered by the SpaCal [9]. This is a lead-scintillating fibre or "spaghetti" calorimeter. It provides good coverage of the region near the beam pipe. The SpaCal provides precision measurements of the scattered electron in DIS events ($1 \lesssim Q^2 \lesssim 100$ GeV^2). Measurements of hadronic energy, including that in jets, are also possible, although these are less precise than measurements made using the LAr calorimeter. In addition, the SpaCal is able to veto beam-gas and beam-wall background events originating up-stream in the proton beam direction by providing time of flight (TOF) information. The TOF difference between these events and those originating at the nominal interaction point is ~10 ns. The time resolution is better than 1 ns.

[5] All measurements of energy in this thesis are in GeV unless otherwise stated.

The position of the SpaCal within the backward part of the H1 detector is shown in figure 2.2. The separation into an electromagnetic (EM) and hadronic calorimeter allows the resolution for detecting scattered electrons to be optimised while maintaining good detection of hadronic particles. Comparison of energy deposits in the two sections improves the e/π discrimination, which is better than one part in one hundred [10].

The SpaCal is constructed from grooved lead sheets, the grooves contain scintillating fibres. The incident particles produce showers of particles in the lead and these particles cause the fibres to scintillate. The light from the fibres is read out by photo-multiplier tubes. This provides the fast timing required. The fibre diameter is small (0.5 mm in the EM section and 1.0 mm in the hadronic section) which enables a high sampling frequency to be obtained. The active volume of each section is 250 mm deep; this corresponds to 28 radiation lengths for the EM section and each section is one hadronic interaction length deep. There are 1192 readout channels in the EM section and 136 hadronic readout channels. This difference reflects the larger cell size needed to contain hadronic showers.

From test beam measurements the energy resolution of the electromagnetic section is $\frac{\sigma(E)}{E} \sim \frac{0.07}{\sqrt{E}} \oplus 0.01$ [11]. The hadronic section has an energy resolution of $\frac{\sigma(E)}{E} \sim \frac{0.56}{\sqrt{E}} \oplus 0.03$ for pions and of $\frac{\sigma(E)}{E} \sim \frac{0.13}{\sqrt{E}} \oplus 0.04$ for electrons [12]. The absolute hadronic scale is measured by comparing the energy response to individual hadronic particles with the particle momentum measured in the CJC and by comparison of the data with the simulation of energy flow [13].

2.4 The Tracking System

The H1 tracking system is shown in figure 2.3. Measurements of charged particle tracks and the interaction vertex are provided by the central and forward tracking

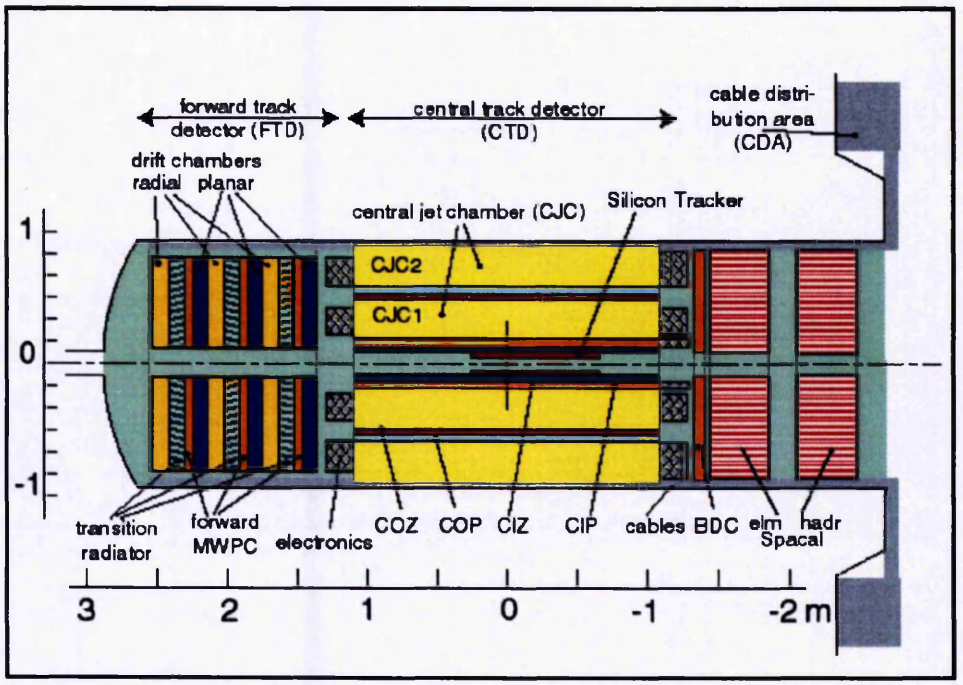

Figure 2.3: A longitudinal view of the H1 tracking system.

systems. These cover the region $7° < \theta < 165°$ and are in the magnetic field, which is parallel to the z axis. Each system is constructed from both drift chambers and multi-wire proportional chambers (MWPCs). A backward drift chamber is also mounted on the front of the SpaCal. There are also two silicon trackers, the CST and BST. Only the central and forward trackers are used in this thesis. The forward tracker is only used for vertex information.

A drift chamber consists of a large number of cells. Each cell is filled with a gas and is subject to a roughly uniform electric field. The electric field is formed by a series of cathode field wires and anode sense wires plus additional field shaping wires. A charged particle entering the cell will ionise the gas. The electrons produced travel at a constant, well known, velocity towards the anode sense wires. At distances close (< 1 mm) to the sense wires the electric field increases dramatically, resulting in a cascade of secondary ionisation. The movement of the produced ions away from the anode induces a current in the wire. The signal is amplified and read out.

The timing of a current pulse from a wire gives the time taken for the primary ionisation to reach the wire and hence the distance of closest approach of the particle to the wire; this has a resolution of a few hundred μm. The signal is read out at both ends of the sense wire and the relative timing of the pulses enables the position of the ionisation along the wire to be known; a resolution of 1% of the wire length is achieved. From the space points determined from the sense wires a particle's track can be found. The curvature of the track in the magnetic field allows the particle's momentum to be determined. Particle identification is also possible by measuring the rate of energy lost with distance travelled ($\mathrm{d}E/\mathrm{d}x$).

A MWPC is based on similar principles to the drift chamber except that there are no drift regions. The cathode is formed by a series of pads around the outside of the cell and the anode wires are very close together ($\sim$ 2 mm) so that the avalanche regions of the wires overlap. Rapid amplification of the initial ionisation occurs, inducing a charge on the sense wire proportional to the initial ionisation. The spatial resolution is limited to the distance between the wires but the short drift time enables the signal to be read out very quickly, providing information for triggering purposes.

2.4.1 The Central Tracking Detector

The central tracking detector (CTD) covers the region $15° < \theta < 165°$ and is shown in cross section in figure 2.4.

The main components are two large concentric drift chambers: the inner central jet chamber (CJC1) and the outer central jet chamber (CJC2) [14]. Each has the plane of sense wires parallel to the z axis, giving the best measurement in the $r - \phi$ plane, with a drift time resolution of 170 μm. Each cell is inclined at 30° to the radial direction so that even stiff tracks will pass through several cells. The z resolution of 2.2 cm, from charge division techniques, is poorer than the $r - \phi$ resolution.

To improve the measurement in the z direction two further drift chambers are used:

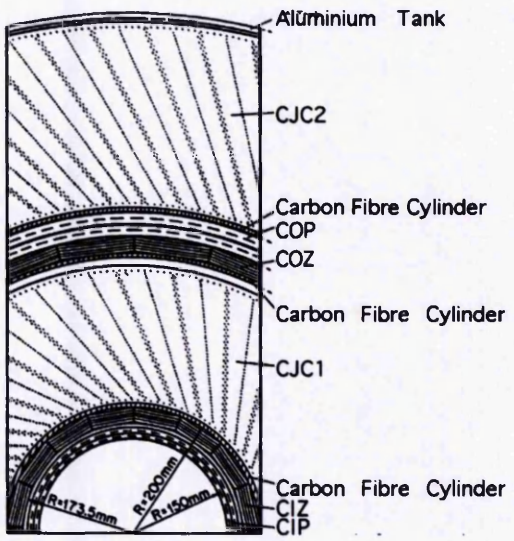

Figure 2.4: A section through the $r-\phi$ plane of the central tracking detector.

the central inner z chamber (CIZ) and the central outer z chamber (COZ) [15]. Their positions are shown in figure 2.4. In these chambers the sense wires are azimuthal and the electric field is in the z direction. The z coordinate can be measured with a resolution of ~ 350 μm.

Tracks are mainly reconstructed from $r-\phi$ information from CJC1 and CJC2 and z information from the CIZ and COZ. Tracks are constrained by imposing a common interaction vertex; tracks that fail this are assigned to secondary vertices or background sources. The z position of the vertex can be found with a resolution of around 3 mm. The combined track measurements give a momentum resolution of $\sigma_p/p^2 \sim 3 \times 10^{-3}$ GeV^{-1}.

The CTD also contains two MWPCs, the central inner proportional chamber (CIP) and the central outer proportional chamber (COP) [16]. They are not used in the track measurement but provide fast timing information for triggering. Their position is shown in figure 2.4. Both consist of double layers of drift chambers with wires

parallel to the z-axis. They are the main detectors used in the z-vertex trigger, which is described in section 2.8.1.

2.4.2 The Forward Tracking Detector

The forward tracking detector (FTD) [17] covers the region $7° < \theta < 25°$. It is made up of three identical 'supermodules'. Each supermodule consists of planar drift chambers, a section of MWPCs, transition radiators and radial drift chambers.

2.5 The Muon Detectors

The iron return yoke of the solenoid is instrumented with limited streamer tubes, as used in the Tail Catcher. Muons escape the main calorimeter and their tracks are reconstructed from their hit patterns in the streamer tubes with an efficiency of greater than 90% for muon energies above 2 GeV. In the forward direction muon detection is provided by the forward muon detector (FMD) [18] which comprises of drift chambers and a toroidal magnet. The toroidal field is necessary for good momentum resolution of muons with a small transverse momentum. The FMD is also used in a variety of analyses to tag the products of proton dissociation.

2.6 The Time of Flight System

At HERA the rate of background events from proton beam-wall and beam-gas interactions is considerably higher than that of beam-beam collisions. The time of flight system provides timing information that can be used to veto these backgrounds. Particles produced in a beam-beam collision will arrive at the TOF detectors at a different time than particles produced in up stream or down stream background collisions.

The TOF system is comprised of a number of plastic scintillators, which are used because of their good time resolution. These are situated between the SpaCal and the backward iron end-cap, near the FMD and within the PLUG calorimeter. In addition a double set of scintillators backward of the iron return yoke (the 'veto wall') detects particles (mainly muons) from the proton beam-halo. The SpaCal is also used to provide TOF information.

2.7 The Luminosity System

The luminosity system provides the information required to calculate the luminosity and hence is essential for the accurate determination of any cross section. The system comprises two components, both situated along the beam line: an electron tagger positioned at $z = -33.4$ m and a photon tagger at $z = -102.9$ m.

The 33 m electron tagger and the photon detector are both TlCl/TlBr crystal calorimeters. They are both 22 radiation lengths deep and have an energy resolution of $\frac{\sigma(E)}{E} \sim \frac{0.10}{\sqrt{E}} \oplus 0.01$. The photon detector is shielded from synchrotron radiation by a lead filter and a veto water Cerenkov detector.

The luminosity is calculated from the measured rate of the Bethe-Heitler process [19] ($ep \to ep\gamma$). The cross section for this process has been calculated precisely within QED and is known to 0.5%. The measurement is made on-line from the rate of coincidence signals in the electron and photon taggers. The sum of the energy of the detected electron and photon is required to be close to that of the electron beam. The rate is corrected for background processes and the detector acceptance to give the on-line luminosity used to steer the beams. The main background source is bremsstrahlung of electrons in the vicinity of residual gas particles and this can be measured using pilot bunches.

The electrons are deflected into the tagger by the HERA beam magnets. Hence, the

acceptance for their detection depends critically on the beam optics and position of the interaction point, which can vary from run to run.

The luminosity is also calculated off-line from the measured rate of scattered photons only [20]. This removes the uncertainty of the electron tagger acceptance. The luminosity is also corrected for the contribution from protons in satellite bunches. The uncertainty on the measured luminosity for the data taking period used in this thesis is 2% [21].

The 33m electron tagger is also used to detect low Q^2 (< 0.01 GeV^2) electrons which are scattered through small angles. There are additional electron taggers at 8 m and 44 m which cover different scattered electron energy ranges but are not used in this thesis.

2.8 Triggering and the Data Acquisition System

At HERA a bunch crossing occurs every 96 ns while the readout times of the H1 subdetectors are considerably longer (up to $\sim$ 1.5 μs) and there are $\sim$ 270 000 readout channels. If every event was read out in full, these factors would result in an unacceptable dead time. To overcome this problem a pipelined trigger and readout system is used, illustrated in figure 2.5.

The trigger system consists of a number of levels, at each level a decision is made to keep or reject the information about an event. At level 1 (L1) the central trigger (CTL1) [22] receives groups of 'trigger elements' from the majority of the H1 subdetectors. It takes up to 24 bunch crossings for the trigger elements to be read out and a L1 decision to be made. During this time the detector information is stored in a 'pipeline' while the trigger information is processed so new data can continue to be recorded and the process remains free of dead-time.

The L1 decision is made based on 128 combinations of the $\sim$ 200 trigger elements

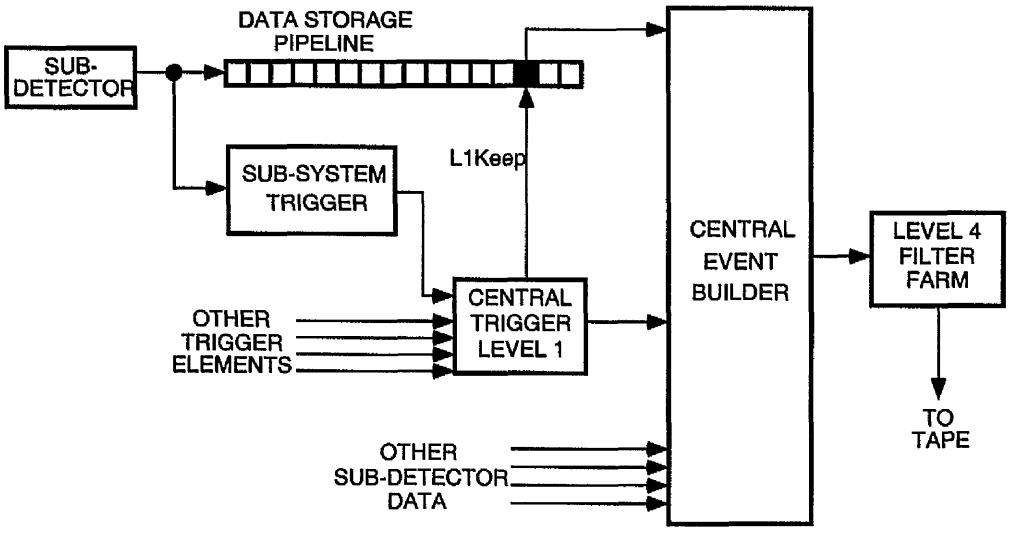

Figure 2.5: A schematic view of the H1 trigger and data acquisition system. L2 is not shown.

called subtriggers. If the requirements of at least one subtrigger are met then a L1-keep signal is set. The subtriggers combine trigger elements that veto background events with those that select physics events. In addition to physics subtriggers some subtriggers are used to monitor backgrounds and trigger efficiencies. These subtriggers, plus other subtriggers with particularly high rates, may be prescaled, that is a L1-keep decision will only be made for a certain, pre-programmed fraction of the events that pass the subtrigger.

If an L1-keep signal is sent then the data taking process is stopped and the full event information from the pipeline is readout and sent to the Central Event Builder (CEB). This process lasts up to $\sim 1-2$ ms and during this dead-time no new events can be recorded. The background event rate of more than 10 kHz is reduced to an event rate of around 40 Hz, while resulting in a dead-time of about 10%.

Some subtriggers have further level 2 (L2) conditions. The L2 trigger is made up of two sections, the topological trigger (L2TT) and the neural network trigger (L2NN). They receive more information from the trigger sub-systems and can make

more complex, but slower, decisions than L1. A decision takes around 20 μs and if the event is rejected, the data readout process can then be interrupted and the pipelines unfrozen.

When all the event information has been read into the CEB the period of dead-time ends. The level 4 (L4) trigger runs on a PC farm performing detailed event processing and rejects the vast majority of remaining background events. Events passing the L4 trigger are written to tape at a rate of approximately $\sim$ 10 Hz and have an average size of 130 KBytes. These events are then processed off-line using the full reconstruction code and classified into one or more physics classes, this is known as level 5.

The main trigger elements that form the subtriggers used in this thesis are described in the following sections.

2.8.1 The z-Vertex Trigger

Demanding that the reconstruction of the event vertex is within the interaction region eliminates the majority of the background from beam-gas and beam-wall events. The z-vertex trigger [23] reconstructs the vertex from signals from the MWPCs of the CIP and COP and the planar MWPC in the first forward tracker supermodule (FPC) and sends this information to the L1 trigger.

The detector is divided into 16 ϕ segments. Within each segment coincident hits in two out of the three chambers, typically with hits in four pads, are used to construct straight lines, called rays. The z coordinate of the intercept of each ray with the z axis is binned in a histogram of 16 bins of 5.4 cm. The histograms from each segment are combined to form the z vertex histogram. For an ep event with a vertex in the nominal region there will be a peak in the histogram, over the background from wrongly constructed rays, which corresponds to the vertex position. This is illustrated in figure 2.6.

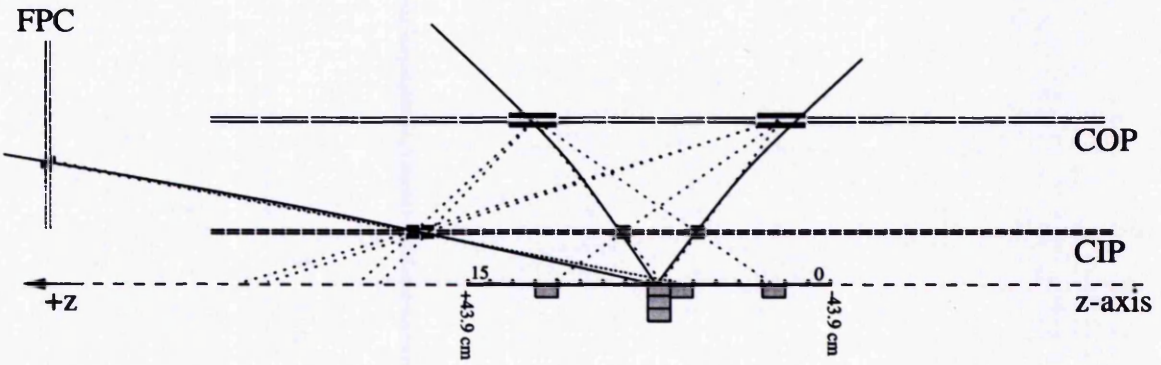

Figure 2.6: A schematic representation of the filling of the z-vertex histogram. All possible rays for the hit pattern are shown. The true rays are shown in bold and are linked to the significant z-vertex histogram peak.

The z vertex histogram can be used to define a number of L1 trigger elements. The zVtx_T0 element demands at least one ray and is used for bunch crossing identification in most subtriggers. The zVtx_sig element is set when there is a significant peak in the histogram above background in the interaction region.

2.8.2 The DCRΦ Trigger

The DCRΦ trigger provides simple tracking information. It uses data from CJC1 and CJC2, making decisions based on look-up tables which relate drift times to track momentum and position. A number of trigger elements are available based on different track numbers and charges.

2.8.3 The SpaCal Inclusive Electron Trigger

The SpaCal inclusive electron trigger only demands an electromagnetic cluster in the SpaCal. It requires a deposit of energy, summed over a 4×4 cell area, within

the TOF window for an *ep* interaction. Three trigger elements are available, each of which has a different cluster energy threshold. The element used in this thesis, IET>1, has a threshold energy of 2 GeV.

2.9 Monte Carlo Simulation

The data measured by the H1 detector must be corrected for the detector acceptance and smearing effects in order to produce results which can be compared to theoretical predictions and data from other experiments. In order to do this a GEANT3 [24] simulation of the effect of the H1 detector is used. The PYTHIA [25] and HERWIG [26] Monte Carlo event generators can be used to simulate the production of the complete final state of photoproduction events, producing a list of particles. This is referred to as the hadron or generator level of the simulation. The interaction of these particles in the detector and their reconstruction is then modelled, to give the detector or reconstructed level. The detector level simulation is directly comparable to the data and the simulation can be used to give the correction factors necessary to correct the data back to the hadron level. This method is used in the analysis presented in this thesis.

Chapter 3

HERA Physics

This chapter gives an introduction to the physics of ep scattering. In Deep Inelastic Scattering (DIS) the lepton is able to probe the structure of extended objects, such as the proton. This process has played a vital role in understanding the structure of matter. A brief review of DIS is given, with emphasis on those issues relevant to the HERA kinematic region. The photoproduction limit, in which the exchanged photon is real, is also discussed. Two further areas of specific relevance to this thesis-jet physics and multiple parton-parton interactions are also briefly outlined.

3.1 DIS Kinematics

A diagram of the generic neutral current (NC) DIS process at HERA, $ep \rightarrow eX$, is shown in figure 3.1. In this process the electron scatters off the proton via the exchange of a neutral electroweak gauge boson (a photon or Z^0). This boson couples to a single charged parton within the proton, and the scattered parton plus the proton remnant produce the hadronic final state, X.

The kinematics of a DIS event can be described using Lorentz scalars formed by

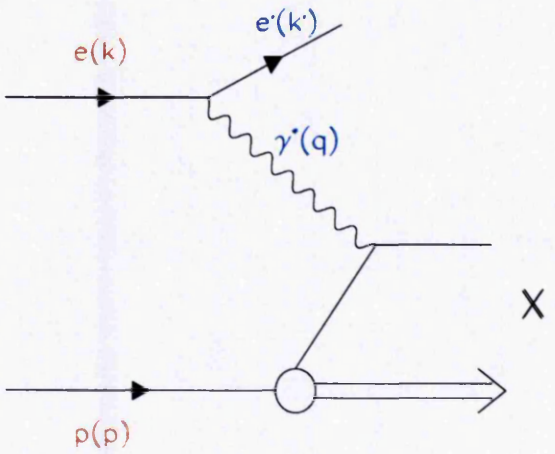

Figure 3.1: The neutral current deep-inelastic scattering process via photon exchange. The 4-vectors used to define the HERA kinematic variables are shown in parentheses.

combinations of the 4-vectors labelled in figure 3.1. The squared centre of mass energy of the *ep* system,

$$s = (k + p)^2 \tag{3.1}$$

is 90,200 GeV^2 for the data used in the analysis in this thesis. The square of the 4-momentum transferred

$$Q^2 = -q^2 = -(k - k')^2 \tag{3.2}$$

defines the virtuality of the photon and is used as a scale when studying DIS interactions. The dimensionless Bjorken scaling variable

$$x = \frac{Q^2}{2p \cdot q} \tag{3.3}$$

can be interpreted as the fraction of the proton's momentum carried by the struck parton in the limit that the parton is massless and carries no transverse momentum. The second Bjorken scaling variable

$$y = \frac{p \cdot q}{p \cdot k} \tag{3.4}$$

can be interpreted, in the proton rest frame, as the fraction of the electron energy carried by the exchanged boson. The invariant mass of the hadronic final state, W, is given by

$$W^2 = (q+p)^2 \tag{3.5}$$

At fixed s, neglecting the azimuthal degree of freedom, the kinematics of the inclusive scattering process can be completely described in terms of any two independent variables such as Q^2, W^2, x and y. These quantities are related, neglecting particle masses, by

$$Q^2 = sxy \tag{3.6}$$

$$W^2 = Q^2\left(\frac{1-x}{x}\right). \tag{3.7}$$

The influence of Z^0 boson exchange is negligible in comparison to photon exchange, except at high Q^2 ($Q^2 > 1000\,\mathrm{GeV}^2$), due to the high Z^0 mass. At $Q^2 = 2000\,\mathrm{GeV}^2$ and $x = 0.4$ the net influence of Z^0 exchange and γZ interference is a reduction in the e^+p cross section of about 30% [7]. The charged current (CC) DIS process $ep \to \nu_e X$ via $W^\pm$ exchange is around three orders of magnitude lower than the NC cross section at low Q^2, due to the large mass of the W boson. At the electroweak unification scale $Q^2 \gtrsim M_W^2, M_Z^2$ the NC and CC cross sections become similar [27].

3.2 The Structure of the Proton

The inclusive electromagnetic cross section for the process $ep \to eX$ may be expressed, to lowest order of QED, in terms of two[1] structure functions $F_1(x,Q^2)$ and $F_2(x,Q^2)$ which parameterise the charge distribution within the proton[2]:

$$\frac{\mathrm{d}^2\sigma_{ep\to eX}}{\mathrm{d}x\mathrm{d}Q^2} = \frac{4\pi\alpha_{em}^2}{xQ^4}\left[y^2xF_1(x,Q^2) + (1-y)F_2(x,Q^2)\right]. \tag{3.8}$$

[1]Where Z^0 exchange is significant a third, parity violating, structure function, $F_3(x,Q^2)$, is necessary to describe the complete neutral current process; see the measurement presented in [28].

[2]For a more detailed discussion see, for example, [29].

$F_1(x,Q^2)$ and $F_2(x,Q^2)$ are related to the structure functions for the scattering of transversely and longitudinally polarised photons, $F_T(x,Q^2)$ and $F_L(x,Q^2)$, by the following relations:

$$F_T(x,Q^2) = 2xF_1(x,Q^2) \tag{3.9}$$

$$F_L(x,Q^2) = F_2(x,Q^2) - 2xF_1(x,Q^2). \tag{3.10}$$

Equation 3.8 can be redefined as

$$\frac{\mathrm{d}^2\sigma_{ep\to eX}}{\mathrm{d}x\mathrm{d}Q^2} = \frac{2\pi\alpha_{em}^2 Y_+}{xQ^4}\left[F_2(x,Q^2) - \frac{y^2}{Y_+}F_L(x,Q^2)\right] \tag{3.11}$$

where $Y_+ = 1 + (1-y)^2$. The structure function $F_2(x,Q^2)$ is extracted from the measured inclusive DIS cross section using equation 3.11 after small corrections for QED radiation and estimating the contribution (if any) of F_L and Z^0 exchange. The contribution of F_L to the cross section is small and indeed negligible except at high y.[3] Measurements of $F_2(x,Q^2)$ using data from the H1 [27, 30], BCDMS [31] and NMC [32] experiments are shown in figure 3.2.

3.2.1 The Quark Parton Model

The first measurements of $F_2(x,Q^2)$ [33], made at values of $x \sim 0.2$, revealed the striking property of scaling or scale invariance [34], the feature that the structure function is approximately independent of Q^2 over a wide range of Q^2 values. This feature is clearly visible in figure 3.2(b). The Quark Parton Model (QPM) [35] was developed in response to this observation. In the QPM the proton is made up of non-interacting, point-like constituents called 'partons'. DIS is then viewed as incoherent elastic scattering between the electron and the charged partons, rather than scattering off the extended proton. The lack of a length scale involved, due to the point-like nature of partons, gives the scale invariance experimentally observed.

[3] F_L would be zero if the Quark Parton Model (section 3.2.1) were exact; this results from the fact that quarks have spin $\frac{1}{2}$.

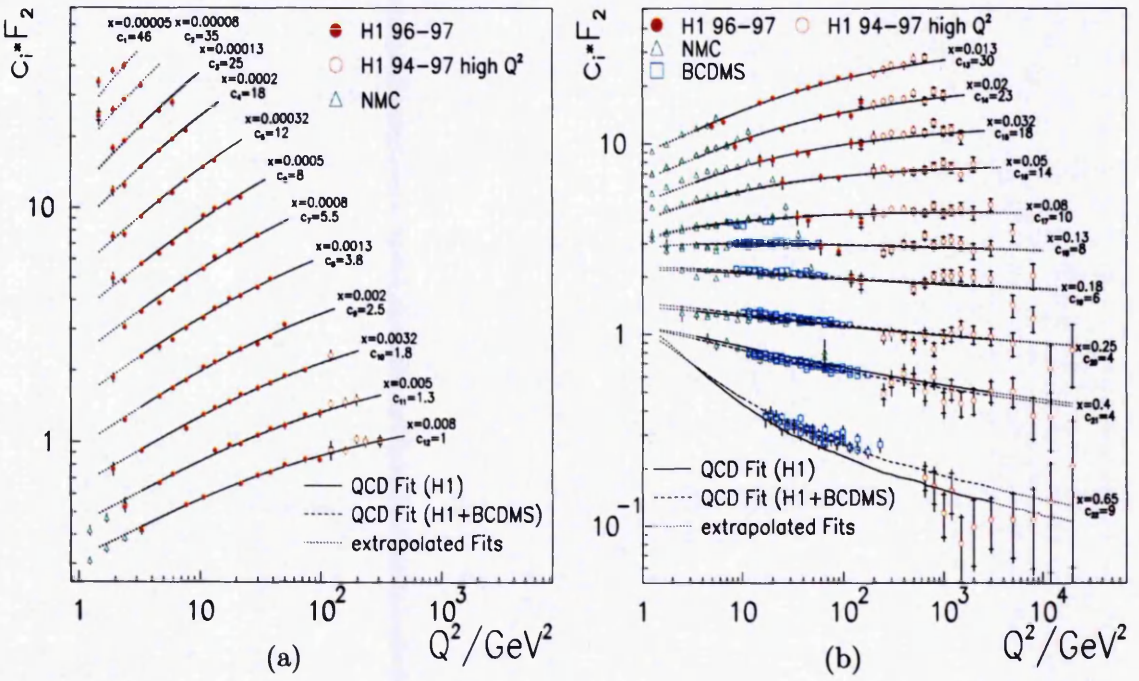

Figure 3.2: Measurements, by H1 and fixed target experiments, of the structure function $F_2(x, Q^2)$ as a function of Q^2 for a range of x values. The curves show NLO DGLAP QCD fits (see section 3.3.1) with different data sets. $c_i(x)$ is an arbitrary vertical displacement, added for clarity.

The QPM can be formulated in the infinite momentum frame of the proton. In this frame the time scale with which partons within the proton interact with each other is time dilated and the proton charge distribution is Lorentz contracted. The γ^*-parton interaction is then instantaneous and incoherent so that the partons can be treated as free. The subsequent interactions which confine the struck parton within a bound hadron occur on much longer time scales and do not affect the result.

The DIS cross section can now be written as a sum of the cross sections for elastic electron-parton scattering in which the parton of type i carries a fraction ζ of the

proton's momentum:

$$\frac{\mathrm{d}^2\sigma_{ep\to eX}}{\mathrm{d}x\mathrm{d}Q^2} = \sum_i \int_0^1 d\zeta f_i(\zeta) \frac{\mathrm{d}^2\sigma_{eq_i\to eq_i}}{\mathrm{d}x\mathrm{d}Q^2} \tag{3.12}$$

where $f_i(\zeta)$ is the probability that the parton q_i carries a fraction ζ of the proton's momentum. Putting the out-going parton on shell gives

$$(q + \zeta p)^2 = 0 \tag{3.13}$$

and hence that ζ is simply the Bjorken scaling variable x. The elastic cross section is calculable within QED for spin $\frac{1}{2}$ partons and from this it follows that

$$F_2(x, Q^2) = x \sum_i e_i^2 f_i(x) \tag{3.14}$$

$$2xF_1(x) = F_2(x) \tag{3.15}$$

where e_i is the charge of the quark of flavour i and the sum is over all active quark flavours. The Q^2 independence of F_2, shown in equation 3.14, is known as Bjorken scaling and results from the assumption of point-like non-interacting partons within the proton. Equation 3.15, known as the Callan-Gross relation [36], follows from the assumption of spin $\frac{1}{2}$ partons. This is equivalent to $F_L = 0$ and its verification by a series of experiments was evidence for the spin $\frac{1}{2}$ nature of partons (quarks). The function $f_i(x, Q^2)$ is known as a Parton Density Function (PDF) and is independent of the hard scatter. This universal property allows the PDFs to be constrained from data from many different experiments and combined to produce global fits. A test of this universality is that the PDFs measured in DIS are applicable in hadron-hadron collisions where, for example, they correctly predict the rate of Drell-Yan pair production [37].

3.2.2 Scaling Violations

From figure 3.2(a) it can be seen that Bjorken scaling is only approximate; there are systematic scaling violations, particularly at low x, where a clear Q^2 dependence is

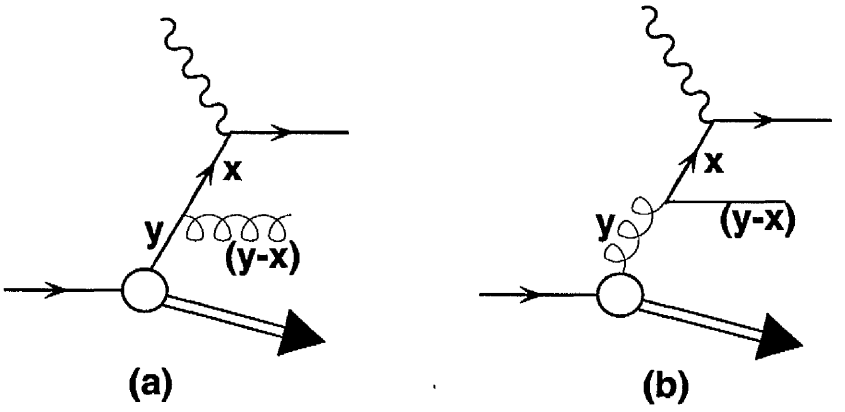

Figure 3.3: Diagrams of the splitting functions (a) $P_{qq}\left(\frac{x}{y}\right)$ and (b) $P_{gq}\left(\frac{x}{y}\right)$. The quark that couples to the photon carries a fraction x of the proton's momentum, but originated from a quark or gluon carrying a momentum fraction y.

visible. This reflects the fact that, even at large Q^2, the partons should not be considered to be entirely non-interacting. These scaling violations can be understood by including QCD corrections to the Quark Parton Model. For example, contributions that are leading order in α_s are the emission of a gluon from the struck quark and quark-anti-quark pair production from a gluon. These processes are illustrated in figure 3.3 and result in logarithmic corrections of the form $\alpha_s \ln Q^2$ and $\alpha_s \ln \frac{1}{x}$. The iteration of these splitting processes leads to a description of the low x regime in terms of ladder diagrams such as that shown in figure 3.4(a). These QCD processes also result in a small, but non-zero, perturbative QCD prediction for F_L [38][4].

For a given order, n, of perturbation theory the QCD expansion for the evolution of $F_2(x, Q^2)$ contains terms of order $\alpha_s^n \ln^m Q^2$ and $\alpha_s^n \ln^m \frac{1}{x}$, with $m \leq n$. A full QCD expansion is not tractable, but in different kinematic regions of the $x - Q^2$ plane different terms dominate the expansion. Two different evolution schemes are discussed in the next section, these can be tested over a wide kinematic region by data from HERA.

[4]For a recent measurement of F_L see, for example, reference [30].

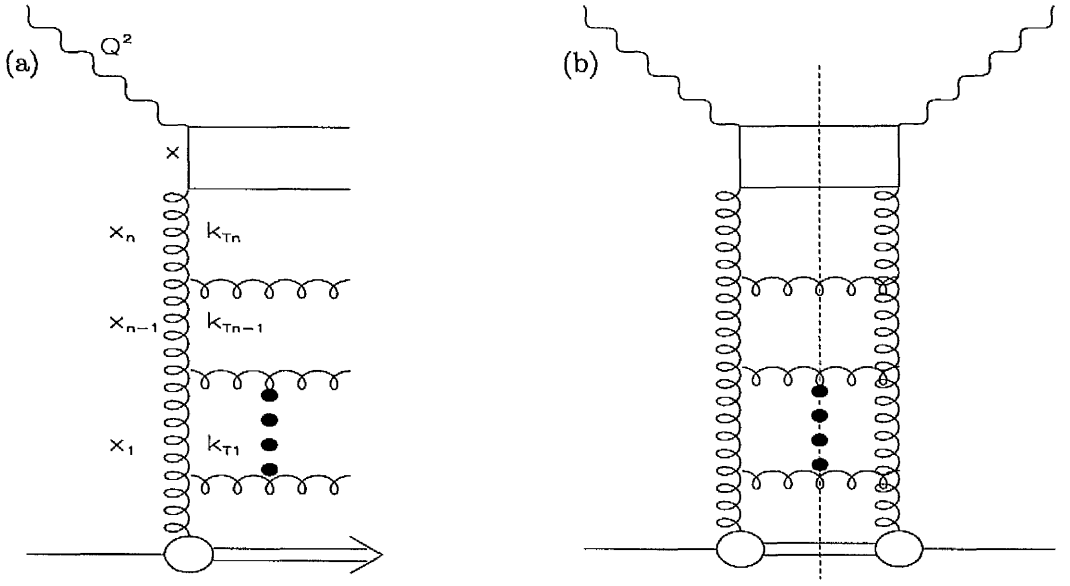

Figure 3.4: (a) A ladder diagram which contributes to $F_2(x, Q^2)$ at low x. In DGLAP evolution the diagram is, in general, composed of both quarks and gluons and the partons are ordered in transverse momentum. In BFKL evolution only gluons contribute and they are ordered in x. The BFKL equation is formed by summing squared amplitudes such as that in (b).

3.3 Low x Phenomenology

A striking feature of recent DIS data is the substantial rise in F_2 with decreasing x at low x and high Q^2, as shown in figure 3.5. The rise of F_2 is related to the increasing gluon density at low x. Within the framework of the DGLAP equations the growth of the parton distributions may be interpreted as due to their Q^2 evolution. In the framework of the BFKL equation this growth is a consequence of their x evolution. These formalisms are briefly discussed in this section.

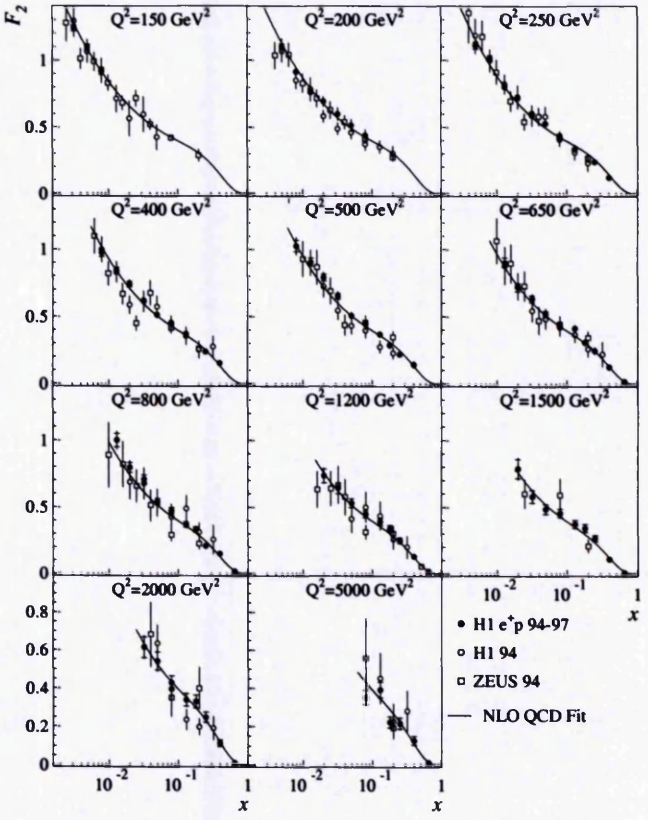

Figure 3.5: Measurement of the structure function $F_2(x, Q^2)$ [27] at high Q^2 as a function of x. Also shown are earlier data from H1 [39] and ZEUS [40] and a NLO QCD fit.

3.3.1 The DGLAP Evolution Mechanism

In the currently accessible kinematic region scaling violations are well described using the QCD formalism developed by Dokshitzer, Gribov, Lipatov, Altarelli and Parisi (DGLAP) [41]. The PDFs are split into functions representing the valence quark (non-singlet flavour), non-valence quark (singlet flavour) and gluon distributions. The DGLAP equations enable the Q^2 dependence of the parton distributions to be computed from given parton distributions at a scale Q_0 at which perturbative QCD is valid. The input distributions themselves are currently not calculable

within QCD[5] and are determined from data at a higher scale. The evolution proceeds through the splitting processes illustrated in figure 3.3.

The result is the DGLAP equations, a set of coupled integro-differential equations which describe the evolution of the parton density functions for the non-singlet quark, $q^{NS}(x,Q^2)$, singlet quark, $q^S(x,Q^2)$, and gluon density , $g(x,Q^2)$ by

$$\frac{dq^{NS}(x,Q^2)}{d\ln Q^2} = \frac{\alpha_s(Q^2)}{2\pi}\int_x^1 \frac{dy}{y}\left[q^{NS}(y,Q^2)P_{qq}\left(\frac{x}{y}\right)\right] \tag{3.16}$$

$$\frac{dq^{S}(x,Q^2)}{d\ln Q^2} = \frac{\alpha_s(Q^2)}{2\pi}\int_x^1 \frac{dy}{y}\left[q^{S}(y,Q^2)P_{qq}\left(\frac{x}{y}\right) + g(y,Q^2)P_{qg}\left(\frac{x}{y}\right)\right] \tag{3.17}$$

$$\frac{dg(x,Q^2)}{d\ln Q^2} = \frac{\alpha_s(Q^2)}{2\pi}\int_x^1 \frac{dy}{y}\left[q^{S}(y,Q^2)P_{gq}\left(\frac{x}{y}\right) + g(y,Q^2)P_{gg}\left(\frac{x}{y}\right)\right] \tag{3.18}$$

where, for example, $P_{qq}\left(\frac{x}{y}\right)$ is the 'splitting function' describing the probability of a struck quark of momentum fraction x originating from a quark with momentum y via the process of gluon bremsstrahlung, illustrated in figure 3.3(a). The splitting functions have been calculated in leading order and next-to-leading order [42] QCD.

The solution of these equations leads, via equation 3.14, to the logarithmic dependences of the structure function on Q^2, such that F_2 falls with Q^2 at high x and rises with Q^2 at low x. The formalism corresponds to summing only those terms of the form $\alpha_s^n \ln^n Q^2$, the leading log approximation (LLA). DGLAP evolution is applicable where perturbation theory is valid and $\ln(1/x) \ll \ln(Q^2/Q_0^2)$. Parameterisations of $F_2(x,Q^2)$ based solely on DGLAP evolution, such as those of Martin, Roberts and Stirling [43], have been successful in describing all the HERA data to date.

3.3.2 The BFKL Evolution Mechanism

At sufficiently low x, the $\log\frac{1}{x}$ terms, which are not described by the DGLAP equations, are expected to become significant. An alternative expansion in terms

[5]Lattice QCD may be able to calculate these non-perturbative functions.

of log $\frac{1}{x}$ can be made for fixed Q^2. The evolution equation resulting from the summation of the leading log $\frac{1}{x}$ terms was developed by Balitsky, Fadin, Kuraev and Lipatov (BFKL) [44][6]. At leading log only terms involving gluon splitting need to be considered, such that figure 3.4(a) is a typical contribution to F_2. Summing squared amplitudes, such as that in figure 3.4(b), for all possible gluon interactions, leads to the BFKL equation. The BFKL equation is valid where perturbative QCD can be used and $\ln(Q^2/Q_0^2) \ll \ln(1/x)$. An analytical solution at fixed Q^2 leads to the prediction that in the low x region

$$F_2(x, Q^2) \sim x^{-\lambda} \tag{3.19}$$

and at HERA energy scales $\lambda \sim 0.5$.

For $x < 0.1$ the measurement of $F_2(x, Q^2)$ can be parameterised as in equation 3.19 [46], with the value of λ needed to fit the data increasing from 0.2 to 0.4 in the Q^2 range from 1.5 to 10^3 GeV^2. At high Q^2 the high value of λ may be consistent with a BFKL interpretation of the x evolution of $F_2(x, Q^2)$. However, this behaviour is also compatible with DGLAP evolution, as can be seen from the good description of the data in figure 3.5. Further searches for evidence of BFKL evolution may be preformed in exclusive channels such as forward jet production [47].

3.3.3 F_2 and Regge Theory

The structure function F_2 is related to the total cross section of the virtual photon-proton interaction by

$$\sigma_{tot}(\gamma^* p) \approx \frac{4\pi^2\alpha}{Q^2} F_2(W, Q^2) \tag{3.20}$$

where, at low x, $W \approx \sqrt{Q^2/x}$. If x is sufficiently low then the Regge limit $W^2 \gg Q^2$ is satisfied. A simple Regge model (see section 4.1) predicts that the virtual photon-proton cross section has the same energy dependence as the real photon-proton

[6] A calculation of the next-to-LLA summation has also been completed [45].

cross section and hence that $\lambda \sim 0.08$. Measurements of F_2 at very low Q^2 are consistent with this behaviour [48]. Large deviations from this behaviour are seen as Q^2 increases, indicating the need for corrections to the simple Regge picture.

3.4 Photon Physics

In DIS the photon virtuality resolves scales much smaller than the size of the proton ($Q^2 \gg 1\,\mathrm{GeV}^2$) and hence is able to probe the structure of the proton. Conversely, in photoproduction the photon is almost real ($Q^2 \sim 0$) and different physics processes are seen. The total ep cross section contains a $1/Q^4$ factor, as in equation 3.8, and so is dominated by photoproduction. In this case HERA is effectively a γp collider with a centre of mass energy $W = \sqrt{ys}$. The γp cross section, $\sigma_{\gamma p}$, can be calculated from the measured cross section, σ_{ep}, by

$$\frac{\mathrm{d}^2\sigma_{ep}(s)}{\mathrm{d}Q^2\mathrm{d}y} = \sigma_{\gamma p}(ys)F(y,Q^2). \tag{3.21}$$

The photon flux, $F(y,Q^2)$, can be calculated using the Weizsäcker-Williams approximation [49].

At leading order, two classes of high P_T photoproduction events can be defined. In the direct process, shown in figure 3.6(a), the photon behaves as a point-like object, coupling directly to the hard subprocess. In the resolved process, shown in figure 3.6(b), the photon behaves hadronically, with a single parton from the photon entering the hard scatter. A useful variable to distinguish between these classes is x_γ, the fraction of the photon's momentum transferred to the hard subprocess. This will be one for direct events and less than one for resolved events. This picture is only valid for leading order processes and care must be taken to use variables which, although having a physical interpretation at leading order, are well defined at all orders.

In a resolved process the photon splits into a $q\bar{q}$ pair well before the interaction.

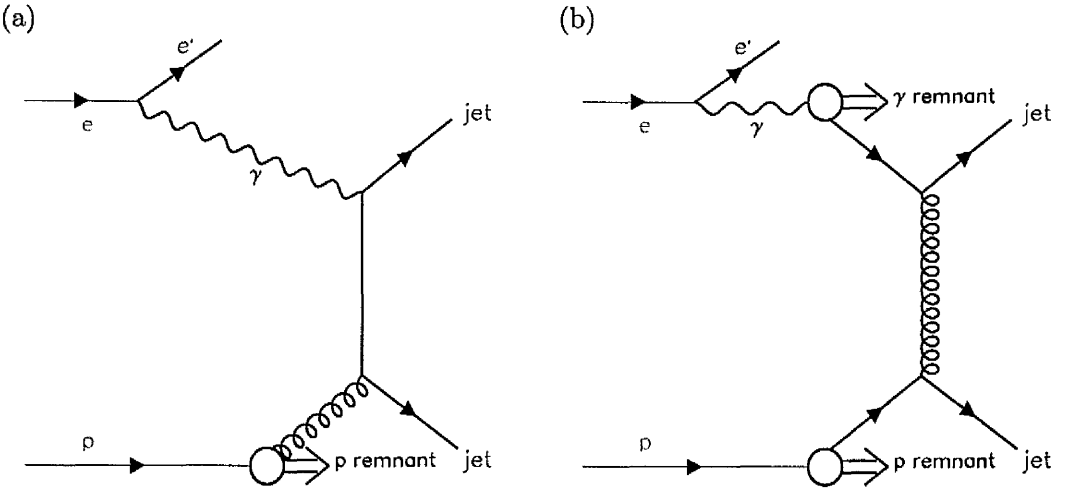

Figure 3.6: Examples of (a) direct and (b) resolved processes in photon-proton interactions.

After this QED process, QCD evolution can occur so that the photon contains both gluons and quarks. A photon structure function F_2^γ can be defined in a similar way to the proton structure function. This can be measured directly in $\gamma^*\gamma$ events at e^+e^- colliders[7]. These measurements are mainly sensitive to the combination of quark densities. At HERA the partonic content of the photon can be probed using the P_T of final state jets. These results are sensitive to the gluon density of the photon, as shown in figure 3.7 [51].

The resolved component is dominant except at high P_T scales, where the final state requires a large γp centre-of-mass energy. Resolved events are characteristically different from direct events; they have a photon remnant in the final state and are dominated by gluon-exchange processes whereas in direct events there is no photon remnant and the propagator is a quark.

[7]For a comprehensive review of photon structure measurements both at e^+e^- and ep colliders see [50].

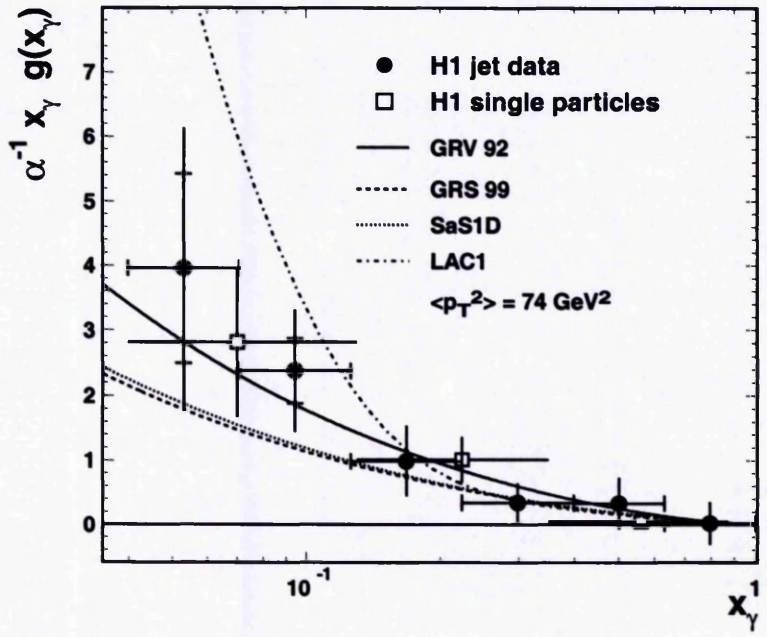

Figure 3.7: H1 extraction of the gluon density $g(x_\gamma)$ multiplied by $\alpha^{-1}x_\gamma$ as a function of x_γ for a mean $\hat{P_T}^2 = 74\,\mathrm{GeV}^2$ of the hard partons. Also shown is a previous H1 measurement at $\hat{P_T}^2 = 38\,\mathrm{GeV}^2$ using single high E_T particles [52]. The LO parameterisations of the gluon distribution [53] based on fits to e^+e^- two-photon data are also shown.

3.5 Jet Physics

In the majority of γp interactions the final state particles have a small amount of transverse momentum, P_T. In jet events, however, the outgoing partons have a large amount of P_T and the hadronisation results in a collimated jet of particles whose properties are correlated with the dynamics of the outgoing parton. Hence, jet events are extremely useful in understanding the underlying dynamics of partonic interactions.

There is no unique definition of a jet. Instead, a number of different algorithms are

available. Jets must be easy to measure experimentally and theoretically reliable to calculate [54]. In pQCD there is a divergence when two massless particles are collinear; this is cancelled in the total cross section by a virtual contribution from the equivalent process with the two partons replaced by one parton which carries the sum of the momenta of the pair. For this cancellation to occur in the jet calculation, a collinear pair of particles must be treated in the same way as one particle with their combined momentum. An equivalent experimental requirement is that the algorithm must not depend strongly on the angular resolution of the detector because when two collinear particles enter the same calorimeter cell they are unresolved.

To avoid the divergence from the emission of particles with vanishingly small energy, the calculation must be insensitive to the addition of a soft particle (infra-red safe). Experimentally, the results should not depend strongly on calorimeter noise, which adds low energy particles to the true event. The k_t algorithm [55] fulfills these requirements and is used in the analysis presented in this thesis. It is described in more detail in Appendix A.

The cross section for jet events can be written as a convolution of the proton and photon parton densities and the matrix elements for the parton scattering, $\hat{\sigma_{ij}}$,:

$$\sigma = \sum_{ij} \int \mathrm{d}x_A x_B f_{i/A}(x_A, \mu^2) f_{j/B}(x_B, \mu^2) \hat{\sigma_{ij}} \tag{3.22}$$

where $f_{i/A}$ is the proton distribution for partons of flavour i carrying a momentum fraction x_A, $f_{j/B}$ is the photon distribution for partons of flavour j, carrying a momentum fraction x_B and μ is the factorisation scale. The hard scale of the jet P_T allows a perturbative calculation of the parton-parton scattering. The leading order (LO) calculations have been implemented in Monte Carlo models and the next-to-LO (NLO) corrections have also been calculated. The proton PDFs are well constrained and provide a good description of jet data. The photon PDFs are less well constrained at high x_γ but a good description of the data is still obtained. Monte Carlo generators evolve the outgoing partons into final state hadrons through

parton showering and hadronisation. Parton showering simulates higher order perturbative effects, by iterating the QCD radiation of quarks and gluons until some scale, typically 1 GeV. The final, non-perturbative phase is modelled by a phenomenological hadronisation model, converting the partons into hadrons. The two main hadronisation schemes used are the string fragmentation model [56] (implemented in JETSET [57] which is used by PYTHIA) and the cluster fragmentation model [58] (implemented in HERWIG).

In the Lund string fragmentation model the colour field between a $q\bar{q}$-pair is treated as a string. As the $q\bar{q}$ separation increases the energy stored in the string rises until the string breaks forming a new $q\bar{q}$ pair and strings. Gluons cause kinks in the string. The process continues until all the available energy is used up, leaving only colourless, on-shell hadrons.

In the cluster fragmentation model all outgoing gluons are split into $q\bar{q}$-pairs. Colour singlet pairs end up close together in phase space and neighbouring $q\bar{q}$-pairs can be combined to form colour singlet clusters. Heavy clusters are split into two lighter clusters. All clusters then decay into colourless resonances or stable hadrons.

3.6 Multiple Parton-Parton Interactions

QCD calculations were not found to give a good description of the initial HERA jet data [59], even after allowing for radiation effects and fragmentation. The transverse energy flow outside of the jets was much greater than that expected from single parton-parton scattering. This additional underlying event energy can be attributed to further interactions which occur between the beam remnants. This may anyway be expected from the proliferation of low x partons seen in the growth of F_2 [60].

In γp collisions it can be seen (figure 3.8) that the amount of energy flow outside the jets is correlated with decreasing x_γ^{jets} [61]. Direct events, which are at high

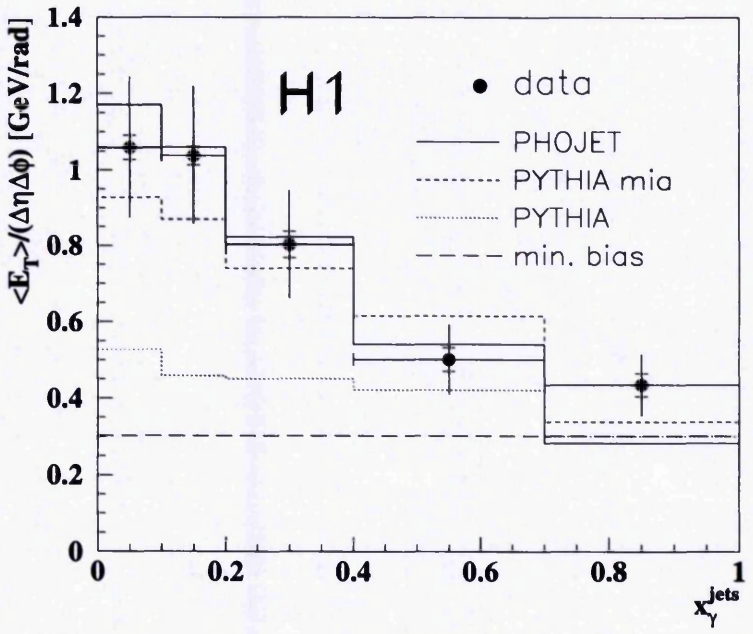

Figure 3.8: The transverse energy flow outside jets, as a function of x_γ^{jets}, compared to the calculations of QCD generators with (PYTHIA mia, PHOJET) and without (PYTHIA) beam remnant interactions.

x_γ^{jets}, have no photon beam remnant to interact further, whereas resolved events do, suggesting that the energy flow is indeed connected with interactions of the beam remnants. The effect of multiple interactions has also previously been observed in $p\bar{p}$ collisions [62].

Including this energy flow into the jet energy drastically alters the measured jet rate [63], particularly at low P_T and also the distributions of event variables. So, it is important that the effect of multiple interactions is well modelled in Monte Carlo simulations. This has been done in both PYTHIA [64] and HERWIG, which uses the JIMMY [60] package. The multiple interactions are modelled as further uncorrelated perturbative parton-parton scatters. The divergent matrix elements for these scatters are regulated by a P_T cut off, P_T^{mi}; this is the main free parameter in the model.

Chapter 4

Diffraction

This chapter aims to give a brief review of the field of diffraction, in order to set in context the analysis presented in this thesis.

Hadron-hadron cross sections at high energy are dominated by long-range, soft interactions. The low momentum transfer means that perturbative QCD is not applicable. The best description of these interactions is given by the phenomenological model of Regge theory [65]. A brief outline of Regge theory[1] and its description of total hadronic cross sections is given in section 4.1. Regge theory explains the observed rise of the total cross section at high centre-of-mass energies by a diffractive exchange called the pomeron. At HERA, the hard scale Q^2 can be used to probe the structure of the pomeron and these measurements are outlined in section 4.2. Finally, it is possible to investigate diffractive processes in which the momentum transferred is large and therefore provides a hard scale enabling, in principle, pQCD calculations to be made. An example of such a process is discussed in section 4.3 and is the subject of the analysis in this thesis.

[1]For a more detailed discussion see [66].

4.1 Regge Theory

Regge theory was developed before QCD and is based solely on very general assumptions about the scattering process. Regge theory aims to determine the behaviour of the scattering amplitude in the limit that the centre-of-mass energy is much greater than all other scales in the process. Its predictions act as a constraint on the high energy properties of QCD [68].

4.1.1 s and t Channel Processes

A general two body scattering process $ab \to cd$ can be described in terms of the particle masses and the Lorentz invariant scalar products of the momenta. The Mandelstam variables, s, t and u, are defined by

$$s = (p_a + p_b)^2 = (p_c + p_d)^2 \tag{4.1}$$

$$t = (p_a - p_c)^2 = (p_b - p_d)^2 \tag{4.2}$$

$$u = (p_a - p_d)^2 = (p_b - p_d)^2 \tag{4.3}$$

However, from conservation of momentum, u is not an independent variable and so, neglecting the external particle masses, the scattering amplitude can be written as $A(s,t)$. The centre-of-mass energy is $\sqrt{s}$ and t gives the square of the four-momentum transferred.

A further assumption about the scattering amplitude can be made: that it is an analytic function of the Lorentz invariants (regarded as complex variables). It can be shown that this is a consequence of causality. An important consequence of this analyticity is crossing symmetry.

The physical kinematic region for the s-channel process $ab \to cd$ is $s > 0, t < 0$. The amplitude $A_{ab\to cd}(s,t)$ can be analytically continued into the unphysical region $t > 0, s < 0$. This gives the amplitude for the t-channel process $a\bar{c} \to \bar{b}d$. So, this

crossing symmetry means that these two physically different processes will have the same scattering amplitude:

$$A_{ab\to cd}(s,t) = A_{a\bar{c}\to\bar{b}d}(t,s). \tag{4.4}$$

4.1.2 Regge Trajectories

The scattering amplitude for the t-channel process $a\bar{c} \to \bar{b}d$ can be expanded as a series of partial waves of different angular momenta:

$$A_{a\bar{c}\to\bar{b}d}(s,t) = \sum_{l=0}^{\infty}(2l+1)a_l(s)P_l(cos\theta) \tag{4.5}$$

where $P_l(cos\theta)$ is the Legendre Polynomial for angular momentum l, θ is the centre-of-mass frame scattering angle between a and c, related to s and t by $\cos\theta = 1 + \frac{2t}{s}$ and the functions $a_l(s)$ are the partial wave amplitudes. Using crossing symmetry this amplitude may be continued into the s-channel to give the amplitude for the process $ab \to cd$. The full partial-wave series can next be summed using a method suggested by Sommerfeld [69] (following Watson [70]). The pole in the l^{th} partial wave then takes the form

$$a_l(t) \simeq \frac{\beta(t)}{l-\alpha(t)} \tag{4.6}$$

so that there is a 'Regge pole' in the partial-wave amplitude at $l = \alpha(t)$ and $\beta(t)$ is the residue function specifying the coupling of the pole to the external particles. Taking the Regge limit, $s \to \infty$, the asymptotic behaviour of the Legendre polynomial can be used to isolate the high energy behaviour of the scattering amplitude:

$$A(s,t) \to \beta(t)s^{\alpha(t)}. \tag{4.7}$$

This is the characteristic Regge-pole asymptotic power behaviour of the scattering amplitude from the exchange of a Regge trajectory. This can be viewed as the exchange of an object, a reggeon, with angular momentum $\alpha(t)$, as shown in figure 4.1. This is not a real particle; the angular momentum is a continuous complex variable.

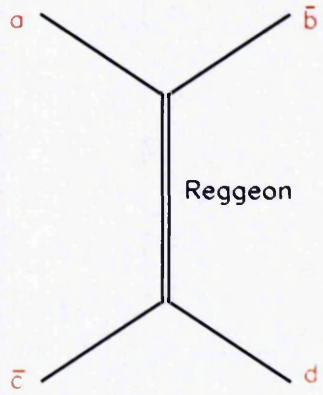

Figure 4.1: Scattering in the t channel, viewed as reggeon exchange.

The amplitude effectively sums the contributions from all possible exchange particles with appropriate quantum numbers. For the t-channel scattering process with t positive the amplitude will have poles corresponding to the formation of physical particles of spin J_i and mass m_i, where $\alpha(m_i^2) = J_i$. Consider the reaction $\pi^- p \to \pi^0 n$. For positive t, i.e. $\pi^-\pi^0 \to \bar{p}n$, the amplitude has poles corresponding to the production of physical particles with the quantum numbers of the ρ. Chew and Frautschi [71] plotted the spin of mesons against their mass squared and found that they lay in a straight line,

$$\alpha(t) = \alpha(0) + \alpha'(t) \tag{4.8}$$

for, at least, positive t. This is shown in figure 4.2 for the ρ, ω, f and a set of mesons, where $\alpha(0) = 0.55$ and $\alpha' = 0.86$ GeV^{-2}. Hence, from equation 4.7,

$$A(s,t) \sim s^{\alpha(0)+\alpha'(t)} \tag{4.9}$$

and the differential cross section is predicted to be

$$\frac{\mathrm{d}\sigma}{\mathrm{d}t} \sim \frac{1}{s^2}|A(s,t)|^2 \sim s^{2\alpha(0)+2\alpha'(t)-2}. \tag{4.10}$$

This has been well verified in many processes [67]. $\alpha(t)$ obtained from measurements of $\frac{\mathrm{d}\sigma}{\mathrm{d}t}$ for $\pi^- p \to \pi^0 n$ in the pion beam energy range 20.8-199.3 GeV [72], shown in

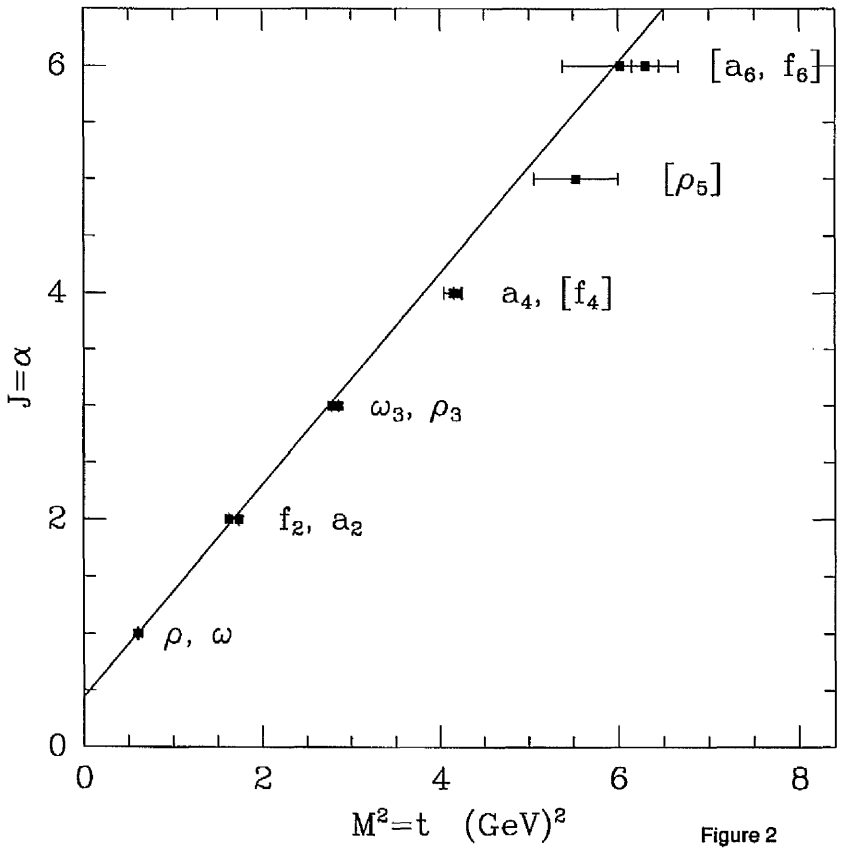

Figure 4.2: The Chew-Frautschi plot of the ρ trajectory.

figure 4.3, agrees extremely well with the extrapolation of the linear ρ trajectory to negative t.

4.1.3 The Total Cross Section

The unitarity of the scattering matrix, a requirement from conservation of probability, gives the optical theorem, which relates the imaginary part of the forward elastic amplitude, A_{el}, to the total scattering cross section:

$$\sigma_{tot} = \frac{1}{s}\Im m\ A_{el}(s,0). \tag{4.11}$$

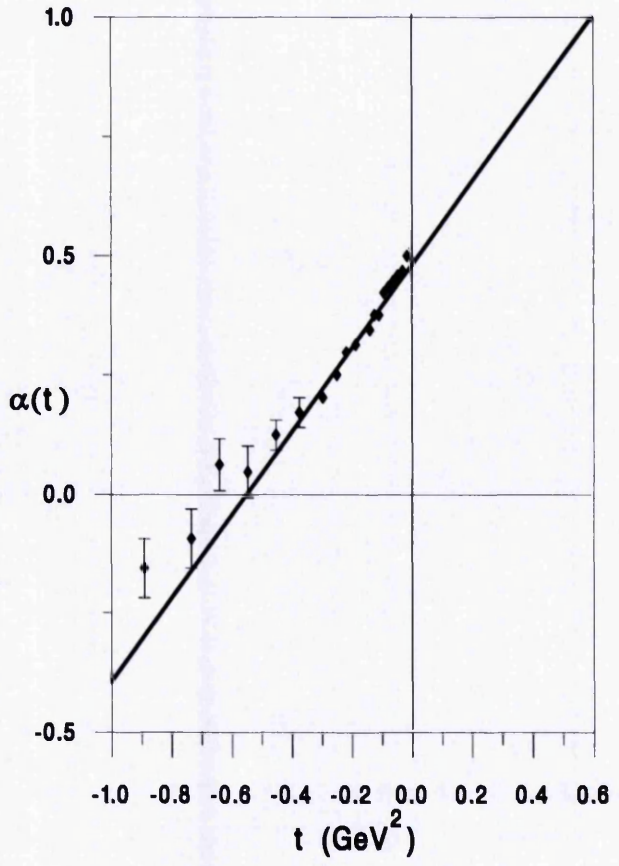

Figure 4.3: The points show $\alpha(t)$ obtained from $\pi^- p \to \pi^0 n$ scattering data [72]. The straight line shows the linear extrapolation of the Regge trajectory shown in figure 4.2 to negative t.

From the scattering amplitude at $t = 0$, equation 4.9, it follows that

$$\sigma_{tot} \sim s^{\alpha(0)-1} \tag{4.12}$$

where $\alpha(0)$ is the intercept of the appropriate trajectory. For example, the ρ-trajectory has $\alpha(0) = 0.55$ and so the cross section for processes in which these quantum numbers are exchanged falls as s increases. Indeed, Pomeranchuk and

Okun [73] proved that in any scattering process in which charge is exchanged the cross section vanishes as $s \to \infty$ (the Pomeranchuk theorem).

Foldy and Peierls [74] noticed the converse: if a cross section does not fall as s increases then it must be dominated by the exchange of vacuum quantum numbers. Experimentally, the total cross sections for hadron-hadron collisions have been observed to rise slowly with s [75]. This requires a Regge trajectory with an intercept $\alpha(0) \geq 1$ and which carries vacuum quantum numbers. This is called the pomeron [76]. No physical particles which would lie on the trajectory have yet been conclusively identified, although particles such as glueballs (bound states of gluons) could exist within QCD.

Figure 4.4 shows the total pp and $p\bar{p}$ cross sections with fits by Donnachie and Landshoff [77]. The fits are of the form

$$\sigma_{tot}(s) = Xs^{\alpha_{\mathbb{P}}-1} + Ys^{\alpha_{\mathbb{R}}-1}. \tag{4.13}$$

The first term in the fits is the Pomeron contribution, with intercept 1.08, and is common to both the pp and $p\bar{p}$ cross section because the pomeron is unable to distinguish between particles and anti-particles. The second term does distinguish the two and is from the exchange of the ρ trajectory with intercept 0.55. Donnachie and Landshoff were also able to fit the $\pi^- p$, $\pi^+ p$ and γp [78] total cross sections with the same trajectory intercepts, which suggests that the pomeron can be considered as a universal object.

At HERA, diffractive processes can be studied where a hard scale is present. The energy dependence of the photon-proton cross section has been observed to steepen with increasing virtuality of the photon, as described in section 3.3.2. A pomeron trajectory cannot vary with Q^2, so this suggests some more complex behaviour. This change in 'effective pomeron intercept' has also been observed in γp processes.

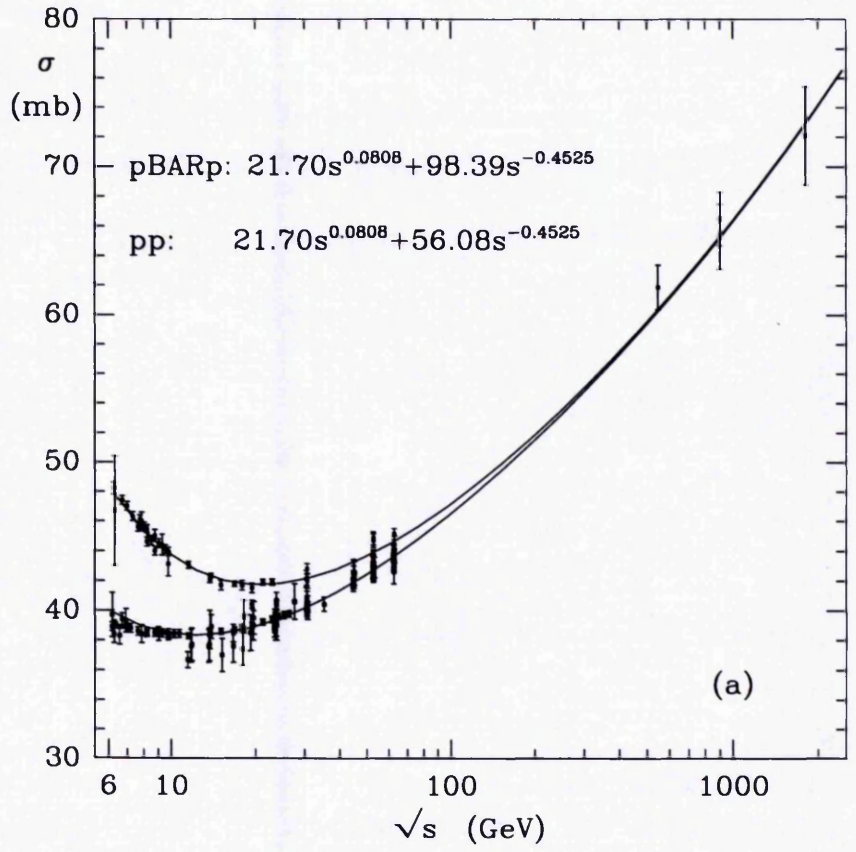

Figure 4.4: The centre-of-mass energy dependence of the proton-proton and proton-anti-proton total cross sections together with a fit by Donnachie and Landshoff.

4.1.4 Diffractive Processes in γp Interactions

The photon may interact with the proton via pomeron exchange, if it first fluctuates into a $q\bar{q}$ pair which may then evolve further. The reaction $\gamma p \rightarrow Vp$, figure 4.5(a), where V is any vector meson, may be considered as elastic and has a cross section of around 10% of the total photoproduction cross section [78]. In Regge theory the s dependence of this quasi-elastic cross section should be the same as that for the total γp cross section. Figure 4.6 shows the energy dependence of the vector meson production cross sections. The energy dependence of the ρ production cross

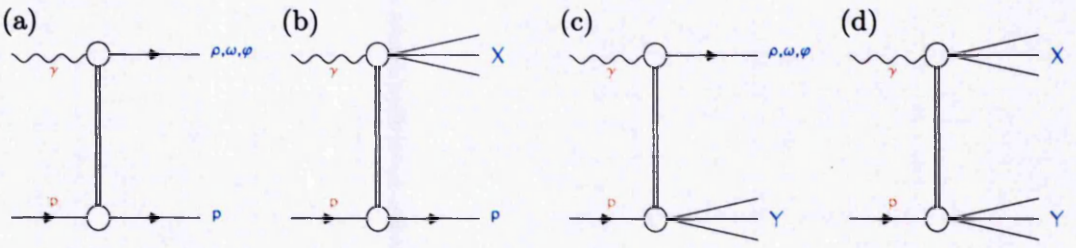

Figure 4.5: Diffractive Interactions in γp collisions. (a) Quasi-elastic vector meson production. (b) Single photon dissociation. (c) Single proton dissociation. (d) Double dissociation.

section is indeed similar to that of the total γp cross section. However, the J/ψ cross section, where the vector meson mass introduces a hard scale into the process, is significantly steeper.

Diffraction also exists as an inelastic process, in which one or both of the interacting hadrons break up or dissociate, shown in figures 4.5(b)-(d). In each case no colour is exchanged and the dissociated state has identical quantum numbers to the incoming particle. The total diffractive contribution to the total γp cross section, at 300 GeV, was found to be around 40% [78]. Diffractive dissociation is a result of non-zero momentum transfer. At the momentum transfer studied in this thesis both the proton and photon dissociate.

4.2 Diffractive DIS

At HERA, a class of DIS events with a large rapidity gap extending from the proton direction has been observed [81]. These events can be attributed to the exchange of an object with vacuum quantum numbers– the pomeron. A diffractive DIS event is shown schematically in figure 4.7.

The hadronic final state can be split into two systems of invariant mass M_X and M_Y, which can be defined as being separated by the largest rapidity gap in the final

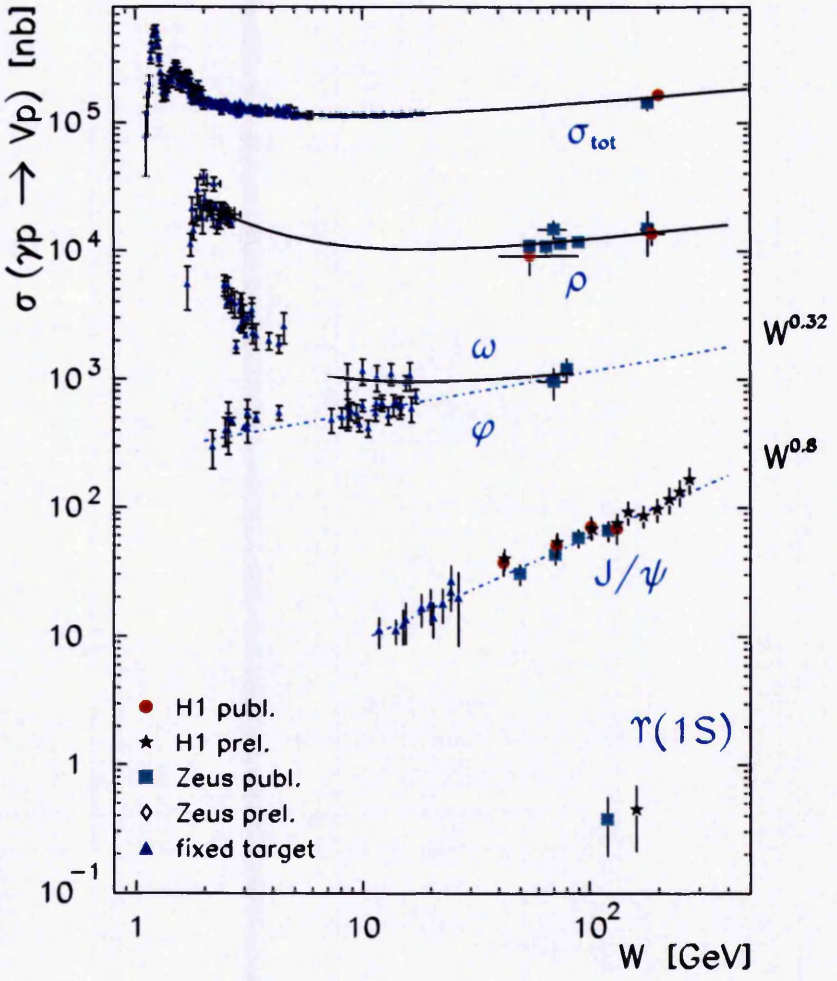

Figure 4.6: The centre-of-mass energy dependence of the total γp cross section and the total cross section for vector meson production measured at HERA and fixed target experiments. Plot from [79] with data from [80].

state. Typically, M_Y is close to the proton mass. In addition to the existing DIS variables additional Lorentz invariants are used:

$$t = (p - Y)^2 \tag{4.14}$$

$$\beta = \frac{-q^2}{2q \cdot (P - p_Y)} = \frac{Q^2}{Q^2 + M_X^2 - t} \tag{4.15}$$

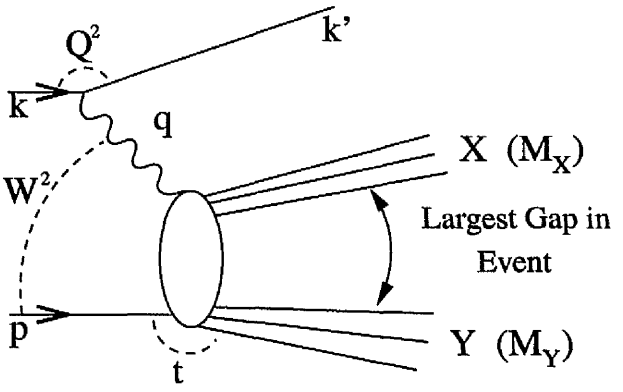

Figure 4.7: Schematic of a diffractive DIS event.

$$x_{\mathbb{P}} = \frac{q \cdot (P - p_Y)}{q \cdot P} = \frac{Q^2 + M_X^2 - t}{Q^2 + W^2 - M_p^2} = \frac{x}{\beta}. \tag{4.16}$$

In the infinite momentum frame of the proton, in the language of pomeron exchange, $x_{\mathbb{P}}$ is the fraction of the proton's momentum carried by the pomeron and β is the fraction of the pomeron's momentum carried by the struck parton. Both M_X and M_Y are required to be small, corresponding to the Regge limit and giving the large rapidity gap seen.

In the leading $\log(Q^2)$ approximation, the cross section for this process, $\gamma^* p \to p'X$, can be written in terms of convolutions of universal partonic cross sections, $\sigma^{\gamma^* i}$, with diffractive parton distributions, f_i^D, for partons of flavour i:

$$\frac{\mathrm{d}^2\sigma_{ep\to ep'X}}{\mathrm{d}x_{\mathbb{P}}\mathrm{d}t} = \sum_i \int_x^{x_{\mathbb{P}}} d\xi \sigma^{\gamma^* i}(x, Q^2, \xi) f_i^D(\xi, Q^2, x_{\mathbb{P}}, t). \tag{4.17}$$

This QCD factorisation has been rigorously proven [82] and is valid for large enough Q^2 and fixed x, $x_{\mathbb{P}}$ and t. The diffractive parton distributions should obey the DGLAP evolution equations.

Applying Regge theory to the concept of diffractive parton distributions leads to the Ingelman-Schlein model [83] of a 'resolved pomeron' with a partonic structure independent of $x_{\mathbb{P}}$ and t. In this model the diffractive parton distribution factorises into a flux factor, $f_{\mathbb{P}/\mathrm{p}}$, and pomeron parton distributions, $f_i^{\mathbb{P}}$. The flux factor describes the probability of a pomeron being 'emitted' from a proton.

By analogy to the proton structure function in equation 3.8, the diffractive DIS cross section can be used to define the diffractive structure function, $F_2^{D(4)}$:

$$\frac{\mathrm{d}^4\sigma_{ep\to ep'X}}{\mathrm{d}x\mathrm{d}\beta\mathrm{d}Q^2\mathrm{d}t} = \frac{4\pi\alpha_{em}^2}{\beta^2 Q^4}\left(1-y+\frac{y^2}{2}\right)F_2^{D(4)}(\beta,Q^2,x_{\mathbb{P}},t) \tag{4.18}$$

from which, using the Regge factorisation mentioned above, the pomeron structure function, $F_2^{\mathbb{P}}(\beta,Q^2)$, can be measured:

$$F_2^{D(4)}(\beta,Q^2,x_{\mathbb{P}},t) = f_{\mathbb{P}/\mathrm{p}}(x_{\mathbb{P}},t)F_2^{\mathbb{P}}(\beta,Q^2). \tag{4.19}$$

A measurement of F_2^D integrated over $M_Y < 1.6$ GeV and $|t| < 1$ GeV^2, $F_2^{D(3)}$, made by H1 [84] is shown in figure 4.8. This is in the kinematic range $4.5 < Q^2 < 75$ GeV^2, $0.0002 < x_{\mathbb{P}} < 0.04$ and $0.04 < \beta < 0.9$.

At large $x_{\mathbb{P}}$, deviations from the behaviour shown in equation 4.19 are seen. These can be described by the addition of a sub-leading reggeon exchange, which carries the quantum numbers of the ρ, w, f, a mesons. This contribution is factorisable into a reggeon flux, $f_{\mathbb{R}/\mathrm{p}}(x_{\mathbb{P}})$, and a meson structure function, $F_2^{\mathbb{R}}(\beta,Q^2)$, so that

$$F_2^{D(3)}(x_{\mathbb{P}},\beta,Q^2) = f_{\mathbb{P}/\mathrm{p}}(x_{\mathbb{P}})F_2^{\mathbb{P}}(\beta,Q^2) + f_{\mathbb{R}/\mathrm{p}}(x_{\mathbb{P}})F_2^{\mathbb{R}}(\beta,Q^2). \tag{4.20}$$

In Regge theory, the pomeron flux can be written

$$f_{\mathbb{P}/\mathrm{p}}(x_{\mathbb{P}}) = \int_{t_{\mathrm{cut}}}^{t_{min}} \frac{e^{B_{\mathbb{P}}t}}{x_{\mathbb{P}}^{2\alpha_{\mathbb{P}}(t)-1}}\mathrm{d}t \tag{4.21}$$

where the effective Regge trajectory is $\alpha_{\mathbb{P}}(t) = \alpha_{\mathbb{P}}(0) + \alpha'_{\mathbb{P}}(t)$. A similar expression can be written for the reggeon flux. A fit of this form was made to the data, where the parameters $\alpha'_{\mathbb{P}}(t)$, $\alpha'_{\mathbb{R}}(t)$, $B_{\mathbb{P}}$ and $B_{\mathbb{R}}$ were fixed using results from pp experiments. The fit gave a value of the reggeon intercept consistent with the previously measured ρ reggeon trajectory and a value of the pomeron intercept of

$$\alpha_{\mathbb{P}}(0) = 1.203 \pm 0.020\ (\mathrm{stat.}) \pm 0.013\ (\mathrm{syst.})^{+0.030}_{-0.035}\ (\mathrm{model}). \tag{4.22}$$

This is significantly larger than the soft pomeron intercept measured in inclusive hadron-hadron collisions, 1.08, and the value $\alpha_{\mathbb{P}}(0) = 1.068 \pm 0.016$ (stat.) $\pm$

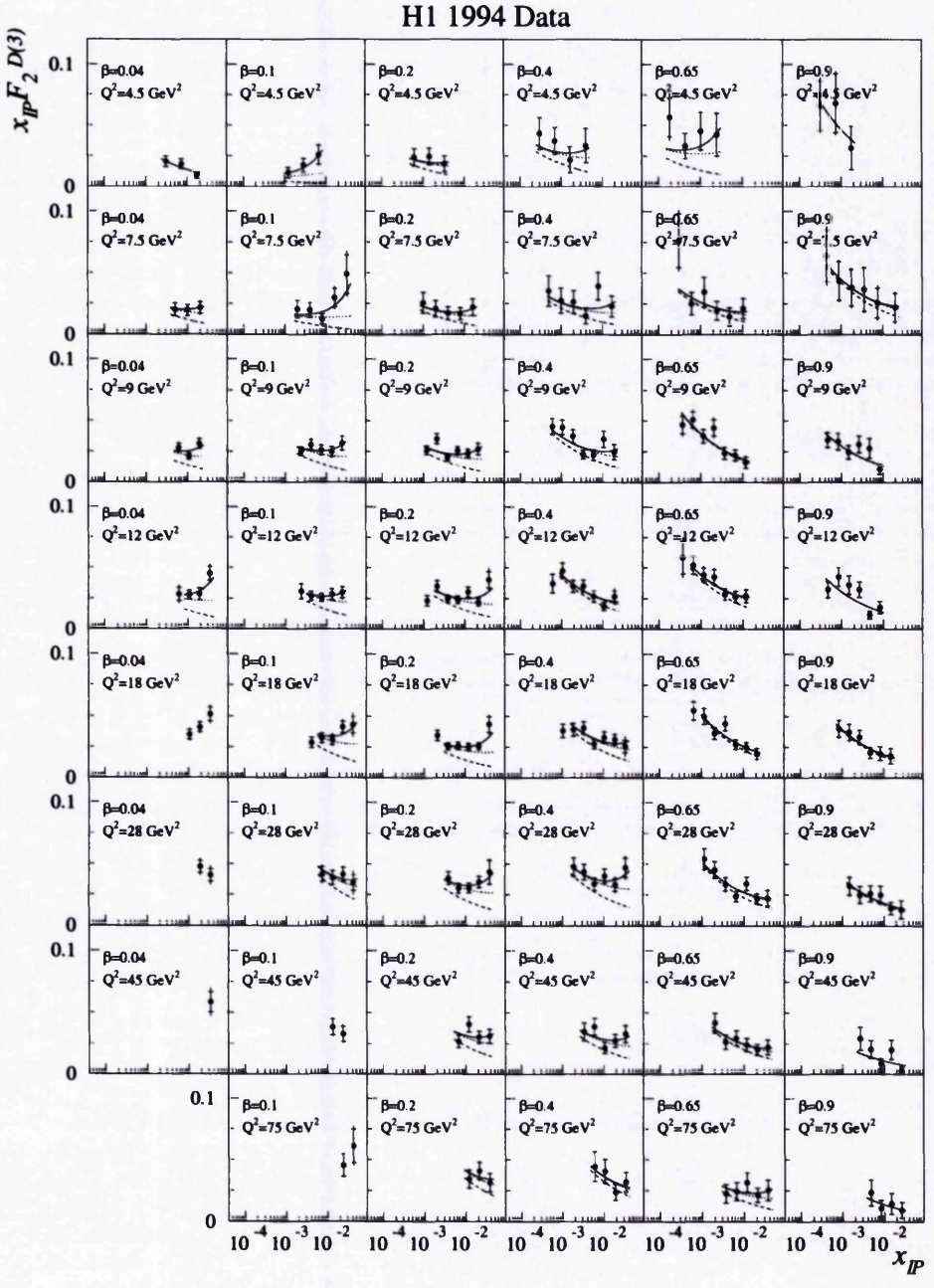

Figure 4.8: The diffractive structure function, plotted as $x_{\mathbb{P}} F_2^{D(3)}(x_{\mathbb{P}}, \beta, Q^2)$ against $x_{\mathbb{P}}$ for various β and Q^2 values. The solid curve shows the result of the fit described in the text and the dashed curve shows the pomeron contribution.

0.022 (syst.) $\pm$ 0.041 (model.) measured in photoproduction from the photon diffractive dissociation cross section [85].

The scaling violations seen in $F_2^{\mathbb{P}}(\beta, Q^2)$ can be described using the DGLAP equations to evolve a set of input parton distributions. A QCD fit was performed and an input distribution of gluons was preferred over that of solely quarks.

Measurements of energy flow [86] and thrust [87] in diffractive DIS also need a gluon dominated pomeron to describe the data. Diffractive dijet measurements are directly sensitive to both the shape and the normalisation of the gluon distribution within the pomeron, through the boson-gluon fusion process. The cross section for diffractive dijets can be predicted using the PDFs from the measurement of $F_2^{D(3)}$. A good agreement is found [88], showing consistency with QCD factorisation, and a flat gluon distribution is preferred. A fit to the dijet data gives $\alpha_{\mathbb{P}}(0) = 1.17 \pm 0.03$ (stat.) ± 0.06 (syst.)$^{+0.03}_{-0.07}$ (model), in agreement with the value obtained from $F_2^{D(3)}$.

Although the HERA data are well described by diffractive parton distributions, these do not work in describing data from $p\bar{p}$ collisions at the Tevatron. While the QCD factorisation described above should not hold in $p\bar{p}$ collisions, the scale of the breakdown is surprising.

CDF has measured the diffractive structure function of the anti-proton by measuring the ratio of the diffractive to inclusive cross sections [89]. In leading order QCD, this ratio is equal to the ratio of the corresponding structure functions and the inclusive structure function is well known. This measurement is shown in figure 4.9 and is compared to calculations using the diffractive parton densities from the H1 $F_2^{D(3)}$ measurement.

The results disagree both in normalisation and in shape, with the HERA prediction being significantly too high. There are a number of possible reasons for this disagreement. One reason may be the effect of multiple parton-parton interactions,

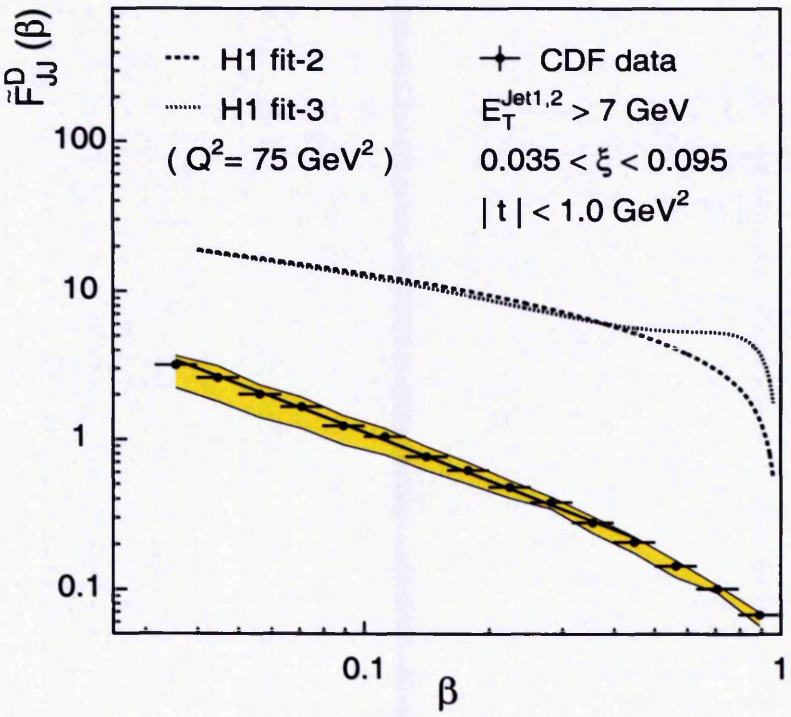

Figure 4.9: The diffractive structure function measured at CDF, shown as points, compared to predictions made from the structure function measured at H1, shown as dashed and dotted curves.

discussed in section 3.6. These may fill in the gap produced by a colour-singlet exchange [90]. The probability that a gap is not destroyed, the gap survival probability, may be much lower at the Tevatron than at HERA because there are more spectator partons in $p\bar{p}$ collisions than in γp collisions and the number density of partons increases with s. This could explain the discrepancy in the normalisations of the distributions. However, multiple interactions are not well understood. Further measurements, such as those dicussed in the next section, may improve our understanding.

4.3 Rapidity Gaps Between Jets

In events such as diffractive DIS, shown in figure 4.10(a), there is a hard scale at one end of the exchange and so perturbation theory becomes relevant. The small momentum transfer, t, means that there is no hard scale at the proton vertex. However, events with hard scales at both ends of the exchange are possible, when the momentum transfer is large. In this case the gap production mechanism is dominated by short distance physics [91] and the pomeron can be pictured as coupling in a point-like way. The process can then be treated as the convolution of the PDFs with elastic parton-parton scattering; this is illustrated in figure 4.10(b). At sufficiently high $|t|$ dijet events may be observed where the jets are widely separated in rapidity and there is very little hadronic activity between the jets- a rapidity gap [2]. These events may be observed experimentally as shown in figure 4.11 [92, 93]. The conditions $-t \gg \Lambda^2_{\rm QCD}$ and $s \gg -t$ mean that the events are in the perturbatively calculable Regge limit of QCD and so may give an insight into the underlying dynamics of diffraction.

These 'gaps between jets' events are in contrast with dijet production from typical QCD processes, which were discussed in section 3.5. In these dijet events a single quark or gluon is exchanged in the hard scatter, carrying colour. The subsequent hadronisation must ensure that the outgoing partons are in colourless hadrons. This leads to QCD radiation emitted between the jets which can be described as the result of a colour string connecting the two outgoing partons. It is also possible that rapidity gaps will be formed in these events by a fluctuation to zero of the number of hadrons produced between the two jets. Naively, this probability falls exponentially with the size of the rapidity region, assuming a simple Poisson distribution for the multiplicity fluctuations. To reduce this probability it is necessary to look at large jet-jet separations.

[2] Experimentally, pseudo-rapidity gaps are observed; these are referred to as rapidity gaps.

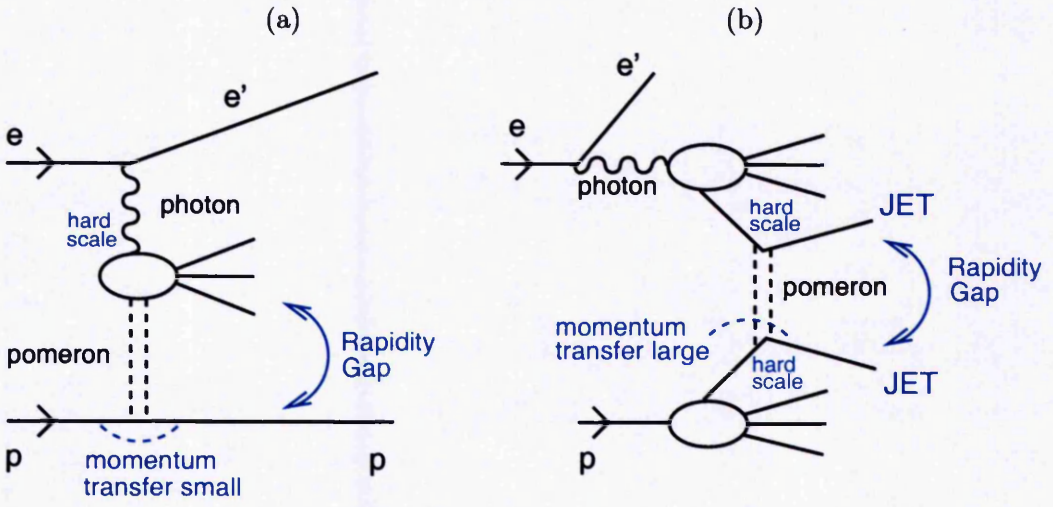

Figure 4.10: (a) Diffractive DIS, in this process the momentum transferred across the rapidity gap is small. (b) Dijet production with the exchange of a colour singlet object forming a rapidity gap between the jets. The momentum transferred across the rapidity gap is large.

An excess of events with rapidity gaps between jets over that expected from typical QCD processes has already been observed in photoproduction at HERA [94,95] and at the Tevatron [96,97] and these results are, as described by Oderda and Sterman, "among the most intriguing recent experimental results in QCD" [98]. These results are briefly discussed in section 4.3.1 and their possible interpretation in section 4.3.2. Complications with the definition of rapidity gap events and a possible solution by Oderda and Sterman are outlined in section 4.3.3. This has led to the development of the rapidity gap definition presented in section 4.3.4 and used in the analysis in this thesis.

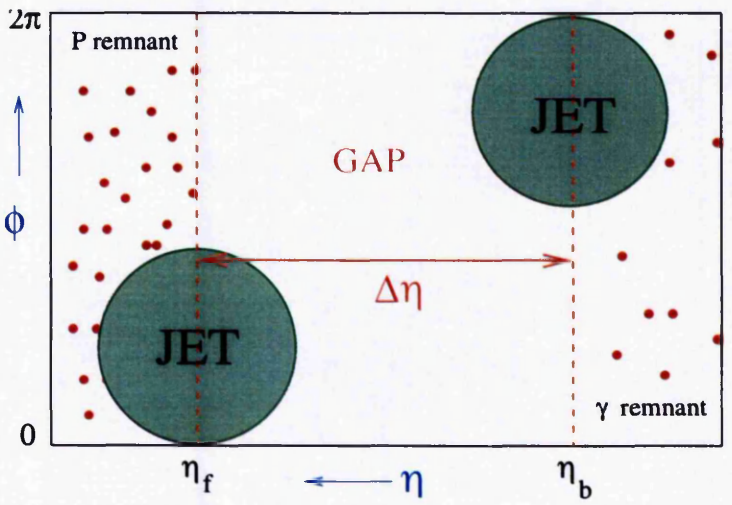

Figure 4.11: Dijet production with the exchange of a colour singlet object forming a rapidity gap in the final state as seen at the detector level.

4.3.1 Observations of Gaps Between Jets

The observable typically measured is the gap fraction, f, which is the fraction of dijet events that also have a rapidity gap between the jets:

$$f = \frac{\sigma_{\gamma p \to jet+gap+jet}}{\sigma_{\gamma p \to jet+jet}}. \tag{4.23}$$

This is a useful variable because some theoretical and experimental uncertainties cancel and the kinematic effects of dijet production are factored out. At HERA, the gap fraction has been measured by both H1 and ZEUS at $W_{\gamma p} \sim 200$ GeV. Photoproduction events are studied because the photon is required to behave hadronically for pomeron exchange to occur. Two high P_T jets were required ($P_T^2 \sim -t$), defined using a cone algorithm. A rapidity gap was defined as the absence of any final state particles between the jet edges, above a certain low threshold energy. The gap fraction measured by ZEUS and H1 as a function of the jet separation, $\Delta\eta$, is shown in figure 4.12. An excess of events of about 7% was found above that expected from standard γp processes at large $\Delta\eta$. At the Tevatron a similar approach is taken

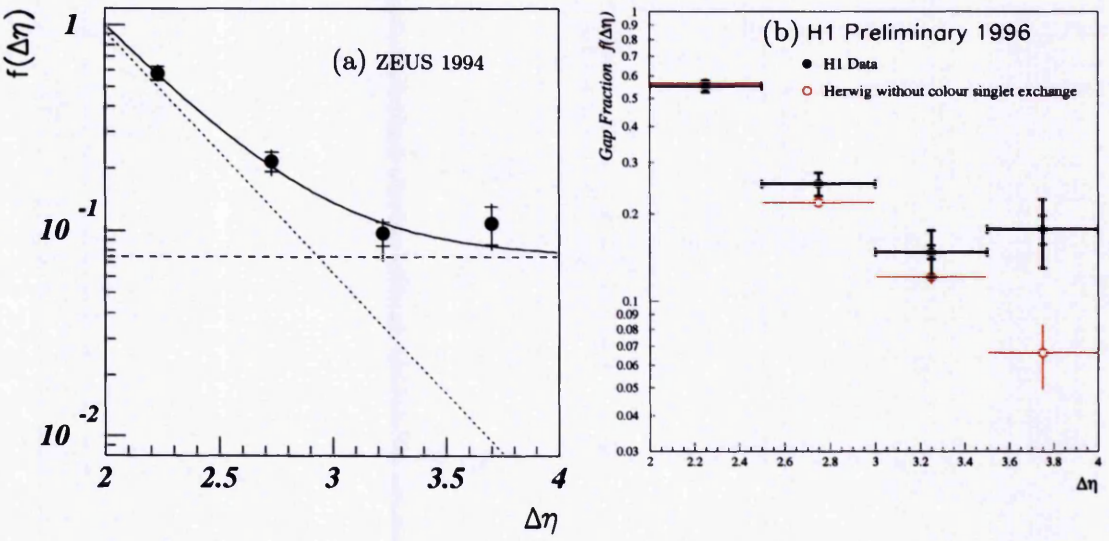

Figure 4.12: The gap fraction, f, as a function of $\Delta\eta$, measured by (a) ZEUS and (b) H1.

and a multiplicity definition is also used to define a rapidity gap. Both CDF and DØ observe a gap fraction of $\sim 1\%$ at s =1800 GeV and of $\sim 3\%$ at s =630 GeV.

4.3.2 Models of Gaps Between Jets

The simplest model for dijet gaps is two-gluon exchange, illustrated in figure 4.13(a). This was originally suggested by Bjorken [93] as a possible background to searches for WW scattering or Higgs production from WW fusion. Bjorken predicted that the magnitude of the gap fraction would be given by

$$f \sim \mathcal{S} \cdot \mathcal{O}\left(\frac{\alpha_S(P_T)}{\pi}\right) \tag{4.24}$$

where $\mathcal{S}$ is the gap survival probability, which he estimated to be ~ 0.1. He concluded that $\sim 0.1\% - 1\%$ of dijet events would have rapidity gaps, but that this could be increased by the addition of higher order corrections, such as those from the BFKL equation, shown in figure 4.13(b).

The association of rapidity gaps with pomeron exchange has already been discussed.

However, the cross section for the 'soft' pomeron falls sharply with increasing $|t|$. From equation 4.10 the cross section falls as

$$\frac{\mathrm{d}\sigma}{\mathrm{d}t} \simeq s^{2(1.08+0.25t)} \tag{4.25}$$

which leads to a vanishingly small cross section at the high values of $|t|$ required to produce jets. However, the hard scale does make it possible to use perturbative QCD. The BFKL LLA colour singlet exchange cross section for the elastic scattering of two partons as computed by Mueller and Tang [92] is:

$$\frac{d\sigma(qq \rightarrow qq)}{dt} \approx (C_F\alpha_s)^4 \frac{2\pi^3}{t^2} \frac{\exp(2\omega_0 y)}{(7\alpha_s C_A \zeta(3) y)^3} \tag{4.26}$$

for $\Delta\eta \gg 1$, where $\omega_0 = C_A(4\ln 2/\pi)\alpha_s$, $y = \Delta\eta = \ln\left(\frac{\hat{s}}{-t}\right)$ and $\hat{s}$ is the parton-parton centre-of-mass energy. The values of α_s are free parameters and can be chosen independently. The value of α_s in the prefactor of equation 4.26 is set to $\alpha_s = 0.18$, for the analysis in this thesis. This value is also chosen for α_s in the main part of the equation, corresponding to a hard pomeron intercept of 1.48. The value chosen has been found to give good agreement with both the Tevatron data on gaps between jets [99] and with the measurement of double dissociative diffractive events at large t [100]. This BFKL prediction will be compared with the measurements made in this thesis.

4.3.3 Energy Flow Between Jets

The understanding of rapidity gap events is complicated by the possibility of further parton-parton interactions. If a rapidity gap is formed in the hard scatter, this can be destroyed by a soft parton exchanged between the two outgoing beam remnants, as shown in figure 4.14. Multiple interactions are poorly understood and their effects cannot be experimentally separated from the gap production mechanism. One theoretical model is to consider this effect as an overall factor, independent of the hard scatter, the gap survival probability. The decrease in the gap survival

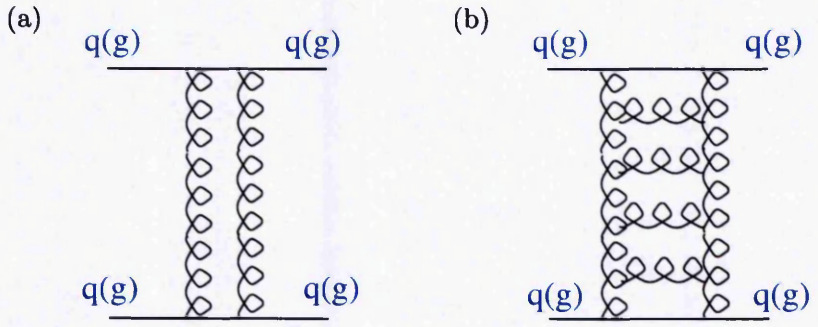

Figure 4.13: (a) 2-gluon exchange (b) Higher Order Corrections from the BFKL equation.

probability with centre-of-mass energy may explain why the observed gap fraction is much higher at HERA than at the Tevatron and is higher at 630 GeV than 1800 GeV.

A further complication is that existing definitions of rapidity gaps are not infra-red safe. Even the softest gluon carries colour and so the definition of the colour content of the hard scatter is problematic. A solution suggested by Oderda and Sterman [98] is to identify rapidity gaps by the energy flow in the interjet region, Q_C. Rapidity gap events will have a small Q_C. Q_C is an infra-red safe observable, whereas a multiplicity is not. This method also has the advantage that the calculated gap fraction can be generalised to include the perturbative part of the survival probability.

The cross section can be treated using factorisation theorems and if $Q_c \gg \Lambda_{\mathrm{QCD}}$ it is perturbatively calculable. If $P_T \gg Q_c \gg \Lambda_{\mathrm{QCD}}$ then there are two perturbative scales, and logarithms in their ratio, P_T/Q_c, can be summed. This resummation allows the concept of hard colour singlet exchange to be generalised. In the Regge limit the dominant exchange is purely colour singlet. This method is complementary to the BFKL approach, because both deal with the resummation of gluonic radiation.

Events with low Q_c would be counted as gap events by the definitions used at HERA

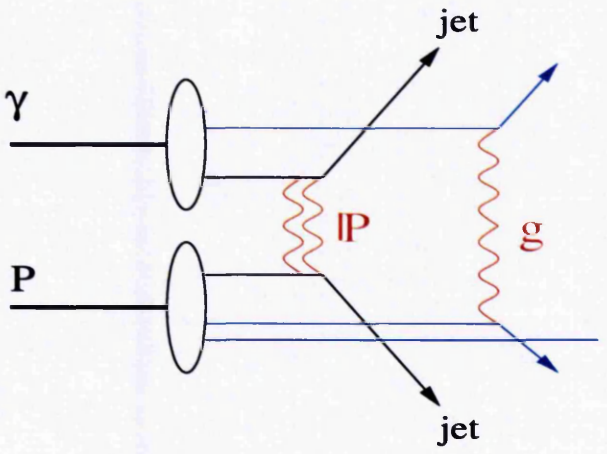

Figure 4.14: A diagram of the formation of a rapidity gap by pomeron exchange which is then destroyed by further parton-parton interactions.

and the Tevatron. Oderda [101] found a reasonable agreement with the ZEUS data, if the fraction of events with $Q_c < 350$ MeV was compared to the measured gap fraction, as shown in figure 4.15.

4.3.4 Definition of Rapidity Gap Events

The concept of defining rapidity gap events in terms of an energy flow between the jets was used as the basis of the rapidity gap definition used in this analysis. Rapidity gap events were defined by the following procedure:

1. Use the k_t algorithm in the inclusive mode, assigning each particle in the final state (excluding the scattered electron) to one and only one jet.

2. Take the two highest P_T jets to be the dijet pair.

3. Sum the E_T of all jets whose centre is between the two jet centres in rapidity to form the quantity E_T^{gap}:

$$E_T^{gap} = \sum E_T^{jets}, \quad \eta_b^{jet} < \eta^{jet} < \eta_f^{jet}. \tag{4.27}$$

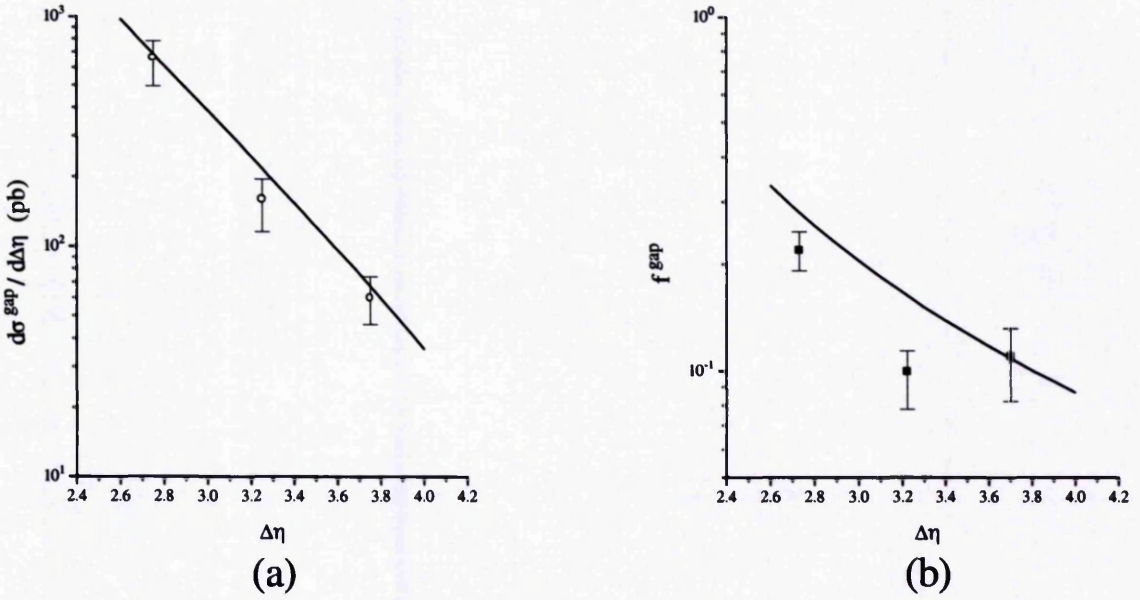

Figure 4.15: ZEUS data on (a) the gap cross section and (b) the gap fraction compared with Oderda's results identifing a gap event by $Q_c < 350$ MeV.

4. Define a rapidity gap event to be an event in which

$$E_T^{gap} < E_T^{cut} \tag{4.28}$$

where E_T^{cut} is some small amount of energy, but where $E_T^{cut} > \Lambda_{\rm QCD}$.

The consequence is that a rapidity gap event is now defined in a manner which is infra-red safe, because it is defined in terms of summed energy and in addition uses the k_t algorithm.

Using this definition, the area of $\eta - \phi$ space over which the energy flow is summed is as large as possible. This means that the probability of a random fluctuation in the final state of a colour-exchange event forming a rapidity gap event is at a minimum. In previous HERA measurements only the rapidity region between the jet edges was considered and consequently a jet separation of $\Delta\eta > 3.5$ was needed to see an excess over the background. The new definition allows this $\Delta\eta$ cut to be relaxed and so an excess of colour singlet events may be searched for over a larger $\Delta\eta$ range and a large improvement in the available statistics results.

Summing the transverse energy flow after running the k_t algorithm rather than directly summing the energy flow of particles has two main advantages. Firstly, the definition is less sensitive to activity at the edge of the gap. In a colour singlet event there is no radiation between the jets but there can be radiation from the colour strings between the jet centres and the beam remnants. From these colour strings it is possible to, at most, emit radiation along the jet axes. Due to finite detector resolution this radiation can spill into the gap. However, if the radiation is included in a jet it is more likely that it will be included in a jet whose centre is outside of the gap region and so the gap will not be destroyed. Secondly, it is experimentally easier to calibrate the energy of low P_T jets rather than that of individual particles.

Chapter 5

Data Selection and Event Reconstruction

In this chapter the data selection procedure is outlined. To correct the data for detector effects a bin-by-bin correction, determined from a sample of simulated events from a Monte Carlo generator, was used. For this method to be valid, a good agreement between the data distributions and those of the Monte Carlo events must be demonstrated from the outset. To this end the Monte carlo events were reweighted where necessary. A good description of the data was achieved, which is illustrated in this chapter.

5.1 Selection Criteria

The data used in this analysis were collected by the H1 experiment during the 1996 running period. This is currently the largest sample of photoproduction data available. Events were selected from these data to produce a sample of good quality dijet photoproduction events. This is defined as the inclusive event sample. From this sample, subsets of events with low E_T^{gap} were selected and these form the gap

event samples.

The data were selected by applying a series of cuts. These cuts restrict events to the kinematic region of interest and improve the quality of the data by removing background and poorly reconstructed events. At each stage in the description of these cuts the plots show the data after all cuts have been applied. The distributions are compared to those of the simulated events from the HERWIG and PYTHIA event generators. These samples were reweighted as described in section 5.6. The normalisation of the PYTHIA sample was scaled by 0.70 so that the number of events in the sample is equal to the number of events in the data sample, after all cuts have been applied. The HERWIG sample was scaled by 1.2, for the same reason.

5.1.1 Run Selection

Data were only selected if they were recorded when all the detector components required were fully operational. These detectors were the main calorimeters (LAr and SpaCal), the tracking system (CJC1, CJC2, CIP and COP), the luminosity system and the time of flight system. Data taking runs were also excluded if the subtriggers used in the analysis were inactive or prescaled. The selected data sample has an integrated luminosity of $6.63\,\mathrm{pb}^{-1}$.

5.1.2 Subtrigger Selection

The H1 trigger system is described in section 2.8. Events were selected if they had been saved by one of two subtriggers, s50 and s83. These both save photoproduction events by requiring an electron to have been detected in the 33 m electron tagger. This is not a sufficient condition to reduce the event rate to a level that can be saved by the H1 readout system, so both subtriggers have additional requirements.

s83 requires that the z-position of the vertex is well reconstructed and that at least three tracks are detected in the central tracker. s50 requires a deposit of electromagnetic energy in the SpaCal. In addition, both subtriggers have timing requirements that veto the vast majority of background from non-beam-beam collision events.

5.1.3 Event Vertex

To further reduce the background from non-beam-beam collision events the reconstructed z-position of the vertex was required to be close to the interaction point: $\pm$ 35 cm of the nominal position of $z = -1$ cm. This selection removes the tails of the distribution, which can come from satellite bunches; these are not included in the detector simulation. The vertex may have been reconstructed using tracks from either the central or forward tracker. In addition, at least one good quality track must be linked to the vertex position. The distribution of the reconstructed z-position of the vertex is shown in figure 5.1. The Monte Carlo event samples have been reweighted to give the best description of this distribution.

5.1.4 Selection of Photoproduction Events

Photoproduction events were selected by having detected the scattered electron in the 33m electron tagger. This procedure ensures that the Q^2 of the emitted photon is less than 0.01 GeV^2. The position of the energy deposit, X_e, was required to be within 6.5 cm of the centre of the tagger so that it was fully contained. The variable y can be calculated from the energy of the tagged electron, E_{tag}, using

$$y = \frac{E_e - E_{tag}}{E_e} \tag{5.1}$$

where E_e is the energy of the electron beam.

The acceptance of the tagger is shown as a function of y in figure 5.2(a). To avoid the regions of low acceptance a cut of $0.30 < y < 0.65$ is made. This corresponds

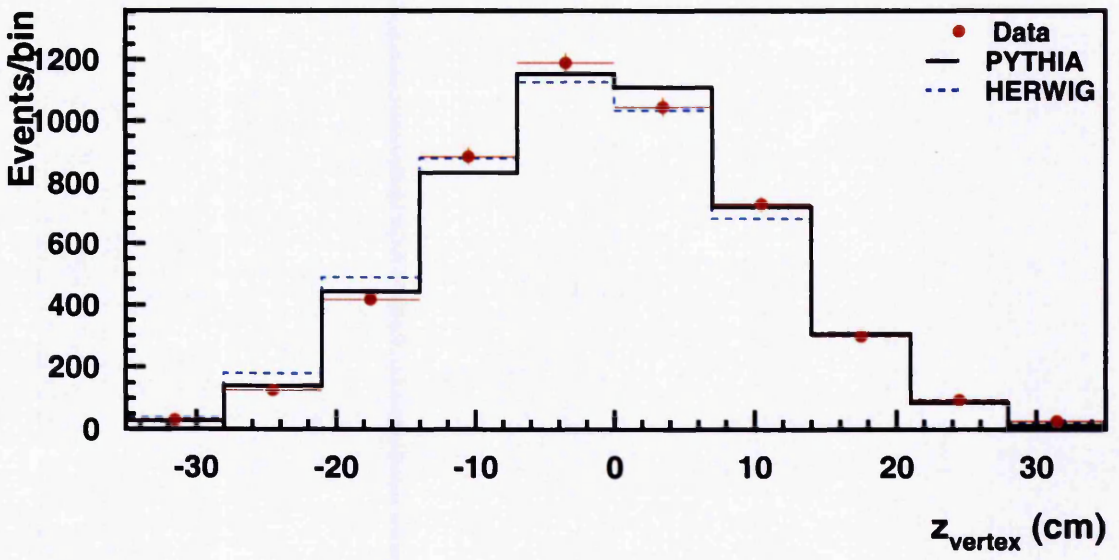

Figure 5.1: The distribution of the reconstructed z position of the event vertex of the data and of the PYTHIA and HERWIG event samples.

to a γp centre of mass energy of 165 GeV $< W <$ 243 GeV. The y distribution, measured with the tagger, is shown in figure 5.2(b).

5.1.5 Selection of Dijet Events

In order to find jets, the longitudinally invariant inclusive k_t algorithm with P_T recombination scheme was used. This associates every particle[1] in the event (excluding the scattered electron) with a jet. The number of jets found agreed well between data and Monte Carlo and on average 11 jets were found by the algorithm. Events that have at least two jets were selected. The highest jet P_T was required to be greater than 6.0 GeV and the second highest jet P_T to be greater than 5.0 GeV. The jet with the larger rapidity is referred to as the forward jet and the other as the backward jet.

[1]At the detector level this may be a calorimeter cluster, track or combined object (see section 5.5).

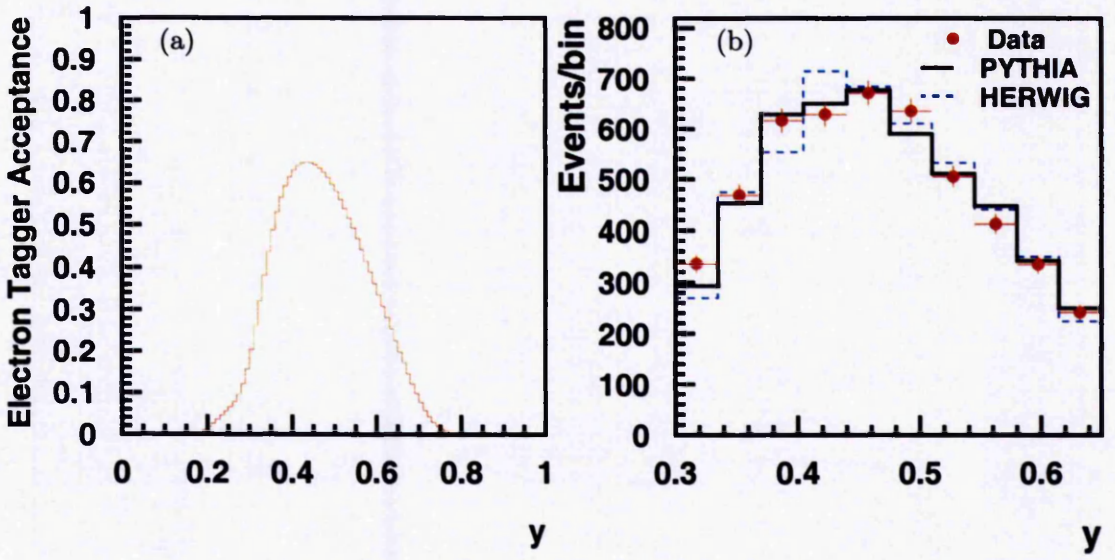

Figure 5.2: (a) The luminosity weighted acceptance of the 33m electron tagger, as a function of y, for the 1996 data taking period. (b) The y distribution, measured with the 33m electron tagger. The distributions of the HERWIG and PYTHIA event samples are also shown.

The jet P_T cut was chosen to be sufficiently high that jets could be resolved from the underlying non-jet hadronic activity. The asymmetric cut would enable the comparison of a next to leading order calculation which, for dijet events, contains terms which are logarithmic in the difference in jet P_T's. Experimentally, an asymmetric cut improves the reconstruction efficiency because usually at the hadron level both jets will have a P_T of around 6 GeV and the cut allows the event to enter the final sample even if the P_T of one jet has been smeared downwards.

Due to the boost in the proton direction the backward jet is always fully contained within the LAr calorimeter or the SpaCal. The rapidity of the forward jet was required to be $\eta^f < 2.65$ so that it is fully contained within the LAr calorimeter. The distributions of the forward and backward jet transverse energy and rapidity are shown in figure 5.3.

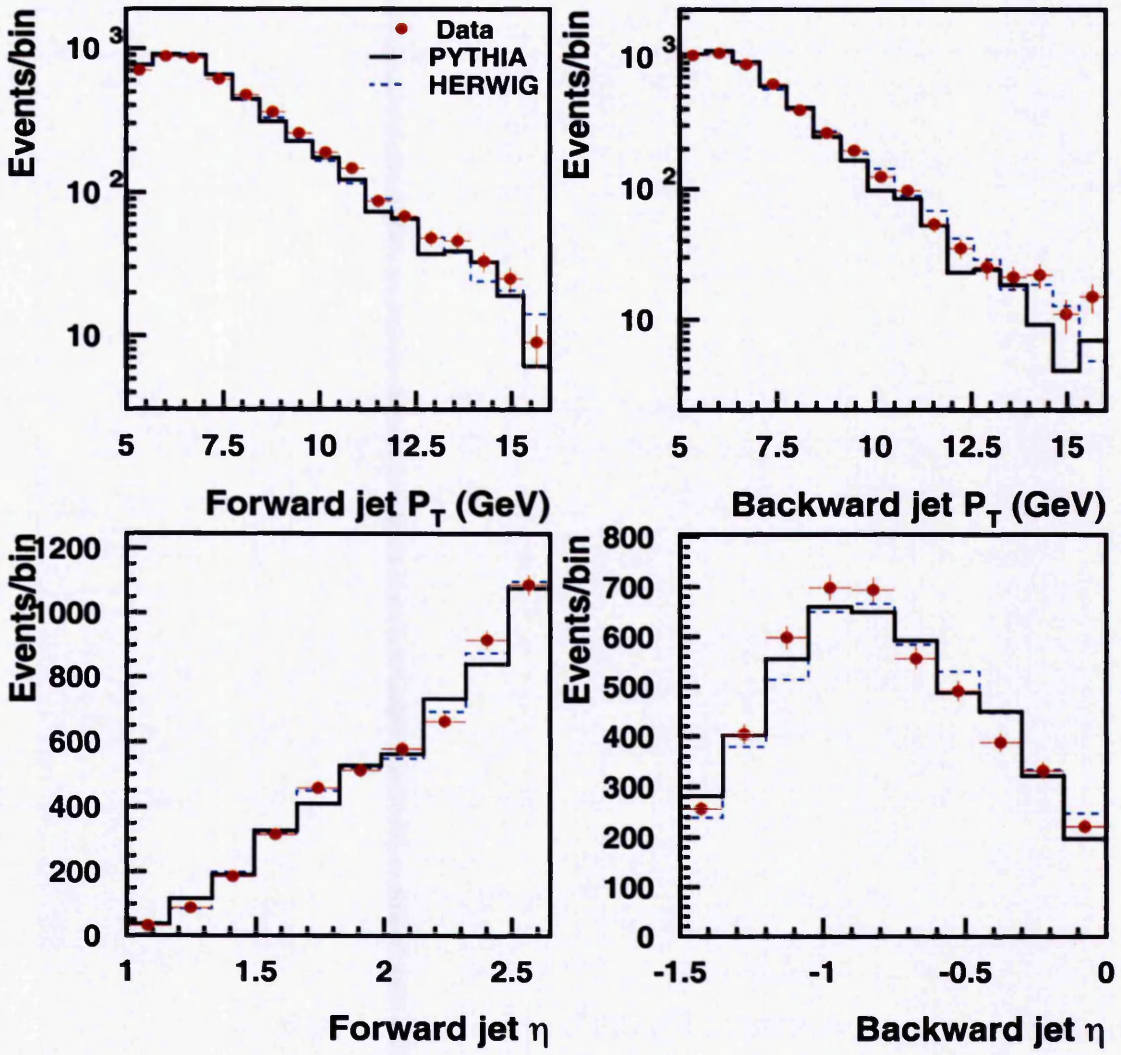

Figure 5.3: The P_T and η distributions of the forward and backward jets of the data and of the PYTHIA and HERWIG event samples.

To select a sample of widely separated dijet events the separation in rapidity of the jets was required to be $2.5 < \Delta\eta < 4.0$. The upper limit is set by the finite acceptance of the detector. The distribution in $\Delta\eta$ is shown in figure 5.4(a) and falls rapidly with $\Delta\eta$. The distribution in $\Delta\phi$ is shown in figure 5.4(b). The dijets are predominantly back-to-back in the transverse plane; a reasonable description is achieved by the Monte Carlo event samples.

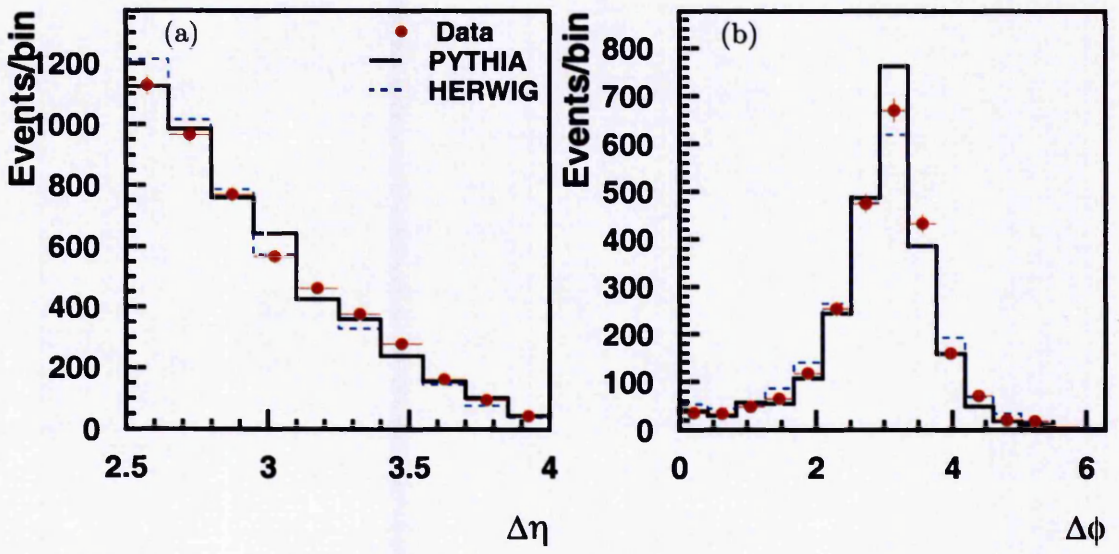

Figure 5.4: The (a) $\Delta\eta$ and (b) $\Delta\phi$ distributions of the data and of the PYTHIA and HERWIG event samples.

5.1.6 Background Rejection

The timing requirements that form part of the subtrigger conditions remove the majority of the background that comes from non-beam-beam interactions. In addition, the z-vertex requirements and the demand for two high P_T jets form a signal that is hard for background events to fake.

The total $E - P_z$ of an event, including the scattered electron, is conserved. If this is measured in a perfectly reconstructed final state, it is equal to twice the energy of the incoming electron, 55 GeV. By requiring that 40 GeV $< \Sigma(E - P_z) <$ 70 GeV, backgrounds from non-beam-beam interactions and poorly reconstructed events are further reduced. The measured $\Sigma(E-P_z)$ distribution, shown in figure 5.5(a), peaks at 56 GeV.

A hit in the electron tagger can result from bremsstrahlung events, $ep \rightarrow ep\gamma$. These can overlap with DIS ep events, thus faking photoproduction events. This background can be reduced by vetoing the scattered photon. Hence, the energy

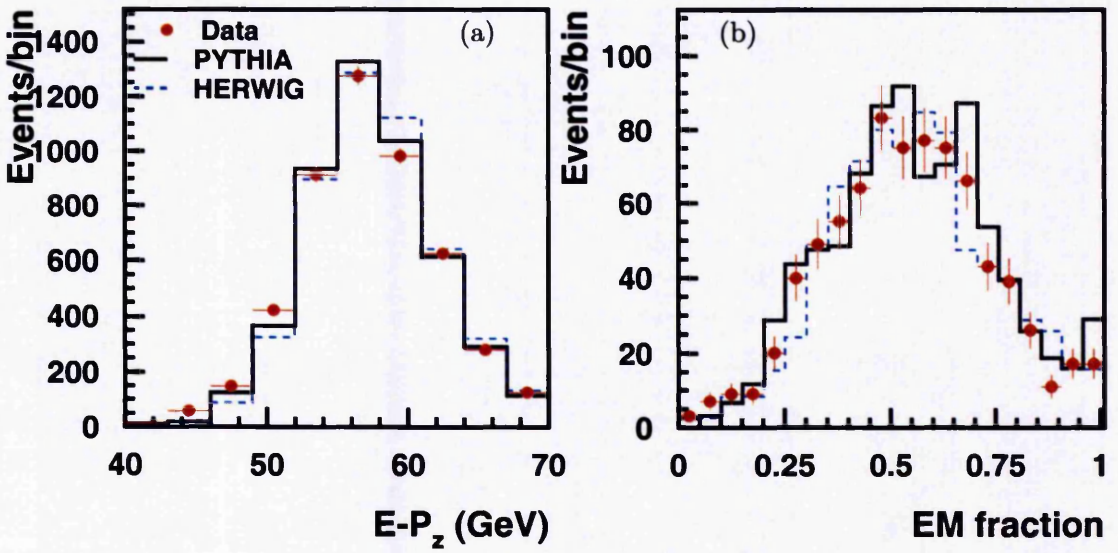

Figure 5.5: (a) The $\Sigma(E - P_z)$ distribution of the data and of the PYTHIA and HERWIG event samples. (b) The distribution of the fraction of electromagnetic energy of jets detected in the SpaCal of the data and of the PYTHIA and HERWIG event samples.

deposited in the photon tagger was required to be less than 2 GeV. The upper limit on $\Sigma(E - P_z)$ further removes this background because an additional hit in the electron tagger adds twice that energy onto the total $\Sigma(E - P_z)$.

The background from overlap events is reduced to a negligible amount by these cuts. However, any one jet DIS event will look like a rapidity gap event if the scattered electron is reconstructed as a jet. So, events were also checked for the presence of a good quality electron. In the LAr calorimeter the default electron finding algorithm (QESCAT) was run. Events were rejected if an electron of energy $E_{e'}$ was found with $E_{e'} > 9$ GeV, a good quality linked track, and $y_e < 0.9$, where

$$y_e = 1 - \frac{E_{e'}}{2E_e}(1 - cos\theta) \tag{5.2}$$

and θ is the angle of the scattered electron. 0.1% of the event sample was rejected by this cut. In the SpaCal region, DIS events are defined by reconstructing $y_{JB} > 0.9$,

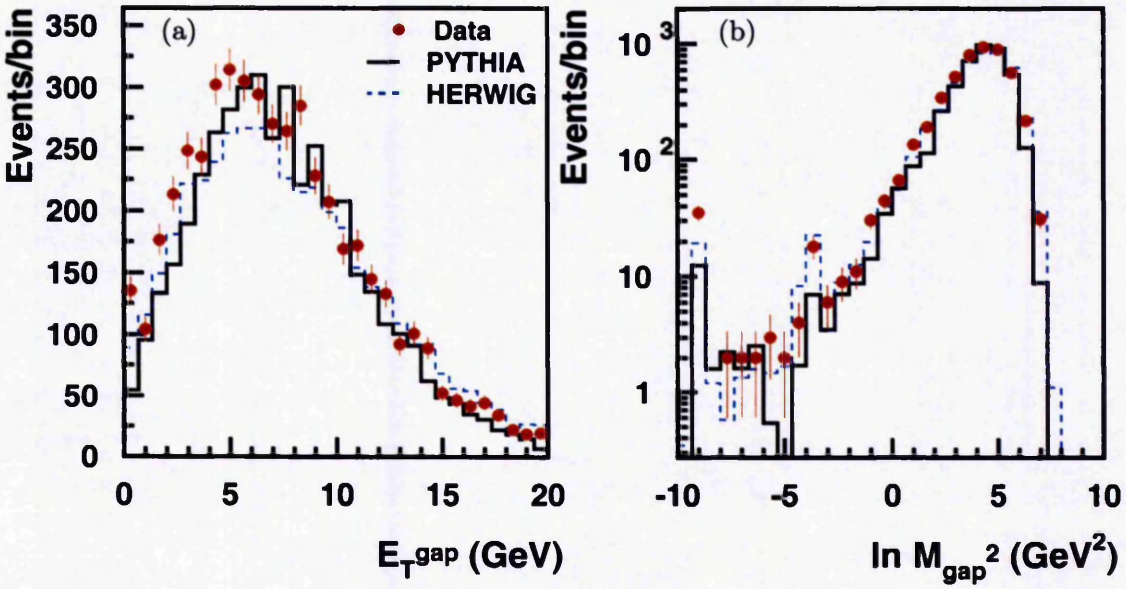

Figure 5.6: The (a) E_T^{gap} and (b) ln M_{gap}^2 distributions of the data and of the PYTHIA and HERWIG event samples, excluding colour singlet events.

where

$$y_{JB} = \frac{\sum_{hfs}(E - P_z)}{2E_e} \tag{5.3}$$

and the sum is over the entire final state, excluding the tagged electron. No events were rejected by this cut.

Finally, the fraction of the energy of jets reconstructed in the SpaCal which was in the electromagnetic section was compared to that expected from the event simulation. This comparison is shown in figure 5.5(b). An extremely good agreement is found, providing assurance that the jets reconstructed are not electrons.

5.2 Selection of Gap Events

The quantity E_T^{gap} was measured, as defined in chapter 4. This is shown in figure 5.6(a). The uncorrected data show an excess at low E_T^{gap} compared with the Monte Carlo event samples excluding additional colour singlet events. The discrep-

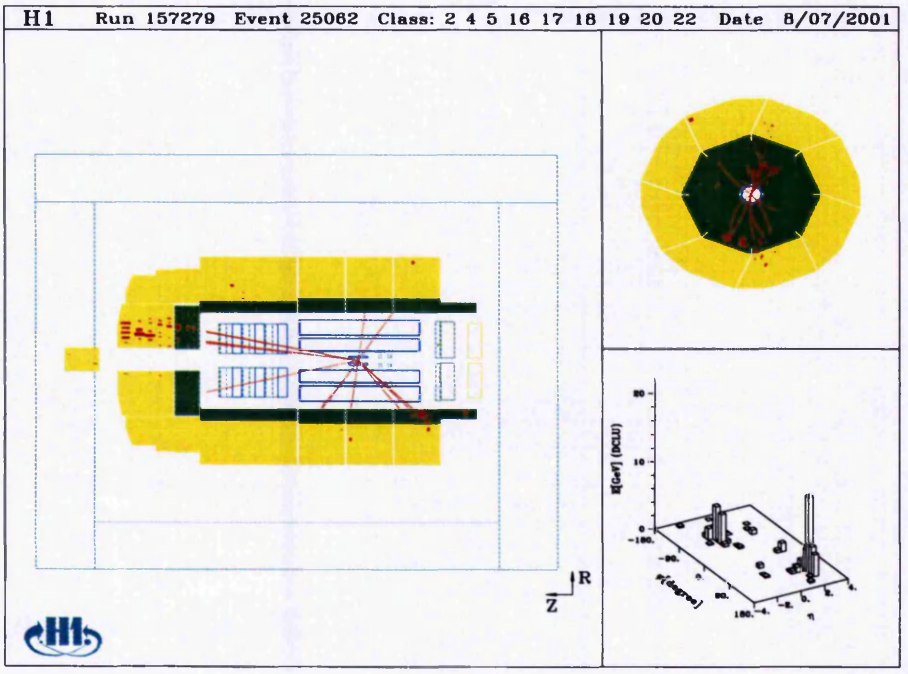

Figure 5.7: An example event from the inclusive sample, with $E_T^{gap} = 4.5$GeV. The views shown are a section through the $r-z$ plane, a section through the $r-\phi$ plane and a "lego" plot of cluster energy in $\eta - \phi$.

ancy can also be seen by plotting the invariant mass of the particles between the two jets. This is shown in figure 5.6(b). An excess is seen at low M^2_{gap}. Events with $M^2_{gap} = 0$ GeV are plotted at $M^2_{gap} = 10^{-4}$ GeV, there is also a peak corresponding to the mass of one pion in the gap.

An event display from a typical dijet event is shown in figure 5.7. In this event E_T^{gap} =4.5 GeV and particles are seen distributed between the two jets. An event display for a gap event is shown in figure 5.8. In contrast, in this event E_T^{gap} =0.2 GeV and little activity between the jets is seen.

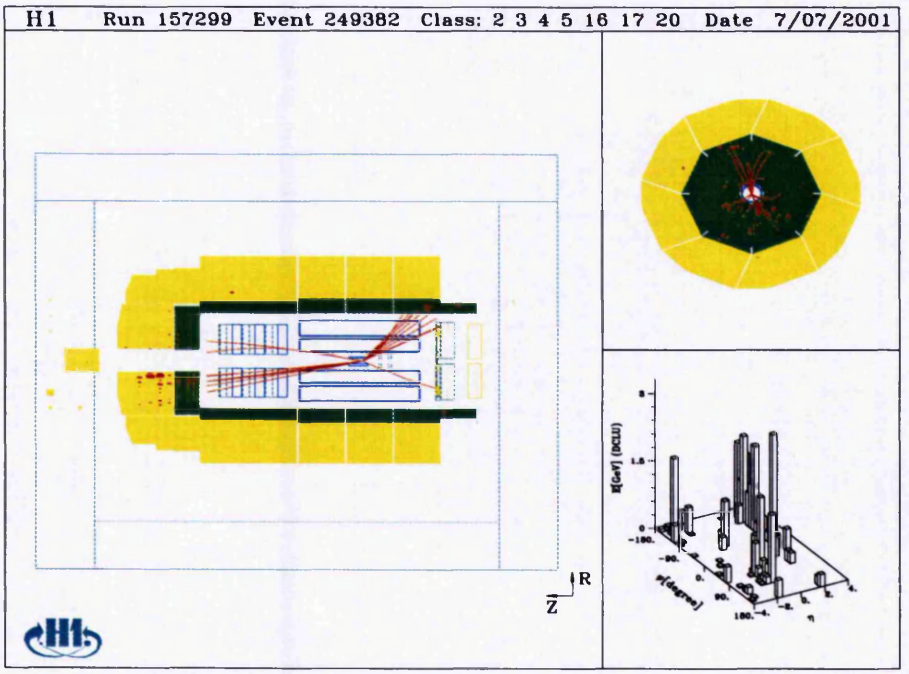

Figure 5.8: An example event from the gap sample, with $E_T^{gap} = 0.2$ GeV. The views shown are a section through the $r - z$ plane, a section through the $r - \phi$ plane and a "lego" plot of cluster energy in $\eta - \phi$.

5.3 Hadron Level Selection

A hadron level sample of Monte Carlo events is defined using the same kinematic cuts that are applied at the detector level selection. This is the definition of the measured cross sections after the data have been corrected for detector effects. The cuts are

- $Q^2 < 0.01\text{GeV}^2$
- $0.30 < y < 0.65$
- $N_{\text{jets}} \geq 2$
- $P_T^{jet\ 1} > 6.0\,\text{GeV}$, $P_T^{jet\ 2} > 5.0\,\text{GeV}$

- $\eta^{jet\ 1,2} < 2.65$
- $2.5 < \Delta\eta < 4.0$

5.4 Event Yield

The number of events per unit luminosity after all cuts (summarised in table 5.1) should be independent of time if the event selection is stable. This ensures that the HV and trigger selection is correct and time variable backgrounds have been removed. The event yield is plotted in bins of 50 nb^{-1} for the inclusive event sample and in bins of 450 nb^{-1} for a gap event sample in figure 5.9. The slightly higher event yield from bin 11 onward in figure 5.9(a), is due to the inclusion of the s50 trigger. Otherwise, the event yield is constant, as expected. In the final event sample there are 4840 events, 93 of which have $E_T^{gap} < 0.5$ GeV and 183 have $E_T^{gap} < 1.0$ GeV.

5.5 Reconstruction of the Hadronic Final State

The hadronic final state is reconstructed using both tracking and calorimetric information. A high energy particle will leave a stiff track that poorly reconstructs the particle's P_T, but the large calorimeter energy cluster will reconstruct the energy well. Conversely, a low energy particle will leave an energy deposit in the calorimeter that may be poorly reconstructed, but if it leaves a track this will reconstruct the particle's P_T well.

The algorithm used first combines calorimeter cells that are close together to form clusters. If a central track is below 2 GeV it is extrapolated to the calorimeter. The clusters in a cylinder around the track are considered. If their total energy is less than the track energy then the clusters are deleted. Otherwise, the clusters are

(1)	$N_{\text{jets}} > 1$
(2)	$P_T(1) > 6.0\,\text{GeV}$
(3)	$P_T(2) > 5.0\,\text{GeV}$
(4)	$\eta^f < 2.65$
(5)	$2.5 < \Delta\eta < 4.0$
(6)	$0.30 < y < 0.65$
(7)	$\lvert X_e \rvert < 6.5\,\text{cm}$
(8)	$-36\,\text{cm} < z_{vertex} < 34\,\text{cm}$
(9)	$N_{\text{track+vertex}} > 1$
(10)	$E_\gamma < 2.0\,\text{GeV}$
(11)	$40\,\text{GeV} < \Sigma(E - P_Z) < 70\,\text{GeV}$
(12)	veto additional electrons

Table 5.1: The inclusive event selection.

deleted, starting with the one closest to the track, until the combined energy of the deleted clusters is greater than the track energy. Tracks with energy greater than 2 GeV are killed to avoid double counting.

Noise in the LAr calorimeter mainly produces low energy isolated clusters. To reduce their effect, clusters are removed if they are at an angle of $\theta_{\text{cl}} < 0.26$ ($\theta_{\text{cl}} > 0.26$) and they are below 400 MeV (800 MeV) and within a radius of 40 cm (20 cm) from the cluster there is less than 400 MeV (800 MeV) deposited.

5.5.1 Jet Calibration

Ideally, the reconstructed value of the P_T of a jet would be equal to the true value of the jet's P_T, as defined at the hadron level. However, energy is lost from the reconstruction as the particles pass through the detector. The LAr calorimeter

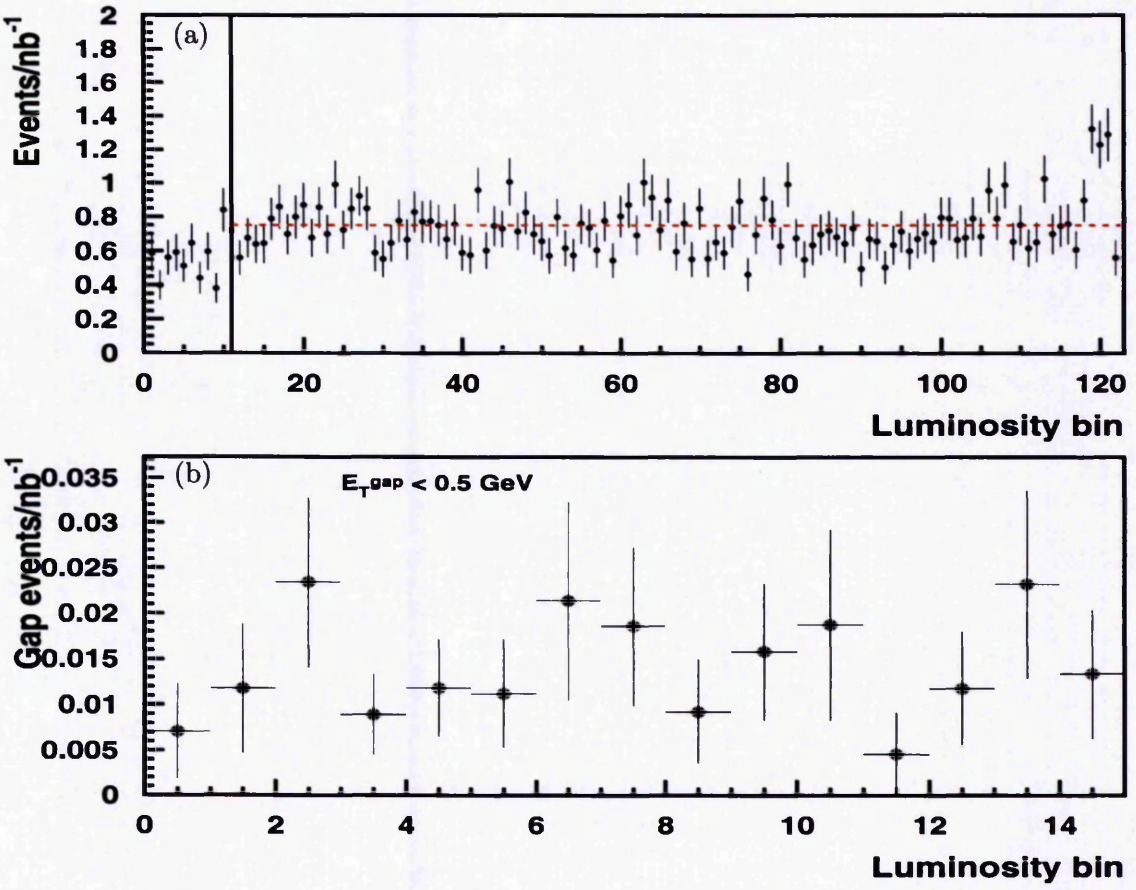

Figure 5.9: The event yield for (a) the inclusive event sample and (b) those events with E_T^{gap} <0.5 GeV.

has been carefully calibrated to improve the energy measurement, but even after this some difference between the hadron level and detector level values remains. Figure 5.10(a) shows the ratio of the reconstructed to hadron level P_T of the jets as a function of z_{impact}. z_{impact} corresponds to the position in z where the jet axis enters the calorimeter. Choosing this variable reduces the smearing effect of the vertex position obtained if the jet θ is used.

A P_T independent calibration, previously used for high P_T jets [102], was found to improve the P_T reconstruction; this improvement is shown in figure 5.10(b). After the calibration the difference between the hadron and detector level values is within

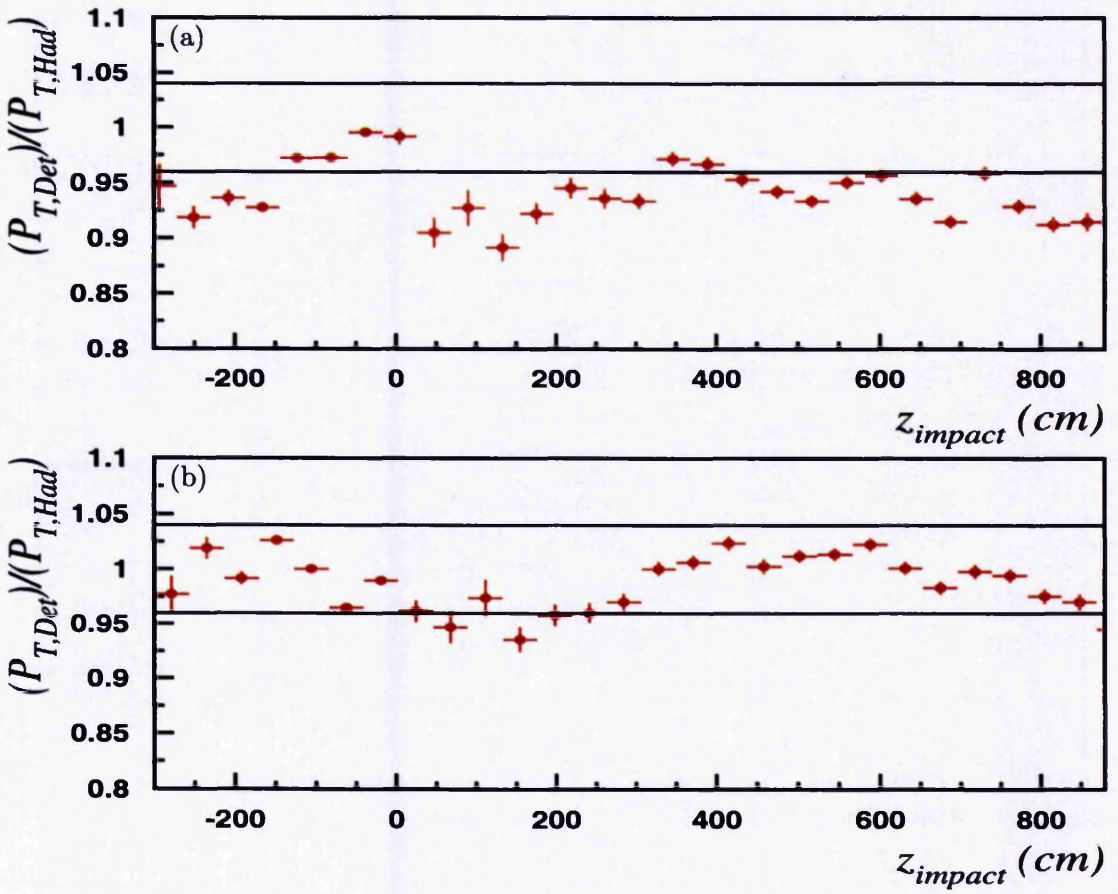

Figure 5.10: The ratio of P_T^{jet} at the detector level to that at the hadron level, from PYTHIA, as a function of the z_{impact} of the jet (a) without and (b) with the calibration. The horizontal lines show the uncertainty quoted on the energy scale ($\pm 4\%$).

the uncertainty quoted on the LAr calorimeter hadronic energy scale (4%).

The resolution of a variable is found by plotting the ratio of the reconstructed and generated values of the variable for all events which pass the hadron level cuts and taking the spread. This distribution is plotted, after calibration, for the P_T and η of the forward and backward jets in figure 5.11. The η resolution is unchanged by the calibration. The significant improvement in the mean value of the jet P_T is illustrated in table 5.2; the effect on the resolution is small.

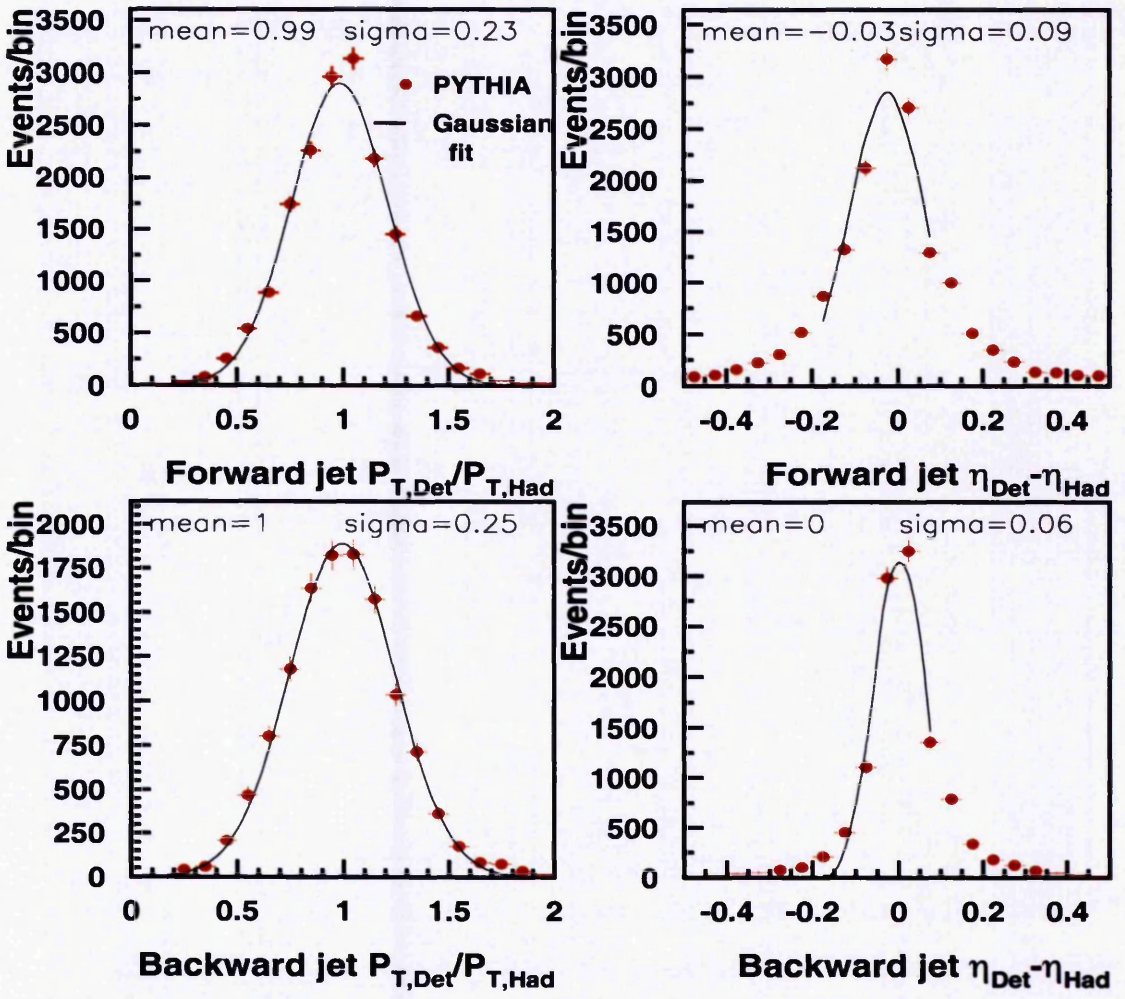

Figure 5.11: The resolution of $P_T^{jetf,b}$ and $\eta^{jetf,b}$ measured in PYTHIA.

5.5.2 Measurement of $\Sigma(E - P_z)$

The value of y can be calculated as in equation 5.1, or alternatively from the hadronic final state:

$$y = \frac{\sum_{hfs}(E - P_z)}{2E_e} \tag{5.4}$$

where the sum is over everything except the electron taggers. The ratio of y measured using these two methods is plotted in figure 5.12, for both the data and Monte Carlo event samples. While the ratio deviates slightly from unity, a good agreement

η^{jet} range	Before Calibration		After Calibration	
	Mean	Sigma	Mean	Sigma
$\eta^{\text{b}} < -1.2$	0.91	0.22	1.00	0.25
$-1.2 < \eta^{\text{b}} < 2.35$	0.96	0.24	0.99	0.25
$-1.2 < \eta^{\text{f}} < 2.35$	0.93	0.21	1.00	0.23
$\eta^{\text{f}} > 2.35$	0.90	0.20	0.97	0.21

Table 5.2: The P_T resolution before and after calibration for the backward and forward jet in different rapidity regions.

is seen between Monte Carlo and data. The $\sum_{hfs}(E - P_z)$ was measured from the sum of the $E - P_z$ of all jets. The calibration described in the previous section was applied to every jet for consistency. This made no observable difference to this distribution.

5.5.3 Measurement of x_p^{jets} and x_γ^{jets}

Two variables x_p^{jets} and x_γ^{jets} are defined as the fractional longitudinal momentum of the proton and photon which participate in the production of the two highest P_T jets :

$$x_p^{jets} = \frac{\sum_{jet1,2}(E + P_z)}{2E_p} \tag{5.5}$$

$$x_\gamma^{jets} = \frac{\sum_{jet1,2}(E - P_z)}{\sum_{hfs}(E - P_z)} \tag{5.6}$$

where E_p is the energy of the incoming proton and the sum in the denominator of x_γ^{jets} is over the entire final state, excluding the scattered electron. The hadronic final state rather than the scattered electron energy is used to calculate x_γ^{jets} because uncertainties in the energy measurements will partially cancel. At leading order, x_p^{jets} and x_γ^{jets} are approximately equal to x (section 3.1) and x_γ (section 3.4) but they are also well defined at all orders. The distributions of x_p^{jets} and x_γ^{jets} are shown

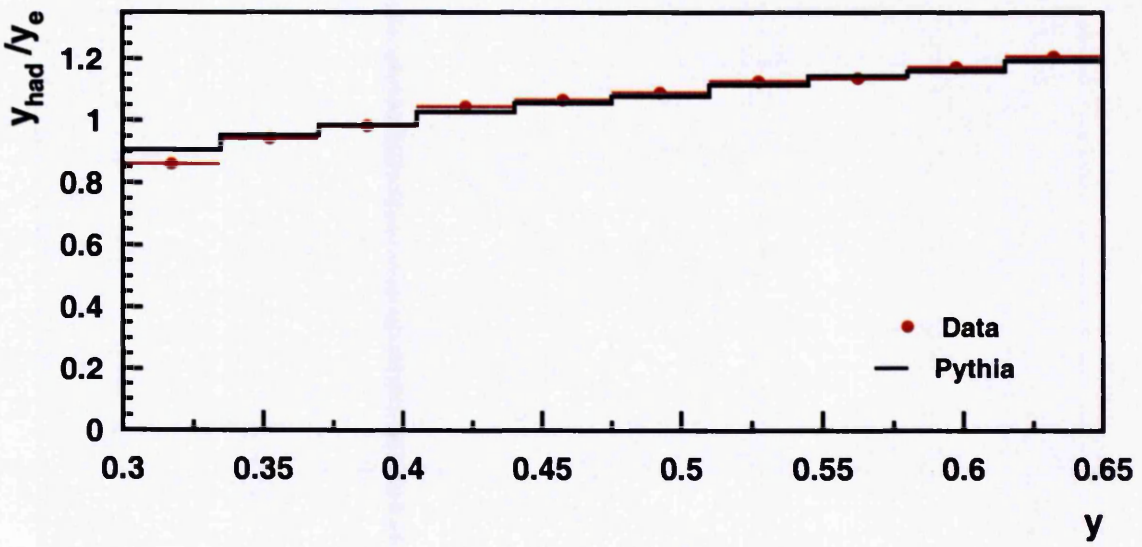

Figure 5.12: The ratio of y calculated using the hadronic final state to y calculated using the tagged electron, measured in the data and in the PYTHIA event sample.

in figure 5.13. The differential distributions are also well described; for example, figure 5.14 shows x_p^{jets} measured in bins of $\Delta\eta$.

5.6 Tuning of the Monte Carlo Simulation of the Data.

Both PYTHIA and HERWIG generate resolved and direct interactions separately. The event samples were generated using the GRV-LO PDFs for the photon [103] and the proton [104]. $11.8\,\mathrm{pb}^{-1}$ ($7.3\,\mathrm{pb}^{-1}$) of resolved events and $16.4\,\mathrm{pb}^{-1}$ ($8.0\,\mathrm{pb}^{-1}$) of direct events were generated using PYTHIA 5.7 (HERWIG 6.1) and these were mixed according to their cross sections. After the hadron level cuts, described in section 5.3, the generated ratio of resolved to direct events was 1:0.27 in HERWIG and 1:0.11 in PYTHIA. The matrix elements are divergent and are regularised by a cut on the minimum P_T generated, P_T^{min}. This was set to $P_T^{min} = 2.2$ GeV in

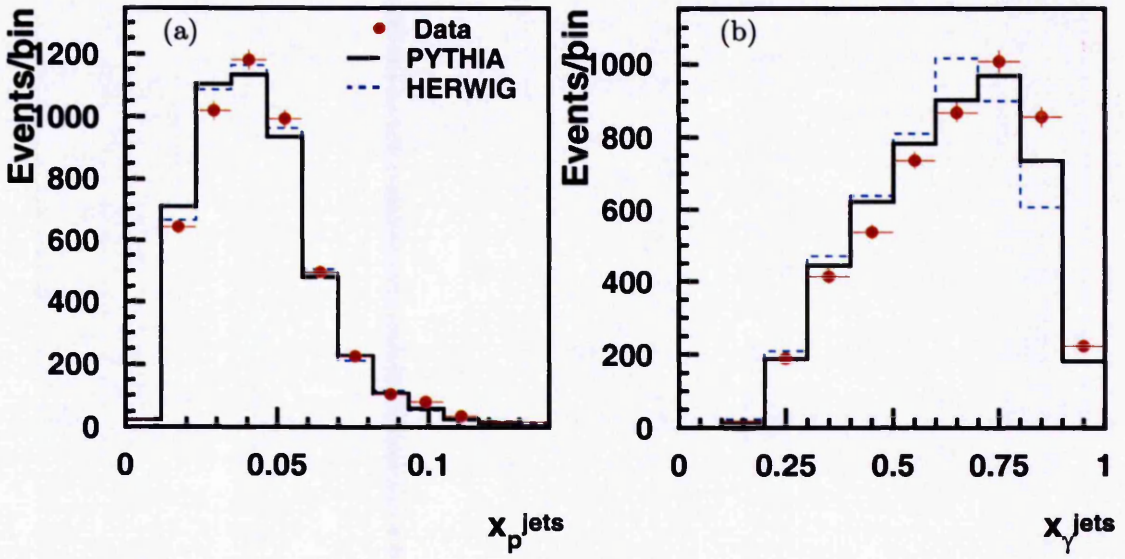

Figure 5.13: The (a) x_p^{jets} and (b) x_γ^{jets} distributions of the data and of the PYTHIA and HERWIG event samples.

PYTHIA and $P_T^{min} = 1.8$ GeV in HERWIG.

5.6.1 Multiple Interactions

As discussed in section 3.6, it is necessary to include multiple interactions in the Monte Carlo models in order to describe the energy flow seen in the data. The rate of multiple interactions in both models can be tuned using the P_T^{mi} parameter. In HERWIG this must currently be set equal to P_T^{min}.

The value of P_T^{mi} was tuned for both the HERWIG and PYTHIA generators to give the best possible description of the data used in this analysis. A number of variables are sensitive to the rate of multiple interactions, including x_γ^{jets} and the rapidity of the jets. However, the main distributions used were the jet profiles. These measure the energy flow in and around the jets. The energy flow depends both on the energy deposited per multiple interaction and the rate of multiple interactions.

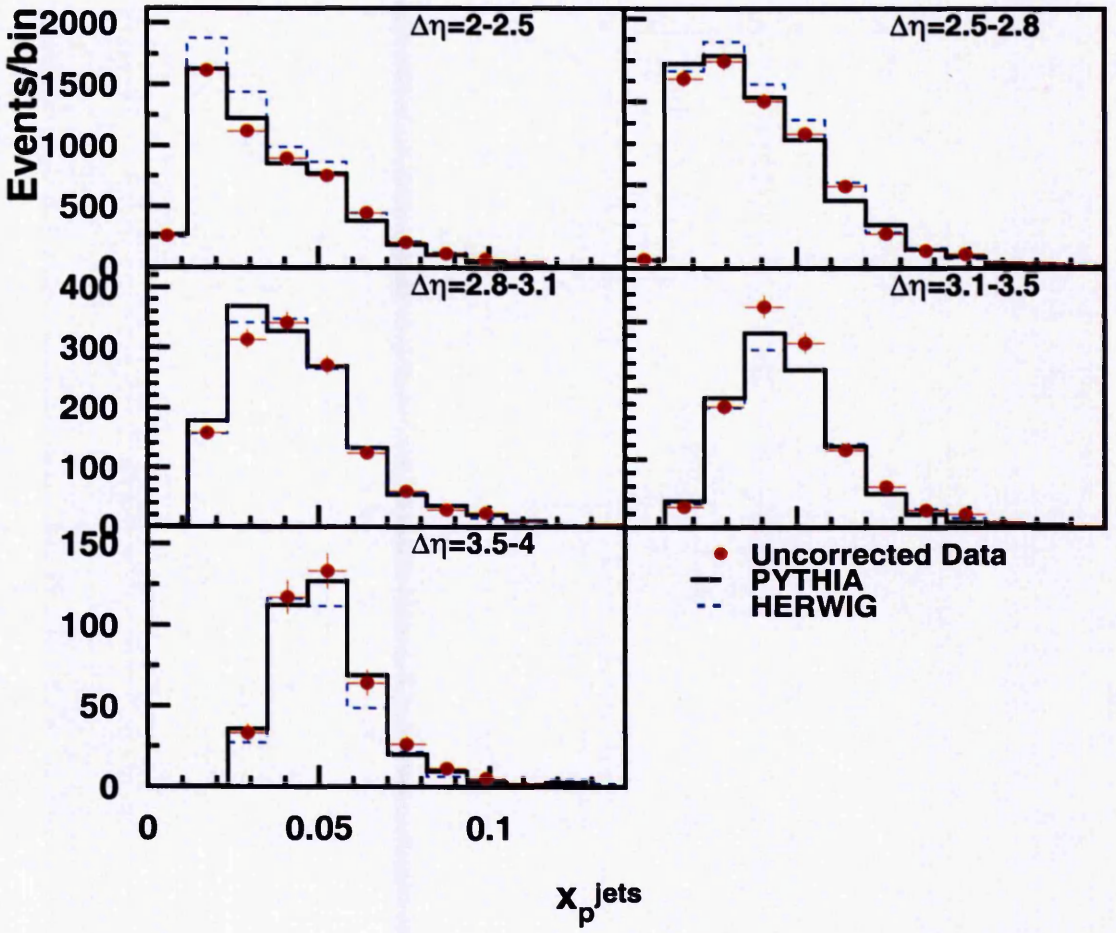

Figure 5.14: The x_p^{jets} distribution, measured in bins of $\Delta\eta$, of the data sample compared to the PYTHIA and HERWIG event samples.

The jet profiles of the forward jet generated by HERWIG with no multiple interactions and with P_T^{mi} set to 1.8 GeV are shown in figure 5.15. The jet η profile plots $\delta\eta = \eta^{cluster} - \eta^{jet}$ weighted by the transverse energy of the cluster for all clusters that are within one radian in ϕ of the jet axis. A similar process is followed for the ϕ profile. The distributions are clearly sensitive to the inclusion of multiple interactions.

The jet profiles for both the forward and backward jets are compared to those from the HERWIG and PYTHIA simulations in figure 5.16. A good description

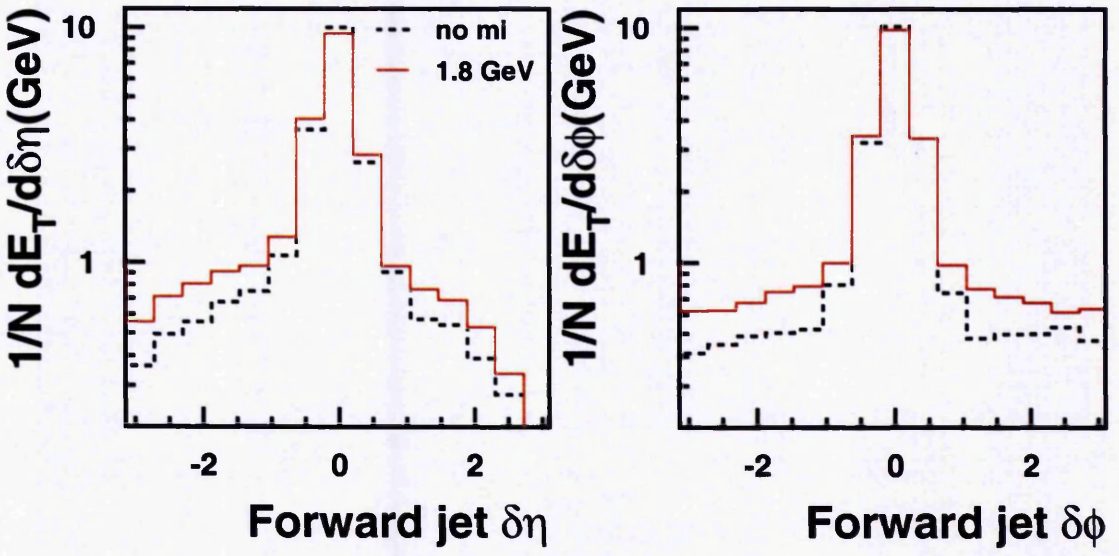

Figure 5.15: The forward jet profiles generated by HERWIG with no multiple interactions and with P_T^{mi} set to 1.8 GeV.

of the jet pedestal is seen using these tunings of $P_T^{mi} = 1.5\,\text{GeV}$ in PYTHIA and $P_T^{mi} = 1.8\,\text{GeV}$ in HERWIG. The best description of the jet η distribution, shown in figure 5.3, is also obtained.

5.6.2 The y Distribution

Figure 5.2 compared the y distribution to that of the HERWIG and PYTHIA event samples after they had been reweighted in y to improve their distributions. The unreweighted distributions of the Monte Carlo event samples disagree slightly with the data as shown in figure 5.17(a). The reweighting is used for the data correction only and not for the model comparisons. On average the correction is 2% per bin and the largest reweight is 5% in the lowest y bin.

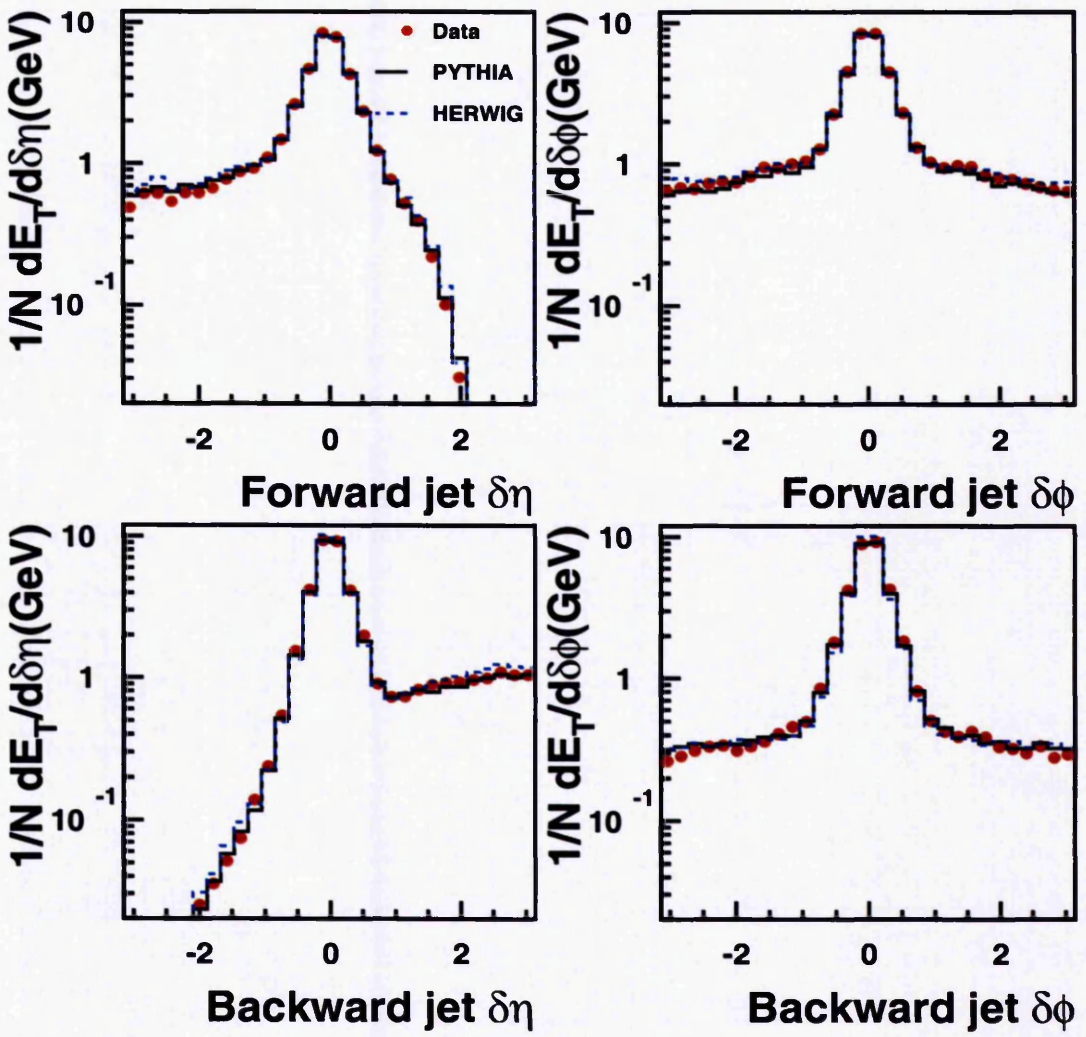

Figure 5.16: The forward and backward jet profiles compared to those of the HERWIG and PYTHIA event samples.

5.6.3 The x_γ^{jets} Distribution

The x_γ^{jets} distribution of the data is poorly described by both the HERWIG and PYTHIA event samples, as shown in figure 5.17(b). This is not surprising because dijet cross sections have not been measured differentially in x_γ^{jets} in this kinematic region before. The disagreement is discussed in more detail in chapter 7. The x_γ^{jets}

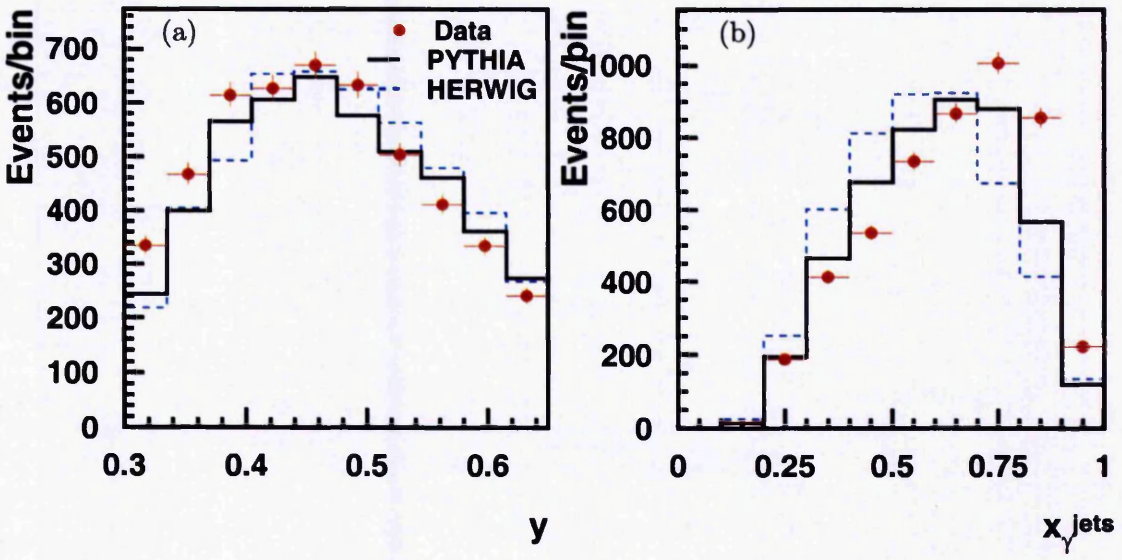

Figure 5.17: The y and x_γ^{jets} distributions compared to the unreweighted distributions of the HERWIG and PYTHIA event samples.

distributions of both the HERWIG and PYTHIA event samples were reweighted for the data correction process. This weighting was applied in figure 5.13.

5.6.4 Addition of Colour Singlet Events

In order for the HERWIG and PYTHIA event samples to describe the E_T^{gap} distribution, shown in figure 5.6, additional events with colour singlet exchange are required. HERWIG includes the BFKL LLA colour singlet exchange cross section. $174\,\mathrm{pb}^{-1}$ of this was generated, with $\alpha_s = 0.18$, and added to the standard HERWIG events with the cross section scaled by a factor of 0.8. The cross section normalisation was chosen so that the Monte Carlo described the number of events in the data with $E_T^{gap} < 0.5$ GeV.

No such process is available in the PYTHIA generator and high-t photon exchange was used instead. $65000\,\mathrm{pb}^{-1}$ was generated and added to the standard PYTHIA events with the cross section scaled by a factor of 1200, chosen to describe the data

at $E_T^{gap} < 0.5$ GeV. This is an electromagnetic process and so the cross section is much too small. However, this is perfectly acceptable for data correction purposes because for this it is only important that the data distributions are fully described.

Chapter 6

Cross Section Measurements

In this chapter a description is given of the analysis procedure used to measure the dijet cross sections differentially in $\Delta\eta$, x_p^{jets}, x_γ^{jets} and E_T^{gap}. The differential cross section in bin i, σ_i, was calculated from:

$$\sigma_i = \frac{N_i}{A_i \epsilon_i b_i \mathcal{L}} \tag{6.1}$$

where N_i is the number of data events in the bin, A_i is the detector acceptance in the bin, ϵ_i is the trigger efficiency in the bin, b_i is the width of the bin and $\mathcal{L}$ is the integrated luminosity of the data sample. The cross section for the rapidity gap event samples and the gap fractions are also measured.

The good agreement between the data and Monte Carlo event samples shown in chapter 5 enables the data to be corrected on a bin-by-bin basis for detector acceptance, as shown in equation 6.1, using the Monte Carlo events to calculate A_i and ϵ_i. However, a further requirement is that the bin widths must be chosen such that migrations between the bins are sufficiently small. The bin widths were chosen according to the criteria discussed in section 6.1. The detector acceptance and trigger efficiency for each bin were then determined. Finally, the uncertainties on the measurements were studied.

6.1 Resolution and Migrations

The resolution of the observables, the bin purities and the stability of migrations between the bins were studied. The choice of binning for the measurements must allow sufficient statistics in each bin, the migrations between the bins to be sufficiently small and the resolution of the variables to be better than the bin size.

6.1.1 Resolution in each Bin

The resolution of $\Delta\eta$, x_p^{jets}, x_γ^{jets} and E_T^{gap} is shown in figure 6.1, by plotting the ratio of the reconstructed and generated values of the variable. The mean value of the ratio is plotted for each bin used in this analysis in figure 6.2. The mean values are all within 3% of 1.0. The resolution of the variable is shown as the vertical length of the error bar and is also shown below the point. The resolution of the variable is better than the bin width for each bin. The resolution in x_γ^{jets} improves greatly at high values of x_γ^{jets} because, by definition, all the hadronic activity is included in the two jets, improving the reconstruction of the P_T and η of the jets. The resolution in x_p^{jets} improves with x_p^{jets} because events with higher x_p^{jets} tend to have higher P_T jets whose P_T and η can be better reconstructed.

6.1.2 Purities

To measure the effect of migrations into a bin the purity, P, is used. This is estimated in the Monte Carlo sample as the fraction of events reconstructed in a bin that were also generated in that bin:

$$P = \frac{N_s}{N_r} \tag{6.2}$$

where N_s is the number of events that stay in the bin (are both generated and reconstructed there) and N_r is the number of events that were reconstructed in the bin.

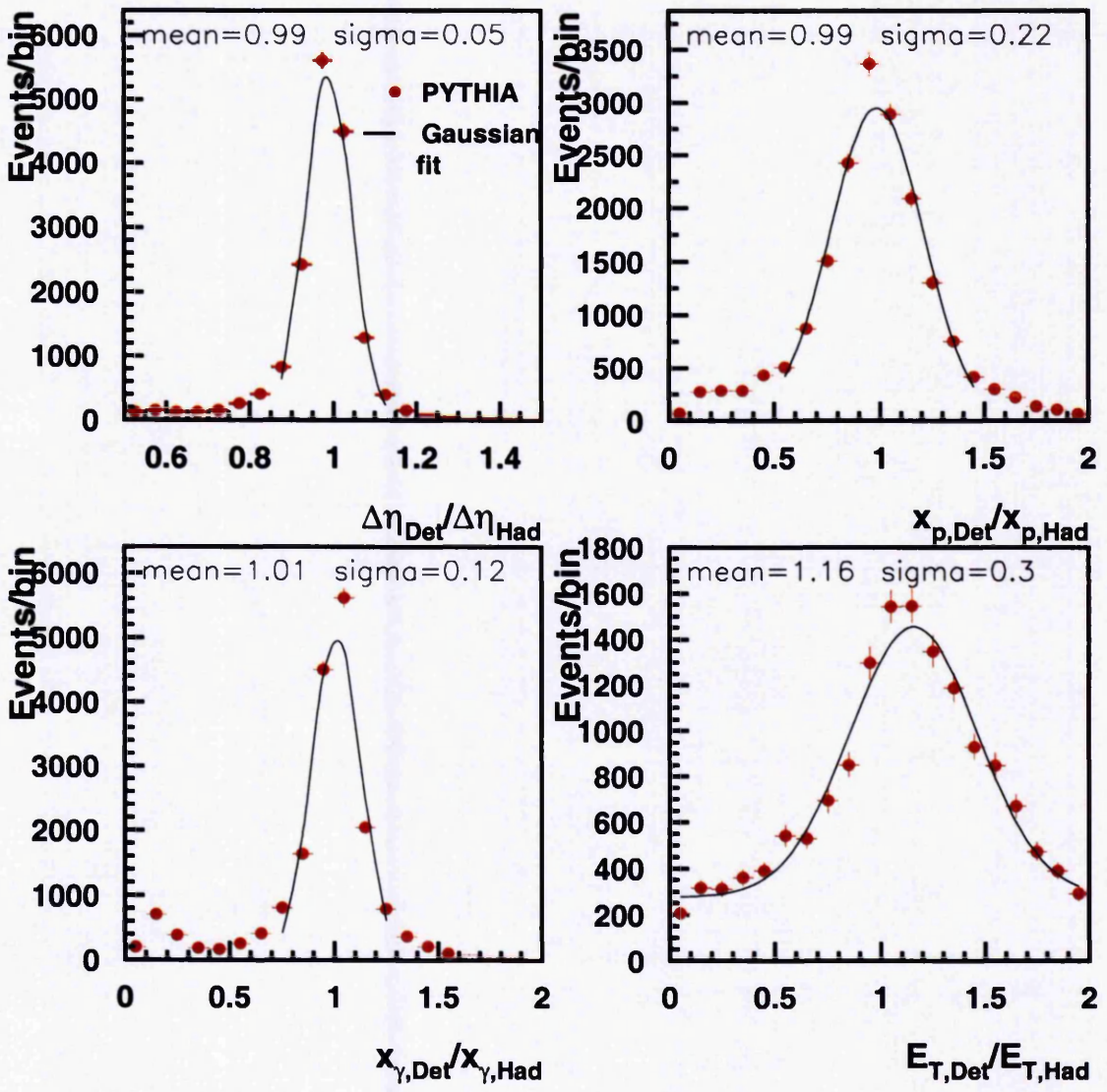

Figure 6.1: The resolution in $\Delta\eta$, x_p^{jets}, x_γ^{jets} and E_T^{gap}.

The impurities are dominated by migrations from events with jets below the P_T cut. The purity of the inclusive sample is 33%, but if P_T migrations are excluded the purity rises to 55%. In general, the purity in each bin was required to be greater than 20%.

The purities for each measured distribution are shown in figure 6.3. The purities in the gap event sample are higher than in the inclusive sample. The rapidity

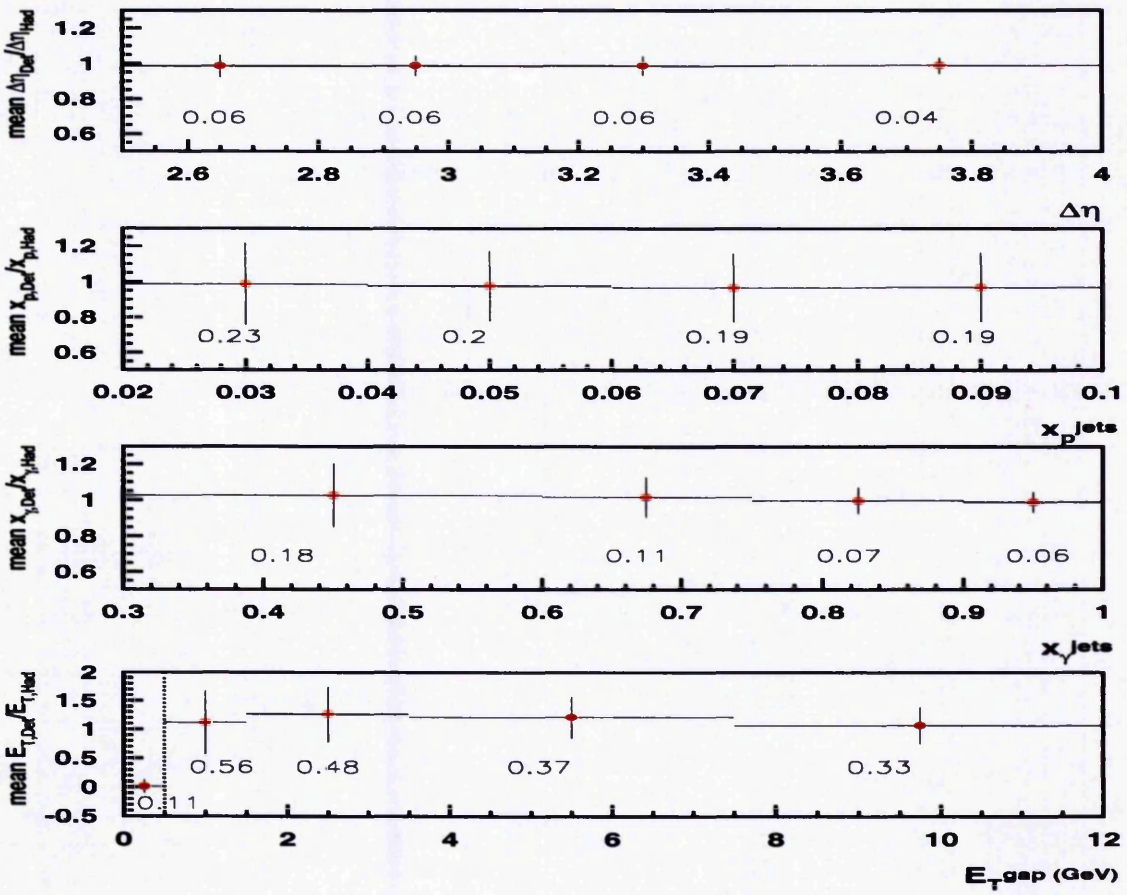

Figure 6.2: The binned mean values of the ratio of the reconstructed and generated values of $\Delta\eta$, x_p^{jets}, x_γ^{jets} and E_T^{gap}. The resolution is shown as an error bar and text. The first E_T^{gap} point shows $E_{T,rec}^{gap} - E_{T,had}^{gap}$.

gap means that there were no multiple interactions and so fewer jet P_T migrations occur; the jets are also better reconstructed, enabling the jet variables to be better measured. The purity rises as a function of x_γ^{jets} for similar reasons. The purity rises as a function of x_p^{jets} because events at higher x_p^{jets} have higher P_T jets. The purity falls as a function of $\Delta\eta$ because high $\Delta\eta$ forces the jets into those areas of the H1 detector in which jets can be less well measured, in particular into the SpaCal.

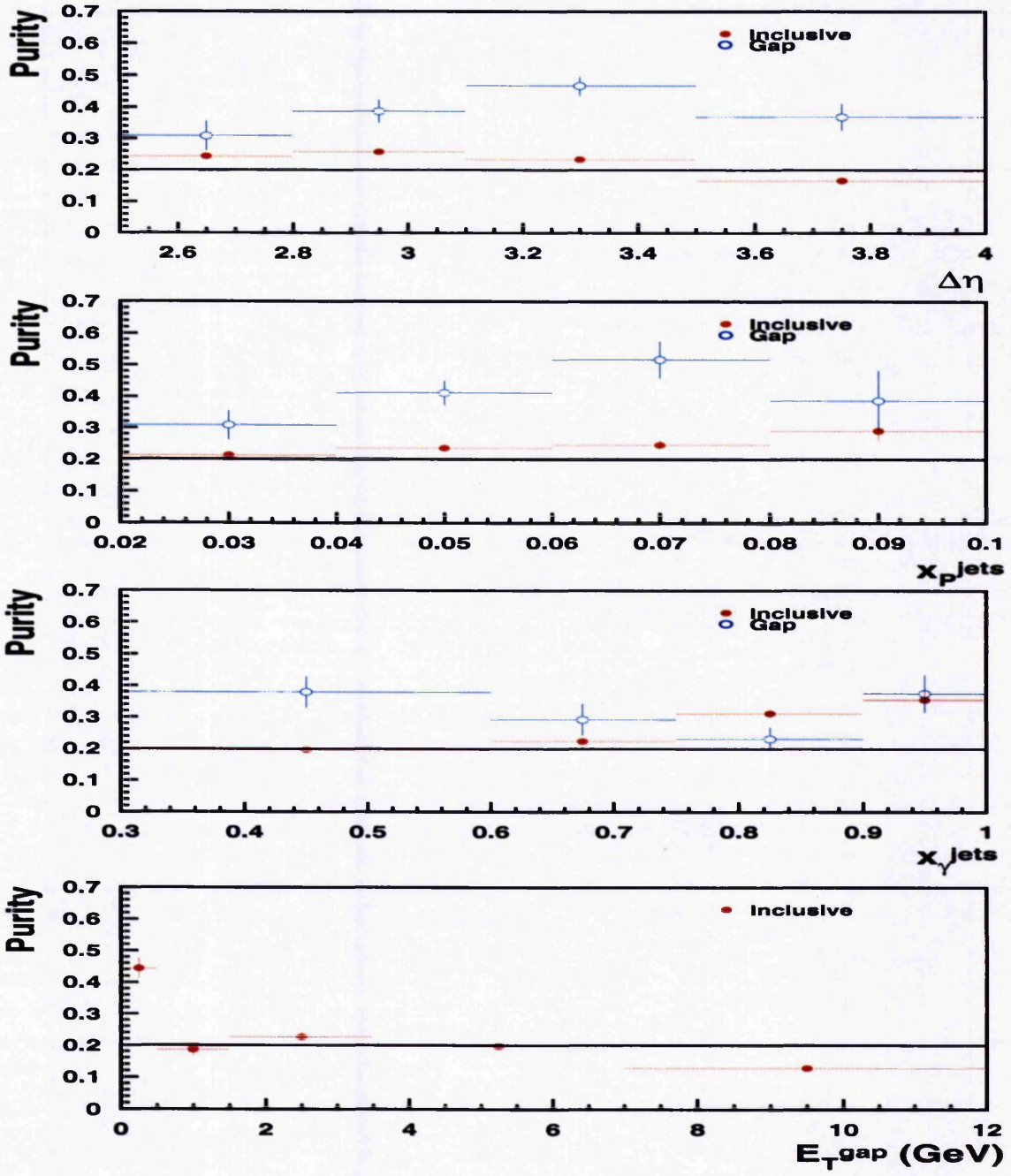

Figure 6.3: The purity in bins of $\Delta\eta$, x_p^{jets}, x_γ^{jets} and E_T^{gap} for the inclusive event sample and for events with E_T^{gap} <0.5 GeV. The horizontal line shows the desired minimum purity of 20%.

6.1.3 Stability

To describe how stable the distribution is with respect to migrations between the bins the stability, S, is defined:

$$S = \frac{N_s}{N_{g'}} \tag{6.3}$$

where $N_{g'}$ is the number of events generated in the bin that were reconstructed somewhere in the final event sample. The stability for each measured distribution is shown in figure 6.4. The stability is better than 60% except at low E_T^{gap} where the stability is better than 40%.

6.2 Correction for Trigger Efficiency

The triggers used in this analysis are not 100% efficient and reject some good *ep* events. The data can be corrected for this on a bin-by-bin basis as shown in equation 6.1. The trigger efficiency was measured using the data sample. The efficiency predicted by the simulation of the triggers was then compared to that measured. A good agreement was found and so the efficiencies measured with the Monte Carlo event sample were used to correct the data, since they have much higher statistics. The efficiency of the electron tagger element is excluded from this correction because it is already included in the tagger acceptance correction.

6.2.1 Measurement from the Data Sample

The efficiency of a given trigger s, ϵ_s, can be measured with the data sample using another independent trigger as a monitor trigger:

$$\epsilon_s = \frac{N_{m\&s}}{N_m} \tag{6.4}$$

where N_m is the number of events in the data sample that have been saved by the monitor trigger and $N_{m\&s}$ is the number of events that have been saved by both the

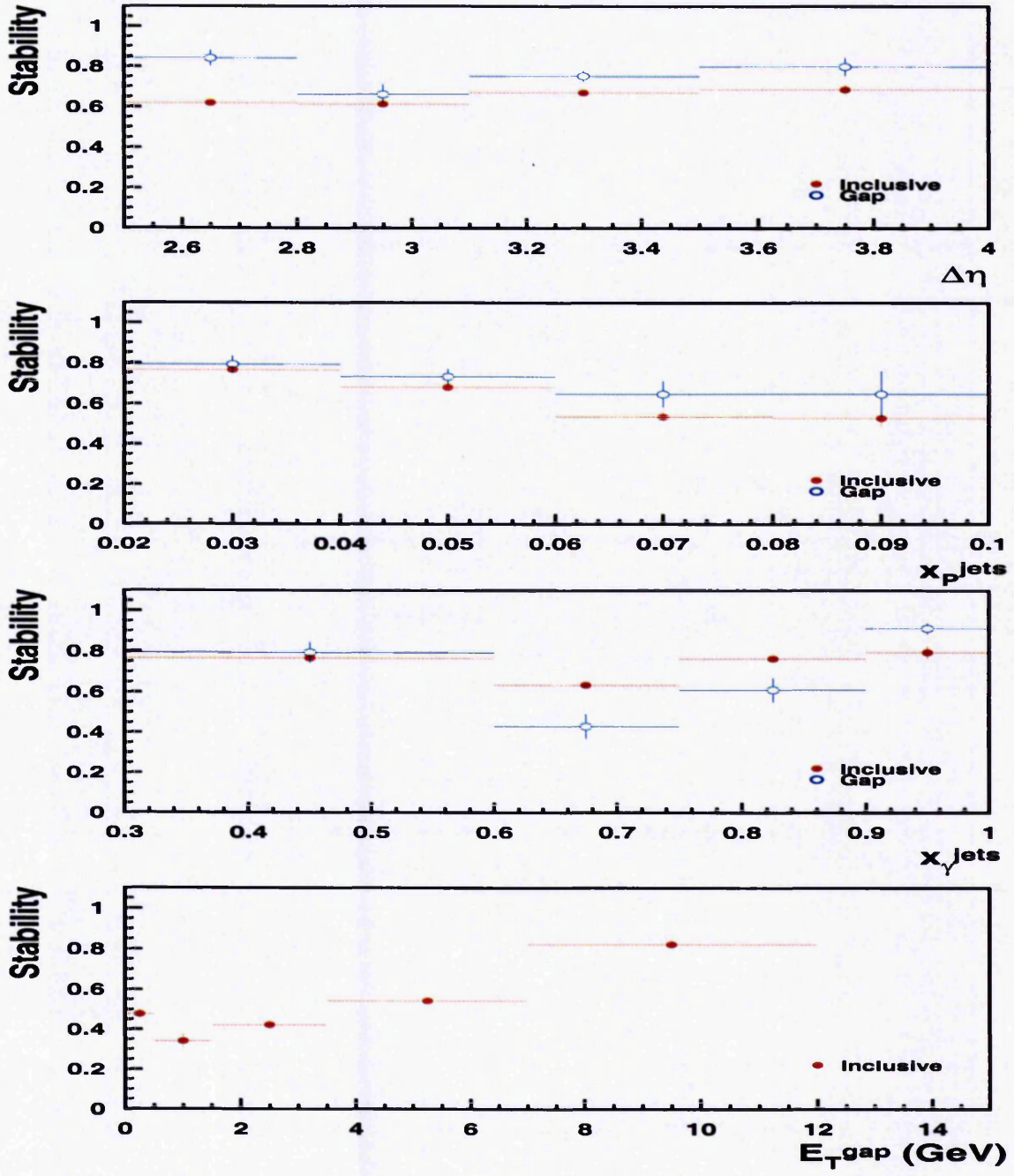

Figure 6.4: The stability in bins of $\Delta\eta$, x_p^{jets}, x_γ^{jets} and E_T^{gap} for the inclusive sample and for events with E_T^{gap} <0.5 GeV.

monitor trigger and trigger s. In order for this method to be valid the monitor trigger must have no conditions in common with trigger s and must save events in the same kinematic region. While s50 and s83 have no trigger elements in common (except for the electron tagger) they cover slightly different kinematic regions. Events which have fired s50 must have deposited at least 2 GeV of electromagnetic energy in the SpaCal. This results from jets which are more backward and hence less likely to have fired s83, which requires central tracks. If s50 were used as a monitor trigger for s83 this would underestimate the trigger efficiency by around 10%.

Fortunately, a further trigger, s82, can be used to monitor the efficiency of s83. The requirement of s82 is LAr_BR+DCRPh_TNeg+etag_all+zVtx_T0 compared to that of s83, zVtx_sig+DCRPh_Tc+eTAG+CIP_bwd_veto. s50 is defined as SPCLe_IET>1+eTAG+L2(SPCL_R20) , where the trigger elements are defined as

- LAR_BR: A tower above threshold, validated by a MWPC track.
- DCRPH_Tc(TNeg):At least 3 tracks (1 negative track) in the central tracker. The threshold momentum is around 200 MeV.
- zVtx_sig(T0): A significant peak (at least one entry) in the zVtx histogram.
- CIP_bwd_veto: ≤ 3 sectors hit in backward 1/4 of CIP.
- eTAG: At least 4 GeV in the 33 m electron tagger
- etag_all: A hit in the 33 m or 44 m electron tagger.
- SPCL_IET>1: At least 2 GeV in the SpaCal electromagnetic calorimeter.
- L2(SPCL_R20): L2 condition that removes the inner area ($R < 20$ cm) of the SpaCal.

To use s82 as a monitor trigger for s83, as in equation 6.4, the trigger elements that are in common must first be considered. The event selection demands an electron

in the 33m tagger and so etag_all will be fired by this tagger for all data events and hence the efficiency of the eTAG and etag_all elements will cancel. The efficiency of the zVtx_T0 element can be measured using s50 and is found to be 100%. This is in agreement with the Monte Carlo prediction. Any correlation between zVtx_T0 and s50 would lower the measured efficiency, but it is seen to be 100%. So this element can also be ignored when using s82 as a monitor efficiency. DCRPh_TNeg is a much weaker requirement of the DCRPh trigger than DCRPh_Tc. Almost all events that have fired DCRPh_Tc have also fired DCRPh_TNeg and so, to a very good approximation, the efficiency of DCRPh_TNeg+DCRPh_Tc is equal to that of DCRPh_Tc. Hence, the efficiency of s83 can be calculated in each bin from

$$\epsilon_{83} = \frac{N_{83\&82}}{N_{82}} \epsilon_{DCRPh\_TNeg} \tag{6.5}$$

The efficiency of the DCRPh_TNeg element, ϵ_{DCRPh_TNeg}, measured in the Monte Carlo sample is found to be around 95%. In addition, the efficiency of this element can be measured with the data sample using s50. A good agreement with the Monte Carlo is found, as shown in figure 6.5(a). This agreement suggests there is no correlation between DCRPh_TNeg and s50, which is not surprising since the DCRPh_TNeg requirement is sufficiently weak that even events with a very backward jet will pass.

To measure the efficiency of s50, ϵ_{50}, s83 can be used as a monitor trigger and then this result corrected for the correlation between the triggers since

$$\epsilon_{50} = \epsilon_{50}(83) \frac{\epsilon_{83}}{\epsilon_{83}(50)} \tag{6.6}$$

where $\epsilon_i(j)$ is the efficiency of trigger i measured using equation 6.4 with trigger j as the monitor trigger.

In order to give a higher efficiency across the detector both triggers can be used and, to a good approximation, the combined efficiency, ϵ, is given by

$$\epsilon = \epsilon_{83} + \epsilon_{50} - \epsilon_{83}\epsilon_{50} \tag{6.7}$$

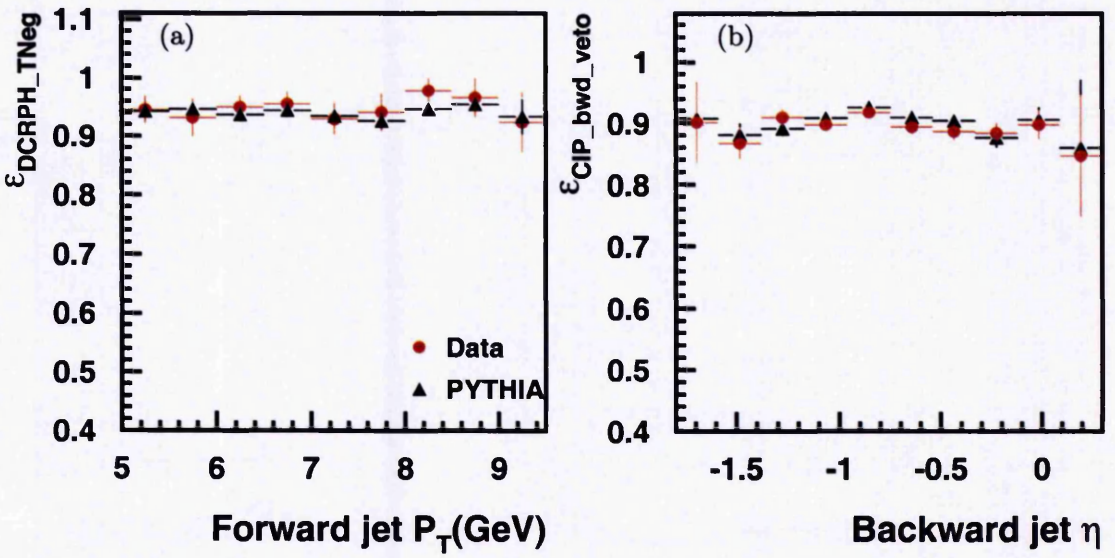

Figure 6.5: The efficiency of (a) the DCRPh_TNeg trigger element and (b) the CIP_bwd_veto as a function of P_T^f and η^b respectively measured using s50 with the data sample compared to that measured using the PYTHIA event sample.

There are sufficient statistics in the data sample to measure the trigger efficiency on a bin by bin basis for the inclusive distributions and in one bin for the gap event sample. However, bin by bin measurements for the gap measurements have large statistical errors or too few events to make any measurement.

6.2.2 Measurement from the Monte Carlo Sample

Unlike the data sample, in the Monte Carlo event sample the total number of events before the trigger requirement, N, is known. Hence, the efficiency of a trigger s can be calculated directly from

$$\epsilon_s = \frac{N_s}{N} \tag{6.8}$$

where N_s is the number of events in the sample that also pass subtrigger s.

Similarly, the efficiency of each trigger element can be measured and compared

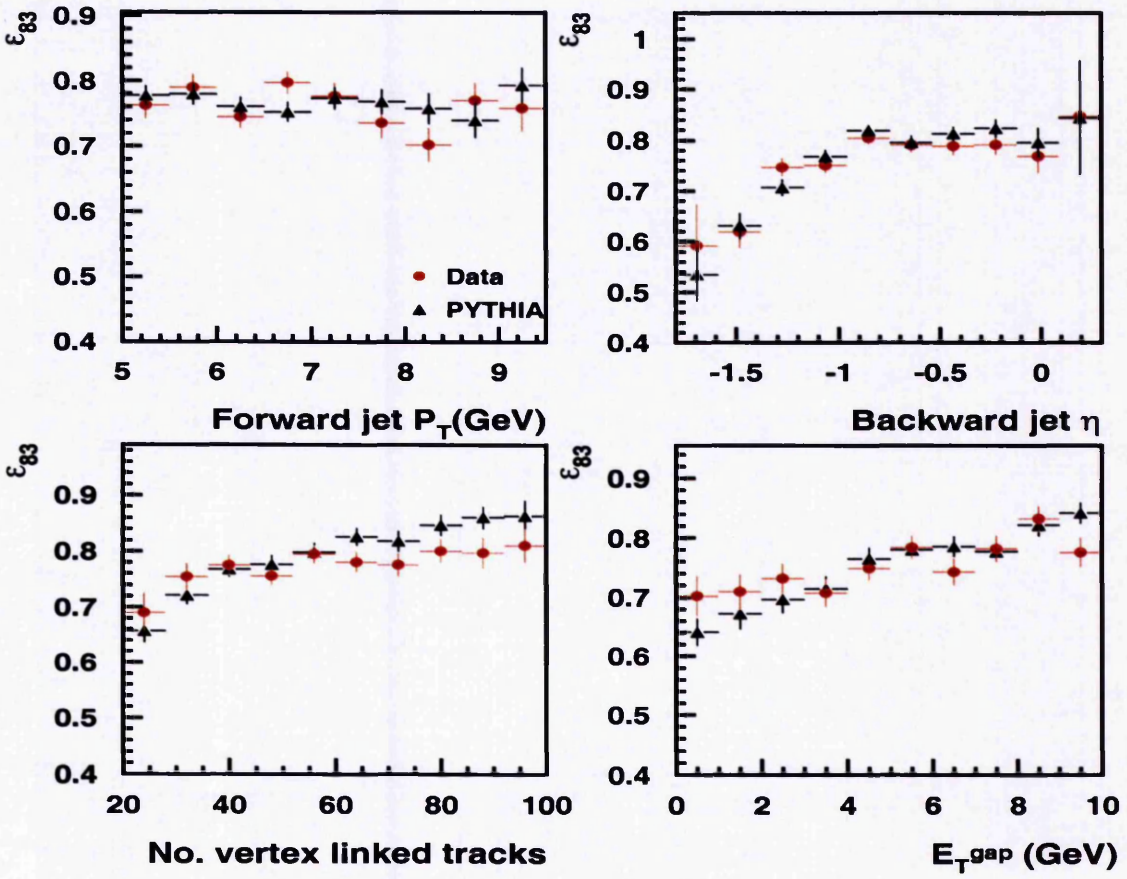

Figure 6.6: The efficiency of s83, as a function of P_T^f, η^b, the number of vertex linked tracks and E_T^{gap}, measured using the data sample and compared to that measured using the PYTHIA event sample.

to that measured in the data. For s83 an extremely good agreement is found for the zVtx_sig and DCRPh_Tc trigger elements. The CIP_bwd_veto agreed well in the shape of all distributions but was consistently too high by 2%. This factor was included in the simulation and a good agreement was then seen, as shown in figure 6.5(b). So the efficiency of s83, measured in the data, can be well described by the Monte Carlo event samples. Example distributions showing this agreement in P_T^f, η^b, the number of vertex linked tracks and E_T^{gap} are shown in figure 6.6.

S50 is well described by the Monte Carlo simulation where there is significant energy in the SpaCal but there is some disagreement at lower energies, which are in the tail of the distribution close to the threshold energy of the trigger. The energy dependence of the trigger element is measured in the data and included in the simulation. The efficiency of the level 2 condition of s50 is not simulated in the Monte Carlo. This was measured in the data and found to be a constant, 95%. After including these factors in the simulation a good agreement between the efficiency measured using the data and Monte Carlo event samples was obtained. This is shown for the variables P_T^b, η^f, EM energy in the SpaCal and E_T^{gap}, in figure 6.7.

6.2.3 Correction Factors

The trigger efficiencies which are used to correct the data are shown in figures 6.8 and 6.9. The measurements using the data are shown and agree, where there is sufficient data, with those values used in the analysis.

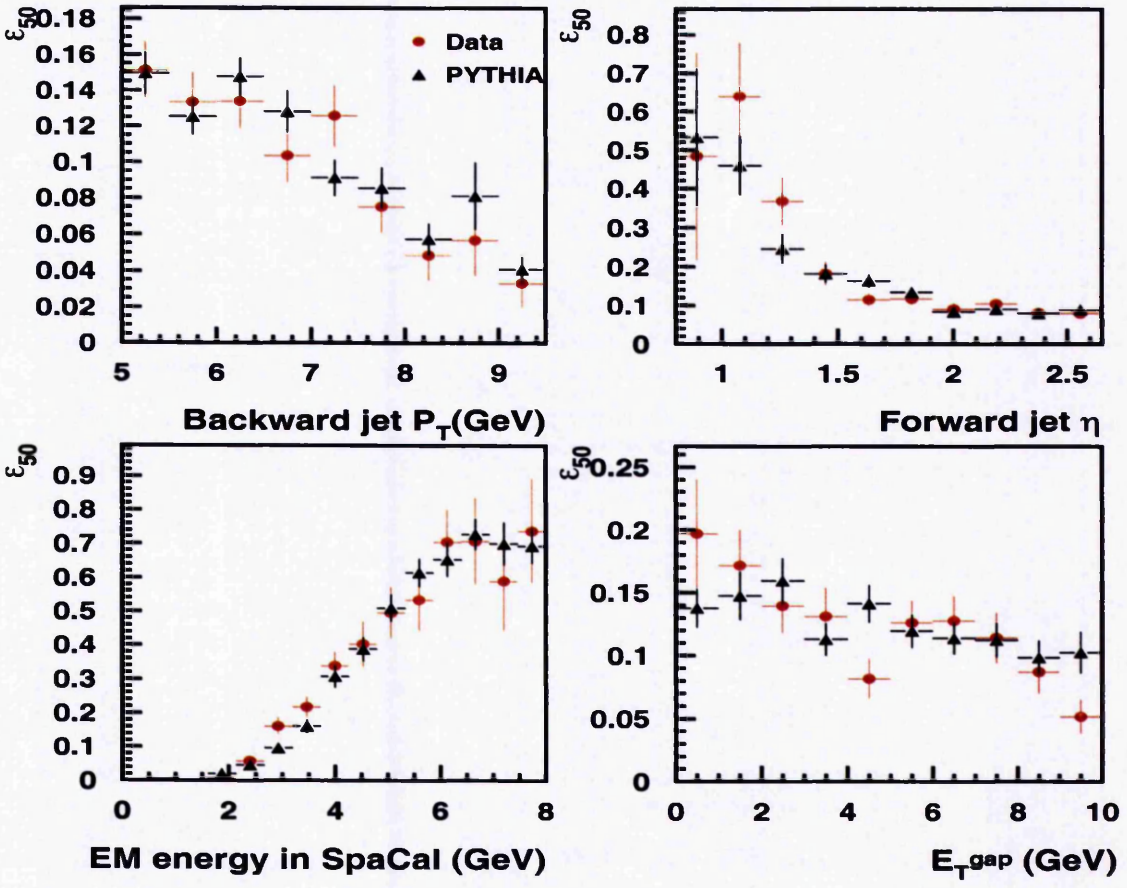

Figure 6.7: The efficiency of s50, as a function of P_T^b, η^f, EM energy in the SpaCal and E_T^{gap}, measured using the data sample and compared to that measured using the PYTHIA event sample.

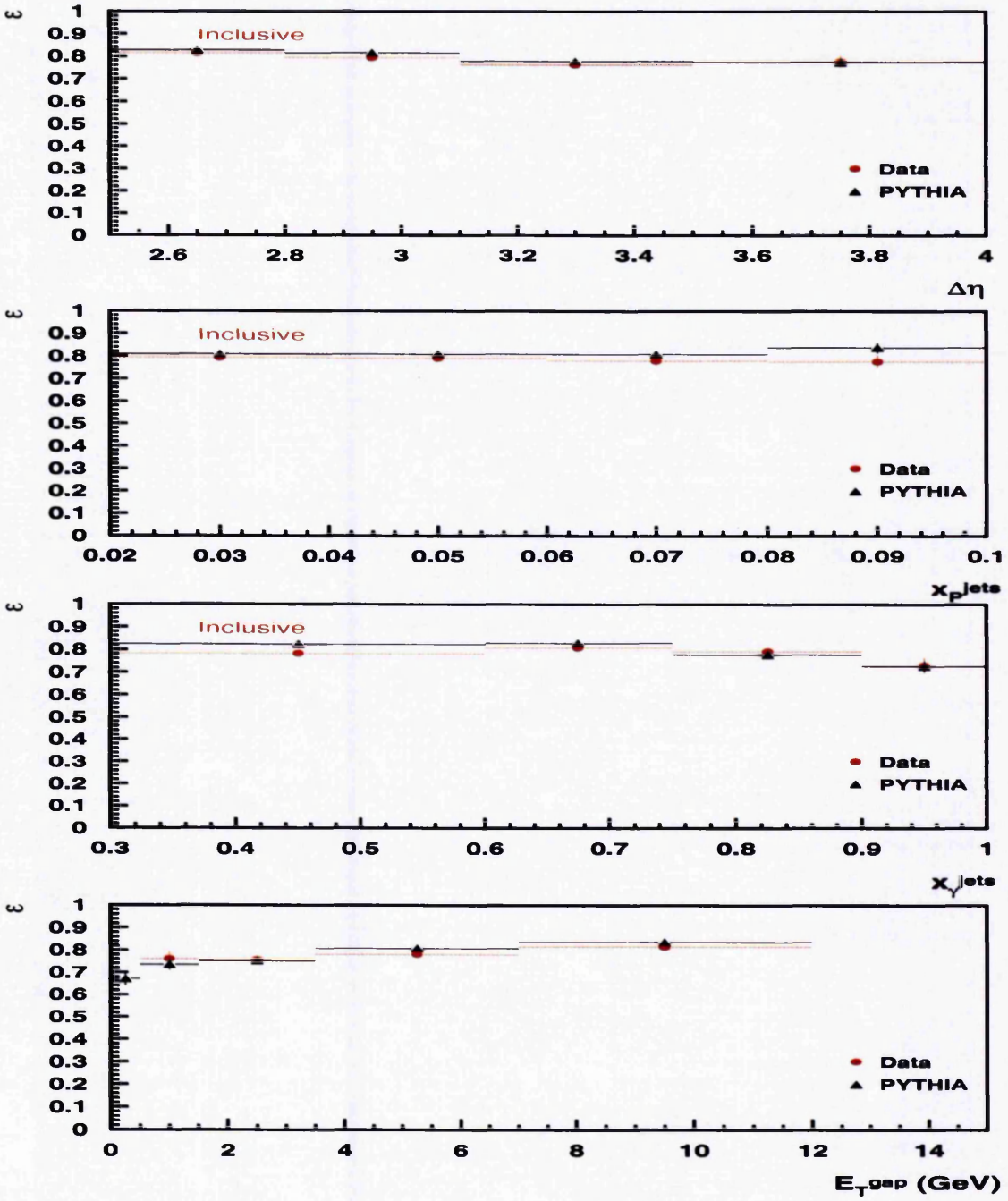

Figure 6.8: The combined trigger efficiency in bins of $\Delta\eta$, x_p^{jets}, x_γ^{jets} and E_T^{gap} for the inclusive sample measured using the PYTHIA and data event samples.

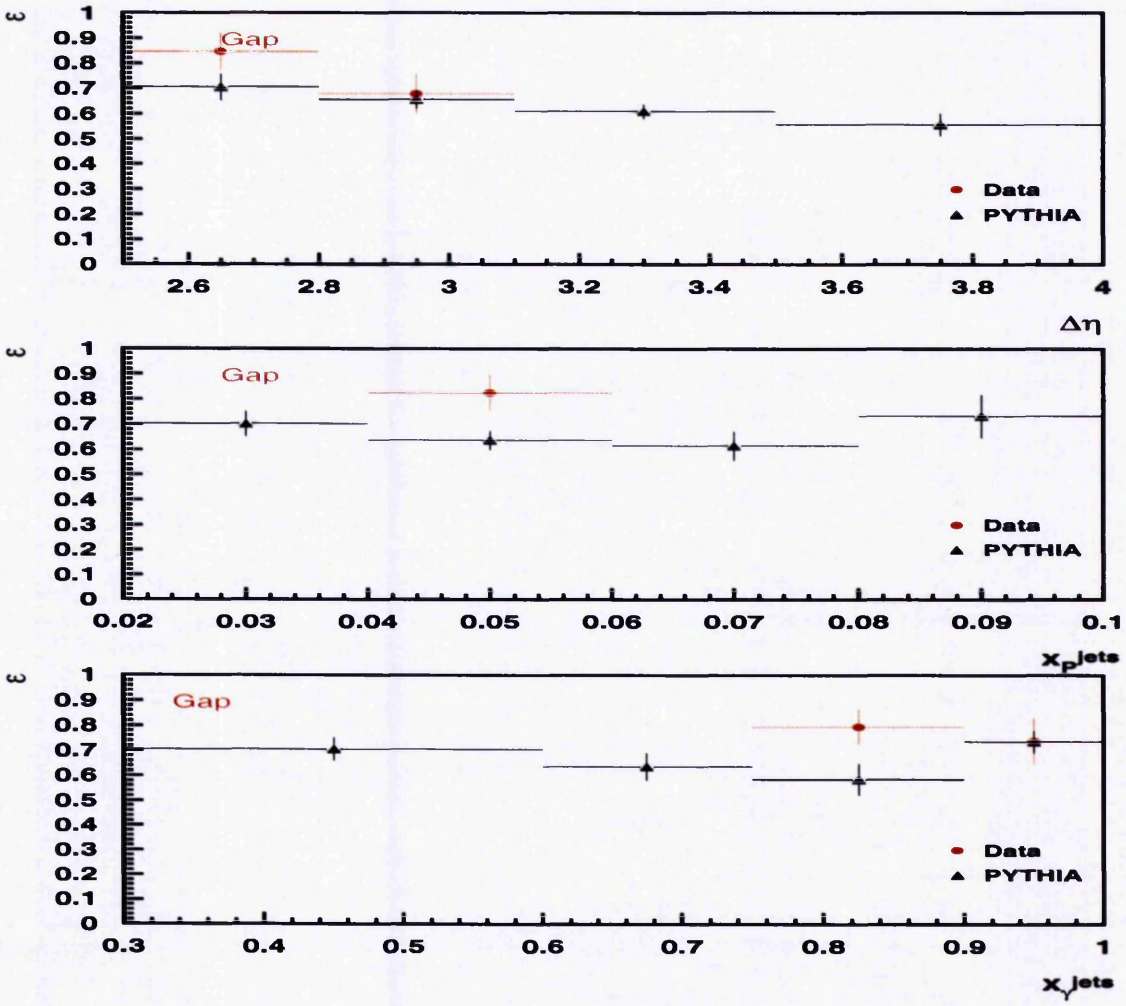

Figure 6.9: The combined trigger efficiency in bins of $\Delta\eta$, x_p^{jets} and x_γ^{jets} for events with $E_T^{gap} < 0.5$ GeV measured using the PYTHIA and data event samples.

6.3 Correction for Detector Effects

6.3.1 Correction for Electron Tagger Acceptance

The acceptance of the electron tagger, shown in figure 5.2, is not 100% and the data must be corrected for this. Unlike other detector inefficiencies, this cannot be well modelled by the H1 simulation, because it is dependent on the HERA beam optics,

which vary for each run. The acceptance has been measured and parameterised for each run and a luminosity weighted acceptance, as a function of y, calculated for the period during which the data used were taken. This weighting was applied to the Monte Carlo events which had been simulated for detector effects.

6.3.2 Measurement of the Detector Acceptance

The detector acceptance, A, for a given bin can be calculated from the number of Monte Carlo events generated in the bin, N_g, and the number of events reconstructed in the bin, N_r:

$$A = \frac{N_r}{N_g}. \tag{6.9}$$

The statistical error on the acceptance, σ_A, is included in the final error analysis and is calculated from

$$\sigma_A = A\left(\frac{V_r}{N_r^2} + \frac{V_g}{N_g^2} - \frac{2}{N_r \cdot N_g}\sum_s (T_s \cdot W_s)(W_s)\right)^{\frac{1}{2}} \tag{6.10}$$

where the sum over s is the sum over all events that are both generated and reconstructed in the bin, W is the weight of an event at the generator level, T is the additional weighting at the detector level and

$$V_r = \sum_r T_r^2 \cdot W_r^2 \tag{6.11}$$

$$V_g = \sum_g W_g^2 \tag{6.12}$$

where the sum over r (g) is the sum over the events reconstructed (generated) in the bin.

Figure 6.10 and figure 6.11 show the acceptance as a function of $\Delta\eta$, x_p^{jets}, x_γ^{jets} and E_T^{gap} for the inclusive event sample and for gap events with $E_T^{gap} < 0.5\,\text{GeV}$ respectively. The predictions from both HERWIG and PYTHIA are shown and these are in good agreement, typically within 5%. The acceptance is above 40% for all bins. The acceptance is much higher for non-gap events than for gap events

because of the larger number of P_T migrations into the bin, discussed in section 6.1.2. The data is corrected using the acceptance determined from PYTHIA since PYTHIA describes the data better than HERWIG.

6.4 Error Analysis

The errors are estimated on a bin by bin basis. The error on each data point comprises of three parts: statistical error, uncorrelated systematic error and correlated systematic error. The statistical errors are assumed to follow a Poisson distribution. The uncorrelated and correlated systematic errors have been separated because the shape of the distribution can only be varied within the limits of the combined statistical and uncorrelated systematic errors, while the normalisation is free within the total error. A number of systematic errors are considered and are discussed below. The fractional error from each source is shown for each data bin in figure 6.12 for the inclusive cross section measurements, in figure 6.13 for the gap cross section measurements and in figure 6.14 for the ratio of these, the gap fraction measurements.

6.4.1 Monte Carlo Statistics

The determination of the detector acceptance and the trigger efficiency has a statistical error associated with it. This was calculated using equation 6.10 but replacing the number of reconstructed events with the number of those that additionally pass the trigger requirement.

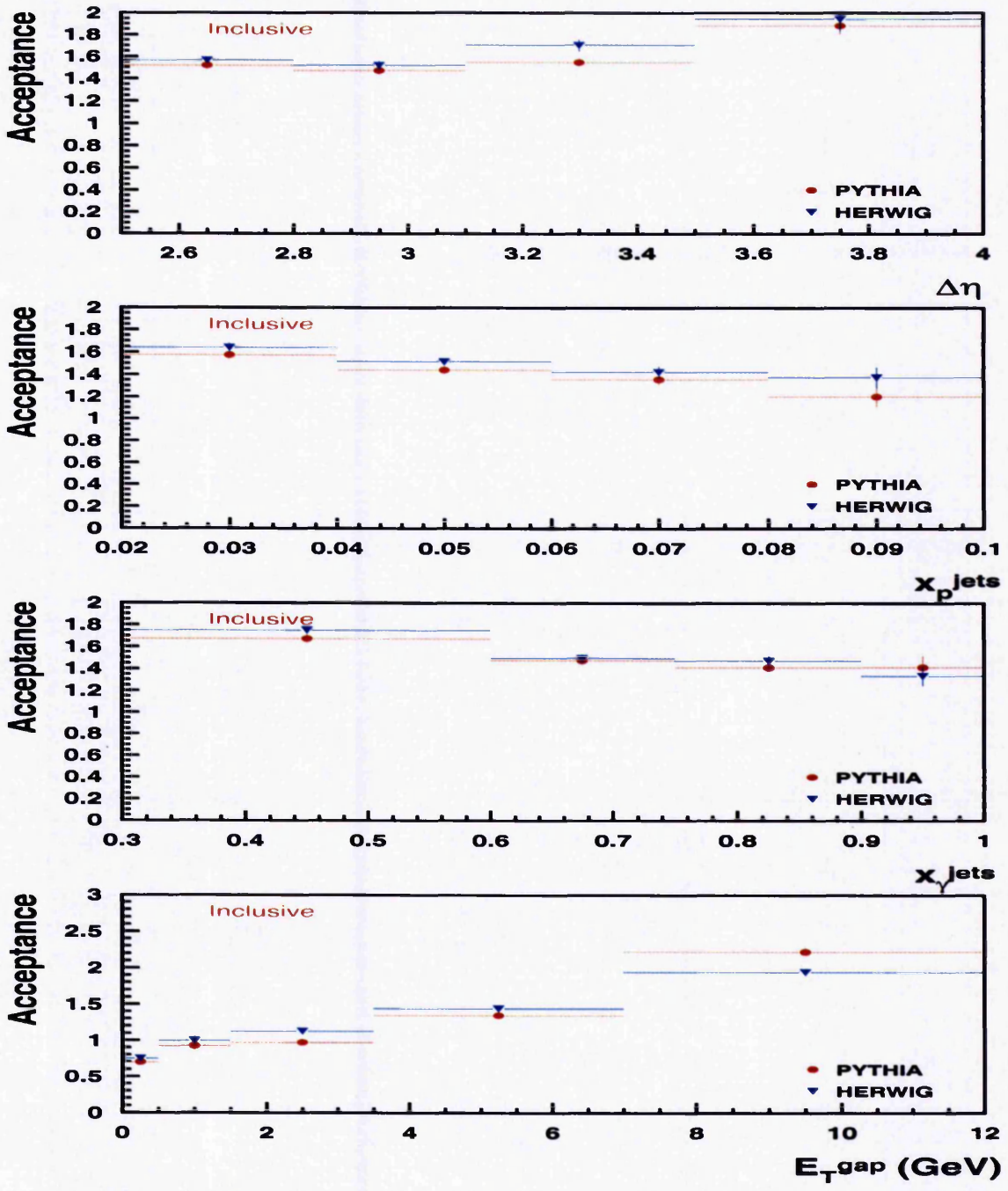

Figure 6.10: The acceptance in bins of $\Delta\eta$, x_p^{jets}, x_γ^{jets} and E_T^{gap} for the inclusive sample measured using PYTHIA and HERWIG.

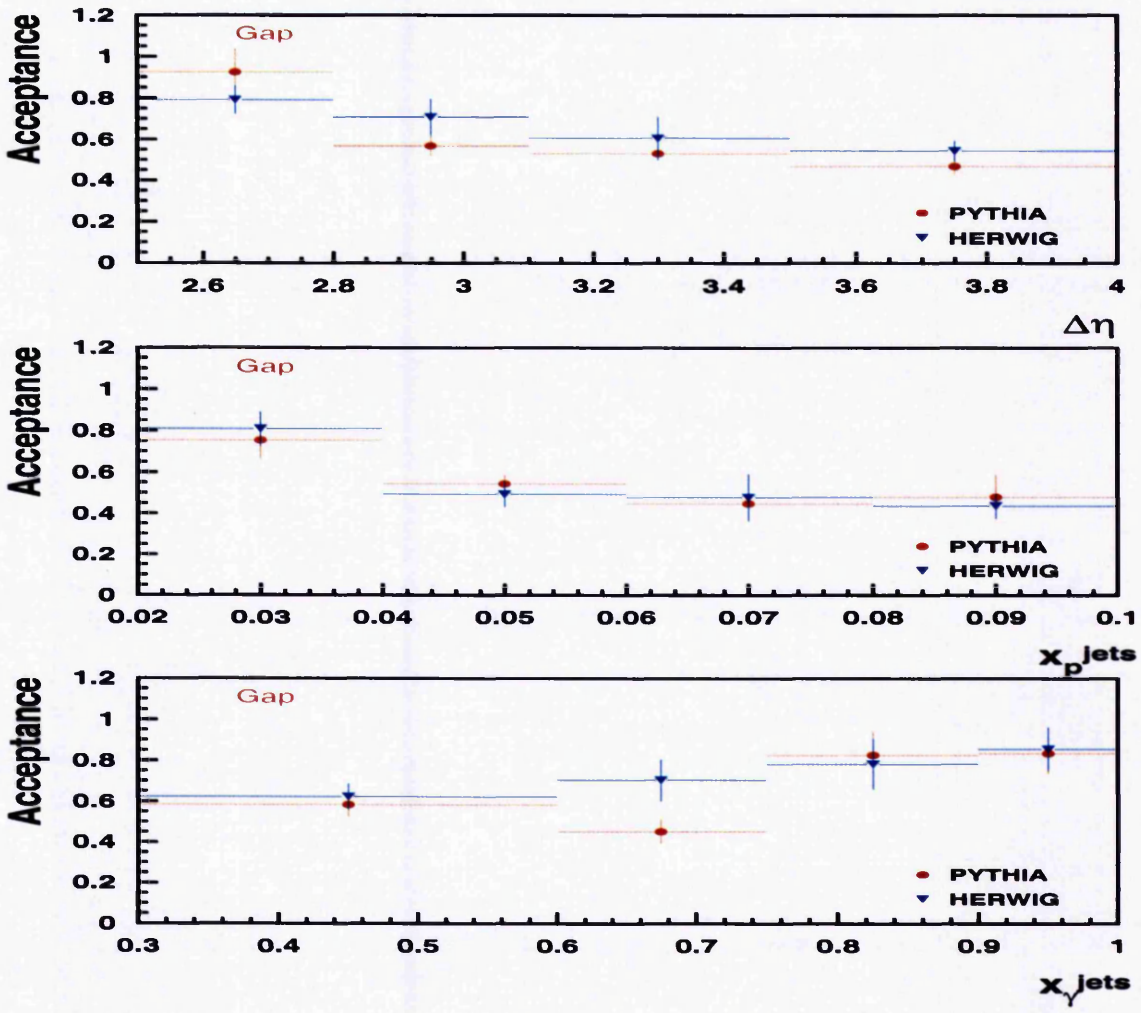

Figure 6.11: The acceptance in bins of $\Delta\eta$, x_p^{jets} and x_γ^{jets} for events with $E_T^{gap} < 0.5$ GeV measured using PYTHIA and HERWIG.

6.4.2 Determination of the Acceptance

The Monte Carlo models do not provide a perfect description of the distributions seen in the data and hence only provide estimates of the acceptance correction. Two different models, HERWIG and PYTHIA, were used to estimate the acceptance. The whole difference between the acceptance measured using the two Monte Carlos was used as the systematic error and this is typically 5%.

Both HERWIG and PYTHIA have been reweighted to improve the y and x_γ^{jets} distributions. The effect of this reweighting on the acceptance correction was considered. The error was taken as the difference between the acceptance determined with and without reweighting the distributions and on average is 3%.

The effect on the acceptance correction of including a colour singlet model in the Monte Carlo sample was also considered. For the inclusive distributions the change to the acceptance correction was extremely small. For the gap distributions the two measurements were in agreement, but the statistics excluding the colour singlet model were extremely low.

6.4.3 Trigger Efficiency Correction

To take into account the possible uncertainties in the shape and normalisation of the trigger efficiency an uncorrelated error of 5% and a correlated error of 5% were ascribed to the correction for trigger efficiency.

6.4.4 Energy Scale Uncertainties

The energy scales of the detectors are known within a certain precision. For the detectors used in this measurement these uncertainties are:

- Hadronic energy scale of the LAr calorimeter: $\pm 4\%$ [8]
- Hadronic energy scale of the SpaCal: $\pm 7\%$ [28]
- Momentum scale of tracks: $\pm 3\%$ [28]

The errors resulting from these uncertainties were estimated using the Monte Carlo event sample, because of the higher statistics. For each energy scale the analysis was rerun twice, with the energy scale scaled up and then down by the known uncertainty.

The error was taken to be half the difference between these two measurements. The dominant error on the measured cross sections is from the uncertainty on the LAr calorimeter energy scale ($\sim$ 15%). The effect is lower for gap events and partially cancels on the gap fraction measurements. The uncertainties from the SpaCal and track energy scales are much smaller, typically 1.5% and 3.5% respectively. These errors are correlated between the data points.

6.4.5 Luminosity Measurement

The uncertainty on the measurement of the luminosity is 2% [21]. This effects each measurement the same and so is a correlated error; the error cancels exactly on the gap fraction measurements.

6.4.6 Electron Tagger Acceptance

The uncertainty on the measurement of the electron tagger acceptance is 5%. This is also a correlated error, cancelling exactly on the gap fraction measurements.

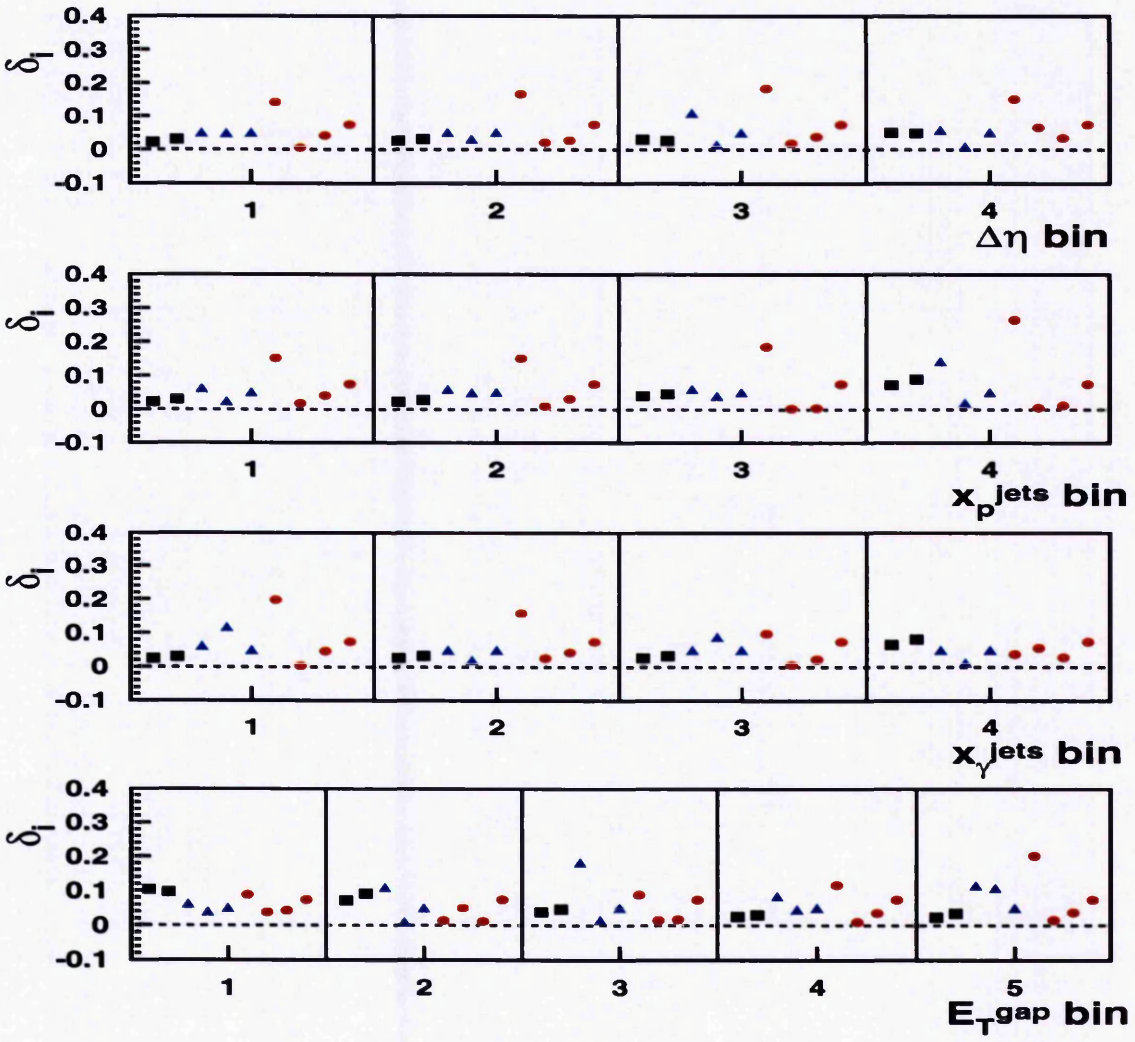

Figure 6.12: The fractional error on the inclusive cross section measurements, within each bin left to right: from data statistics, Monte Carlo statistics, Monte Carlo model, Monte Carlo reweighting, uncorrelated trigger efficiency, LAr calorimeter energy scale, SpaCal energy scale, track momentum scale and the combined error from correlated trigger efficiency, luminosity measurement and electron tagger acceptance.

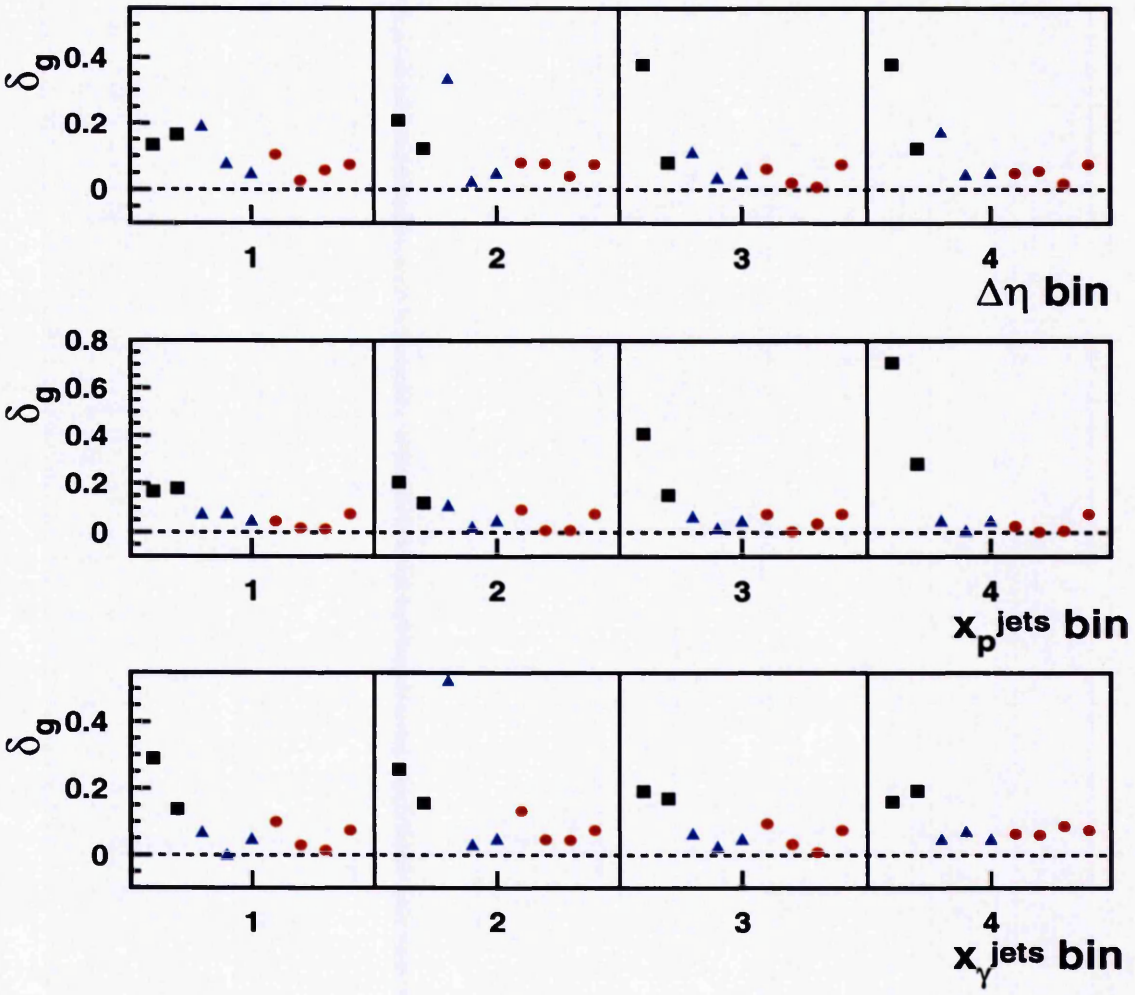

Figure 6.13: The fractional error on the gap cross section measurements, within each bin left to right: from data statistics, Monte Carlo statistics, Monte Carlo model, Monte Carlo reweighting, uncorrelated trigger efficiency, LAr calorimeter energy scale, SpaCal energy scale, track momentum scale and the combined error from correlated trigger efficiency, luminosity measurement and electron tagger acceptance.

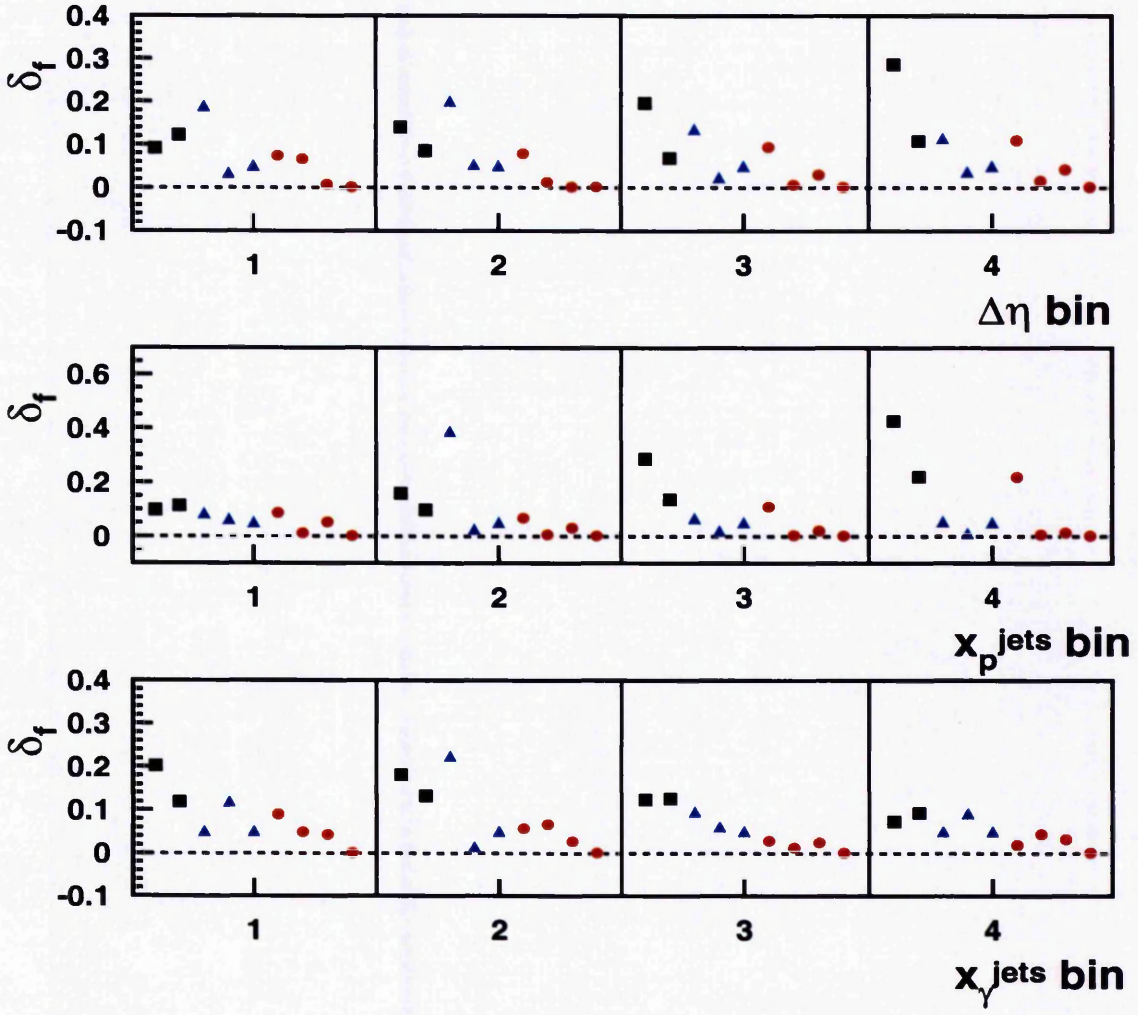

Figure 6.14: The fractional error on the gap fraction measurements, within each bin left to right: from data statistics, Monte Carlo statistics, Monte Carlo model, Monte Carlo reweighting, uncorrelated trigger efficiency, LAr calorimeter energy scale, SpaCal energy scale, track momentum scale and the combined error from correlated trigger efficiency, luminosity measurement and electron tagger acceptance.

Chapter 7

Experimental Results

The cross sections and gap fraction measurements resulting from the analysis are discussed in this chapter. The kinematic range of these measurements is stated in section 5.3. Rapidity gaps are defined using four values of E_T^{cut}. This may give the opportunity for comparison to theoretical calculations for which E_T^{gap} must be sufficiently large, as well as with calculations as a function of E_T^{cut}. Tables of all data are given in appendix B. The measurements are compared to the predictions of the HERWIG and PYTHIA Monte Carlos. These give the results expected from standard γp processes. Differences between the two models mainly result from the different hadronisation schemes used, cluster fragmentation in HERWIG and string fragmentation in PYTHIA.

The HERWIG and PYTHIA predictions are both made by generating the resolved and direct processes separately and then adding these together according to their generated cross sections. To generate the predictions with the addition of colour singlet exchange, BFKL exchange is added to the HERWIG sample and photon exchange, scaled by 1200, is added to the PYTHIA sample. The overall normalisation of the PYTHIA sample was scaled by a factor of 0.7 in order to fit the measured inclusive dijet photoproduction cross sections. Similarly, the HERWIG sample was

scaled by a factor of 1.2.

While the photon exchange model is not a viable candidate process, the cross section being three orders of magnitude too small, it serves as a contrast to the HERWIG BFKL model. This enables the sensitivity of the data to the underlying dynamics to be tested. An exchanged photon couples to quarks, whilst in the BFKL model the exchange couples predominantly to gluons.

7.1 The E_T^{gap} Cross Section

The *ep* cross section, differential in E_T^{gap}, fully corrected for detector effects, is shown in figure 7.1. This is compared to the predictions from the standard HERWIG and PYTHIA models. There is a marked excess in the data for $E_T^{gap} < 0.5$ GeV over both HERWIG and PYTHIA. The shape of the predicted distribution differs markedly between the two models. In particular, HERWIG predicts a larger cross section for $E_T^{gap} < 0.5\,\text{GeV}$. However, neither generator can describe the shape of the E_T^{gap} distribution well.

In figure 7.2 the data is compared to models with colour singlet exchange: HERWIG + BFKL and PYTHIA + γ exchange. In each case, the addition of the colour singlet events is able to describe the low E_T^{gap} cross section while, as expected, leaving the rest of the distribution unchanged. Although the need for the inclusion of colour singlet events is clearly seen, there is little sensitivity to the underlying dynamics of the exchange. This motivates differential measurements of events with low E_T^{gap}.

7.2 The $\Delta\eta$ Cross Section

The *ep* cross section, differential in $\Delta\eta$, for the inclusive dijet sample is shown in figure 7.3. The predictions from PYTHIA and HERWIG are also shown. PYTHIA

gives a very good description of the data, while that of HERWIG falls more steeply with $\Delta\eta$ than the data. Typically, dijet cross section measurements are made at very small values of $\Delta\eta$ so this measurement provides complementary information to existing dijet measurements.

Figure 7.4 shows the cross section with the additional requirement that $E_T^{gap} <$ 1.0 GeV, compared to the predictions from PYTHIA and HERWIG. For $\Delta\eta >\sim 3$ there is an excess over both models.

7.3 The x_p^{jets} Cross Section

The ep cross section, differential in x_p^{jets}, for the inclusive dijet sample is shown in figure 7.5. The predictions from HERWIG and PYTHIA are also shown. A good description of the data is given by both HERWIG and PYTHIA. Only a small range of x_p^{jets} is kinematically available. The requirement that $\Delta\eta > 2.5$, i.e. that the parton-parton centre of mass energy must be large, sets the minimum available x_p^{jets}.

Figure 7.6 shows the cross section with the additional requirement that $E_T^{gap} <$ 1.0 GeV, compared to the predictions from PYTHIA and HERWIG. While the cross section prediction from HERWIG is greater than that from PYTHIA, the data lie above both predictions, again showing the need for an additional colour singlet exchange.

7.4 The x_γ^{jets} Cross Section

The ep cross section, differential in x_γ^{jets}, for the inclusive dijet sample is shown in figure 7.7. The predictions from HERWIG and PYTHIA are also shown. Neither model is able to describe the shape of the distribution. This is the first time that

the x_γ^{jets} distribution has been measured for events at large $\Delta\eta$ and this information can now be used to improve future Monte Carlo modelling of the data.

Figure 7.8 shows the cross section with the additional requirement that $E_T^{gap} <$ 1.0 GeV, compared to the predictions from PYTHIA and HERWIG. Again, the data tend to lie systematically above the predictions from both HERWIG and PYTHIA, although HERWIG lies much nearer to the data.

7.5 The $\Delta\eta$ Gap Fraction

Figure 7.9 shows the gap fraction, as defined in equation 4.23, measured as a function of $\Delta\eta$ compared to the predictions from HERWIG and PYTHIA. The gap fraction in the absence of colour singlet events is naively expected to fall exponentially with increasing $\Delta\eta$. This is indeed seen in the PYTHIA prediction. HERWIG has a tendency to produce gaps at a higher rate at large $\Delta\eta$. However, an excess is seen at large $\Delta\eta$ over both models. The data are clearly flat, or possibly rising at the largest $\Delta\eta$. This behaviour is typical of a diffractive exchange.

The gap fraction defined by $E_T^{gap} < 1.0$ GeV is shown in comparison to the colour singlet models in figure 7.10. A good description of the data is obtained, but no model is particularly favoured.

7.6 The x_p^{jets} Gap Fraction

Figure 7.11 shows the gap fraction measured as a function of x_p^{jets} and the predictions from HERWIG and PYTHIA. There is an excess over the PYTHIA prediction in all bins and this persists up to the largest E_T^{cut}. The excess over HERWIG is less pronounced. At low x_p^{jets}, there is a correlation between x_p^{jets} and x_γ^{jets} because in order to have a large $\Delta\eta$ and a small x_p^{jets} then x_γ^{jets} must be large. This leads to

the tendency seen in both the data and the Monte Carlo of a rise at low x_p^{jets}.

The gap fraction defined by $E_T^{gap} < 1.0$ GeV is shown in comparison to the colour singlet models in figure 7.12. Differences between the BFKL exchange and the photon exchange models may be due to the underlying dynamics of the models; the BFKL pomeron couples preferentially to gluons whilst the photon couples only to quarks. At high x_p^{jets}, the fraction of quark initiated collisions is higher and this would lead to an increased gap fraction in the photon exchange model. However, the statistics are too low to enable the data to differentiate between the models in this way.

7.7 The x_γ^{jets} Gap Fraction

Figure 7.13 shows the gap fraction measured as a function of x_γ^{jets} and the predictions from HERWIG and PYTHIA. There is an excess in the data for $E_T^{gap} < 0.5$ GeV and $x_\gamma^{jets} < 0.75$ over both Monte Carlo predictions, although the gap fraction in HERWIG is higher than that predicted by PYTHIA. The gap fraction rises sharply at high x_γ^{jets}. This is seen in both HERWIG and PYTHIA and is due to the fact that, in leading order QCD, direct photoproduction events have quark propagators, while resolved events are dominated by gluon propagators. Quark propagators have a much lower probability to radiate into the gap between the jets than gluon propagators, leading to a higher gap fraction.

The gap fraction defined by $E_T^{gap} < 1.0$ GeV is shown in comparison to the colour singlet models in figure 7.14. A better description of the gap fraction for $x_\gamma^{jets} < 0.75$ is achieved for both models, but at the expense of too high a gap fraction at large x_γ^{jets}.

7.8 Discussion

There is a clear excess of events in the data with low E_T^{gap} over that predicted by the PYTHIA and HERWIG Monte Carlo event generators. The addition of a hard colour singlet exchange component to the predictions has been investigated. This solution gives an improved description of the data. Unfortunately, different models of the underlying dynamics of the exchange cannot be distinguished.

The fact that the BFKL pomeron, with the choice of $\alpha_s = 0.18$, describes the magnitude of the cross section for gap events is very interesting. A similar value was also found to fit the Tevatron data on gaps between jets. However, there are a number of uncertainties. In order to know how much of the measured gap cross section to assign to colour singlet exchange, the cross section for gap events in standard photoproduction processes must be known. The large uncertainty here is evident from the differences between the predictions of PYTHIA and HERWIG. The addition of multiple interactions to the BFKL Monte Carlo events was not considered; the gap survival probabilty for these events will also affect the normalisation of the BFKL cross section needed. Finally, there are also uncertainties on the BFKL predictions shown here; the correct way to treat the running coupling is unknown, as are the higher order corrections at non-zero t.

The new definition of a rapidity gap used here may enable the data to be compared to pQCD predictions, such as the work of Oderda and Sterman. This may help to improve our understanding of colour singlet exchange and multiple interactions.

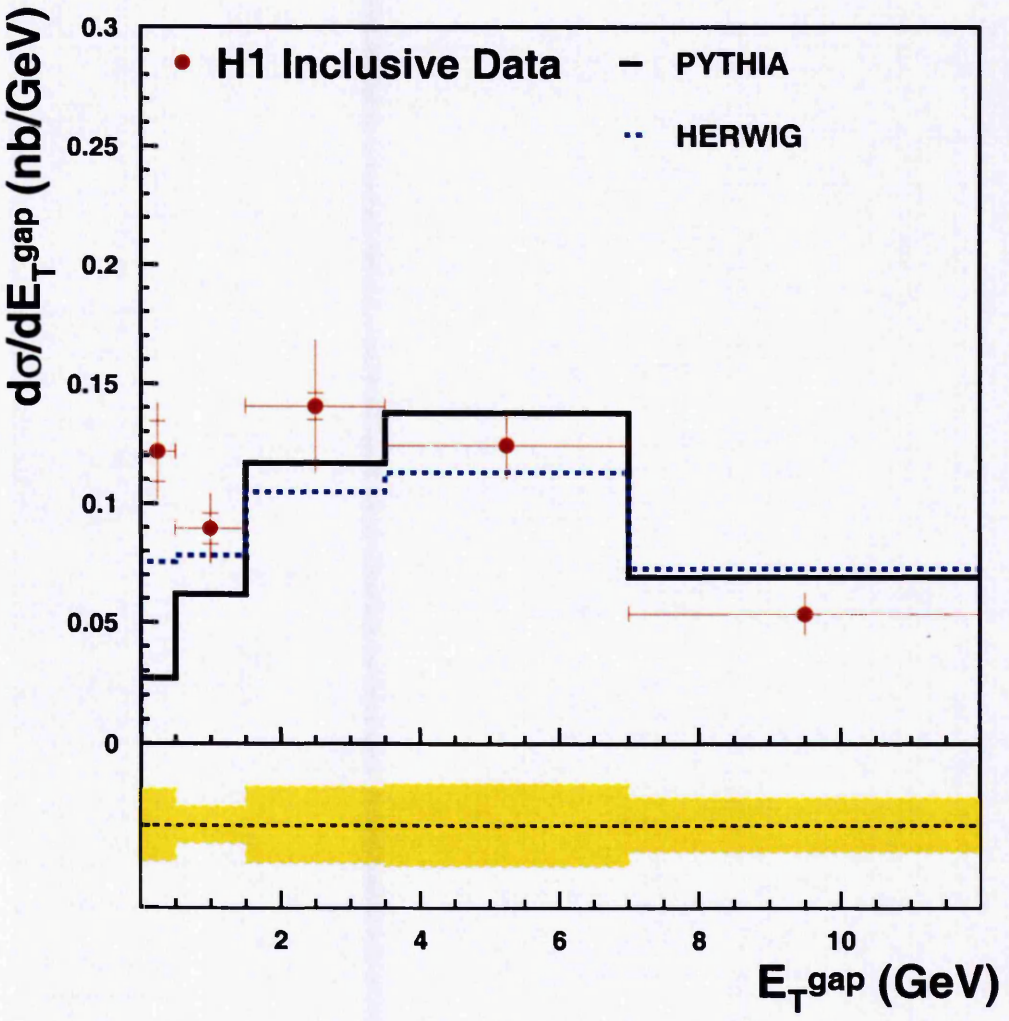

Figure 7.1: The dijet cross section differential in E_T^{gap}, the summed transverse energy between the two highest P_T jets, in the kinematic range defined in section 5.3. The inner error bars represent the statistical error and the outer error bars represent the statistical and non-correlated systematic errors added in quadrature. The solid band below the plot shows the correlated systematic errors on the same vertical scale as the plot. The solid line shows the prediction of PYTHIA and the dashed line that of HERWIG.

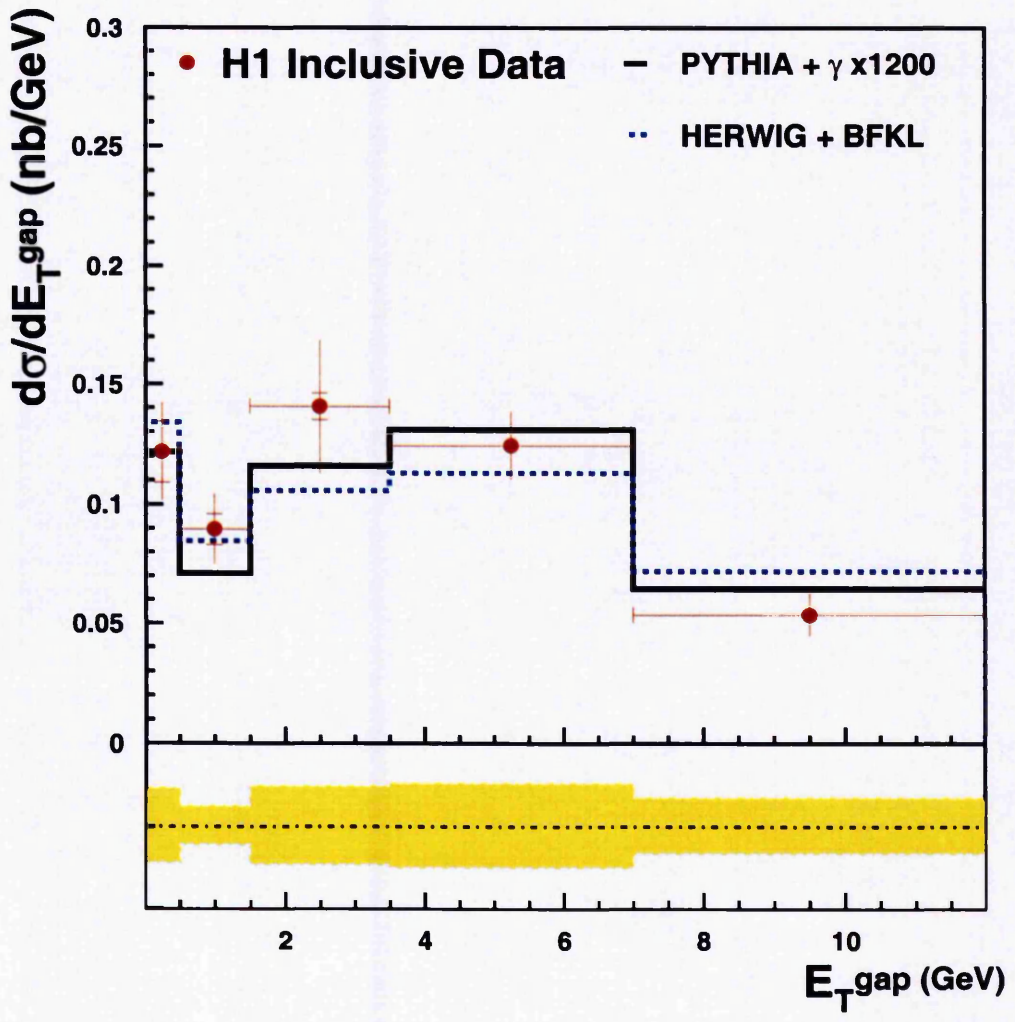

Figure 7.2: The dijet cross section differential in E_T^{gap}. The solid line shows the prediction of PYTHIA with high-$|t|$ γ exchange added and the dashed line shows the prediction of HERWIG with BFKL colour singlet exchange included.

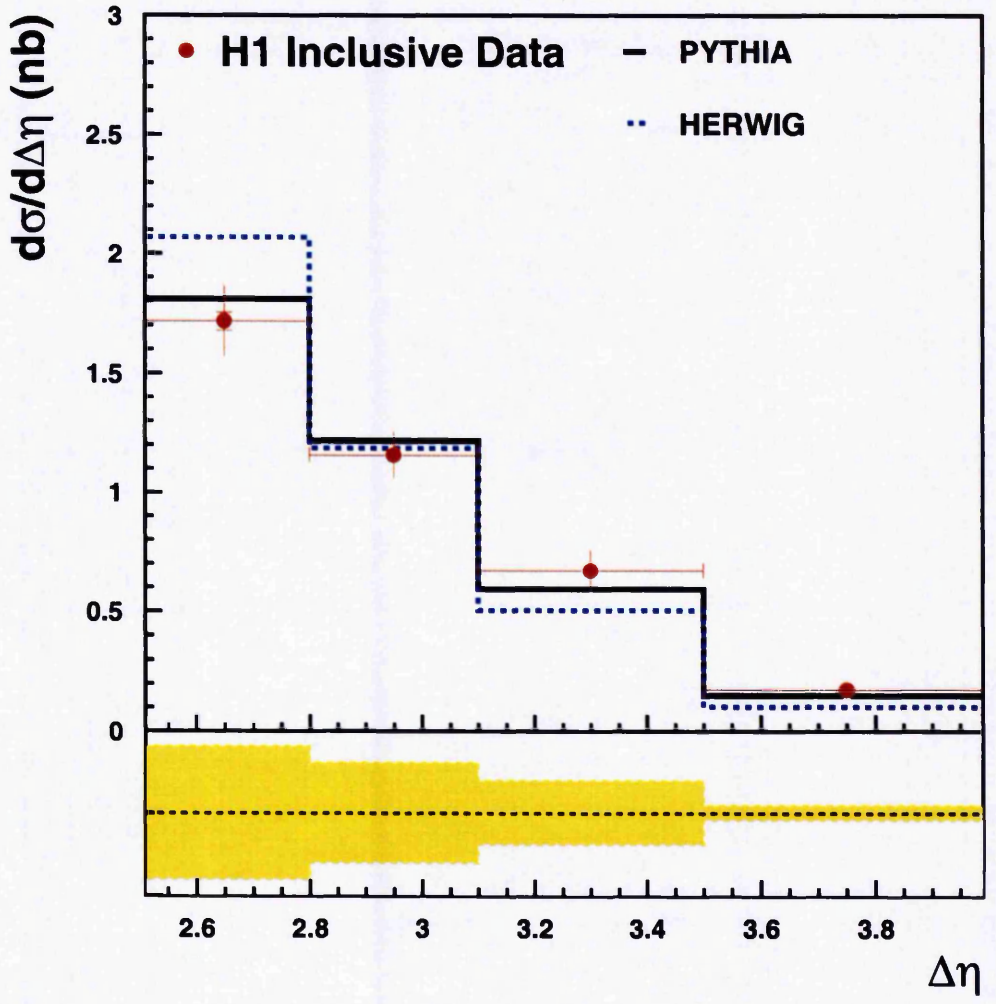

Figure 7.3: The dijet cross section differential in $\Delta\eta$. The solid line shows the prediction of PYTHIA and the dashed line that of HERWIG.

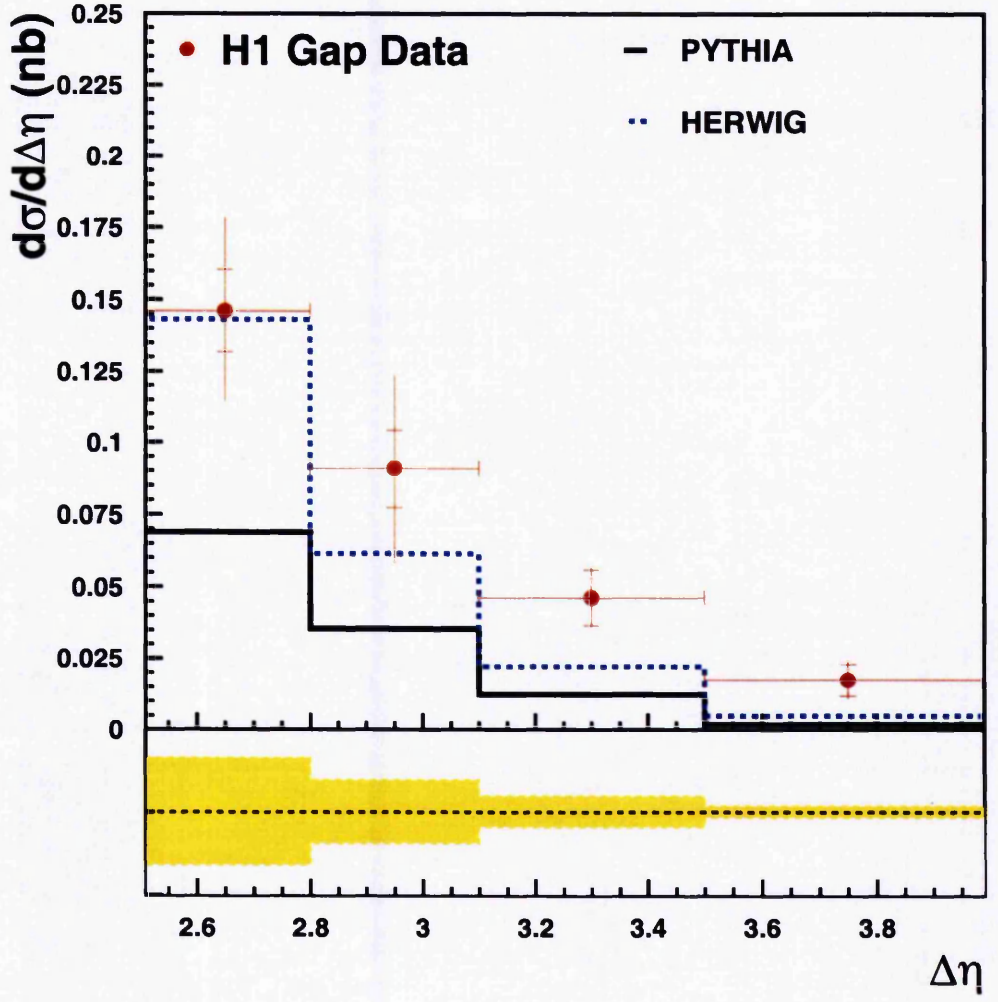

Figure 7.4: The dijet cross section differential in $\Delta\eta$, with the additional requirement that $E_T^{gap} < 1.0$ GeV. The solid line shows the prediction of PYTHIA and the dashed line that of HERWIG.

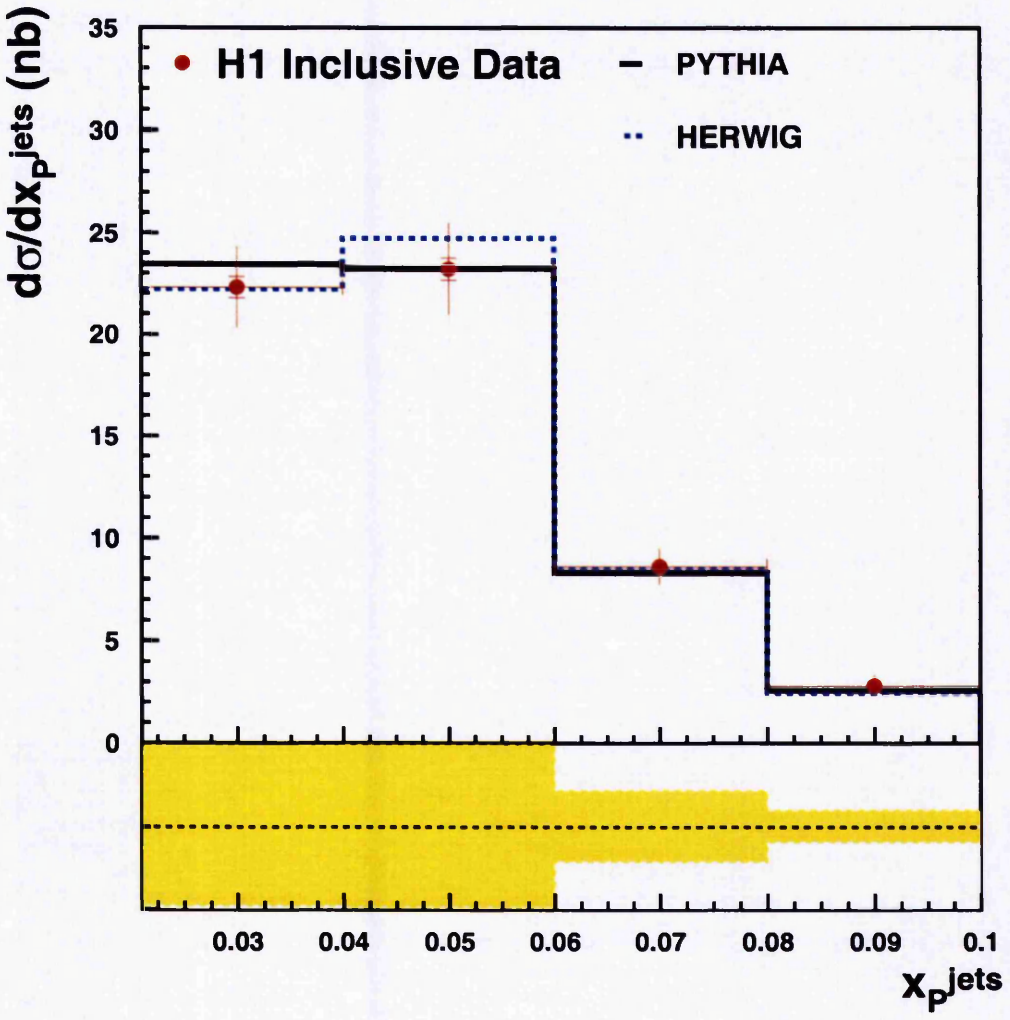

Figure 7.5: The dijet cross section differential in x_p^{jets}. The solid line shows the prediction of PYTHIA and the dashed line that of HERWIG.

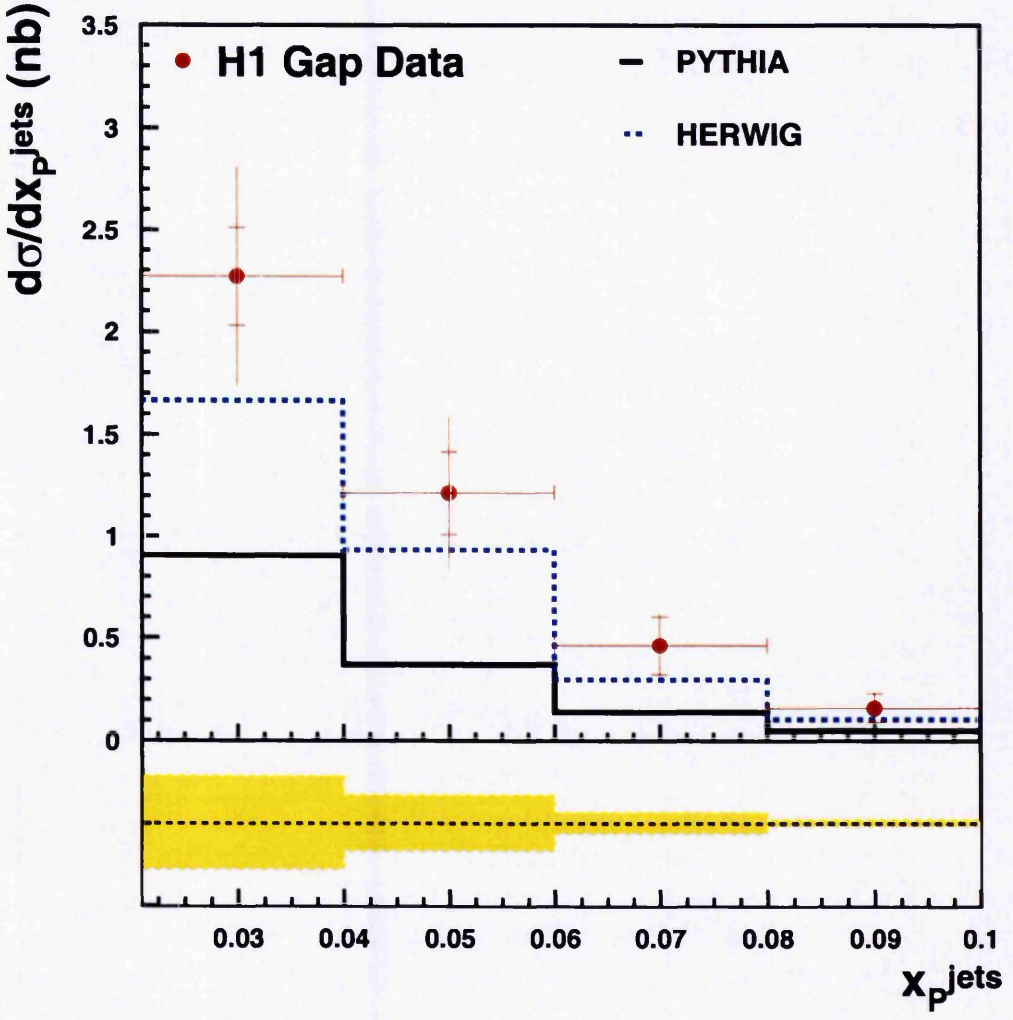

Figure 7.6: The dijet cross section differential in x_p^{jets}, with the additional requirement that $E_T^{gap} < 1.0$ GeV. The solid line shows the prediction of PYTHIA and the dashed line that of HERWIG.

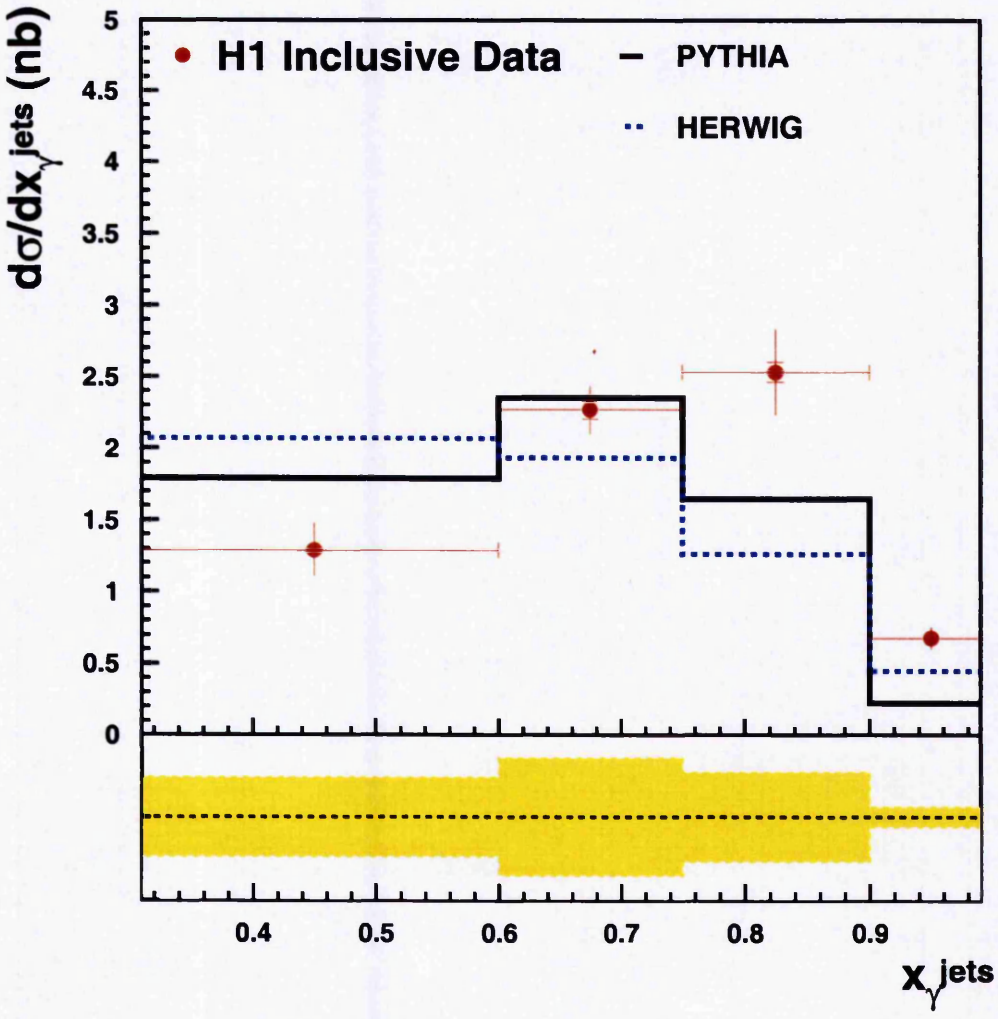

Figure 7.7: The dijet cross section differential in x_γ^{jets}. The solid line shows the prediction of PYTHIA and the dashed line that of HERWIG.

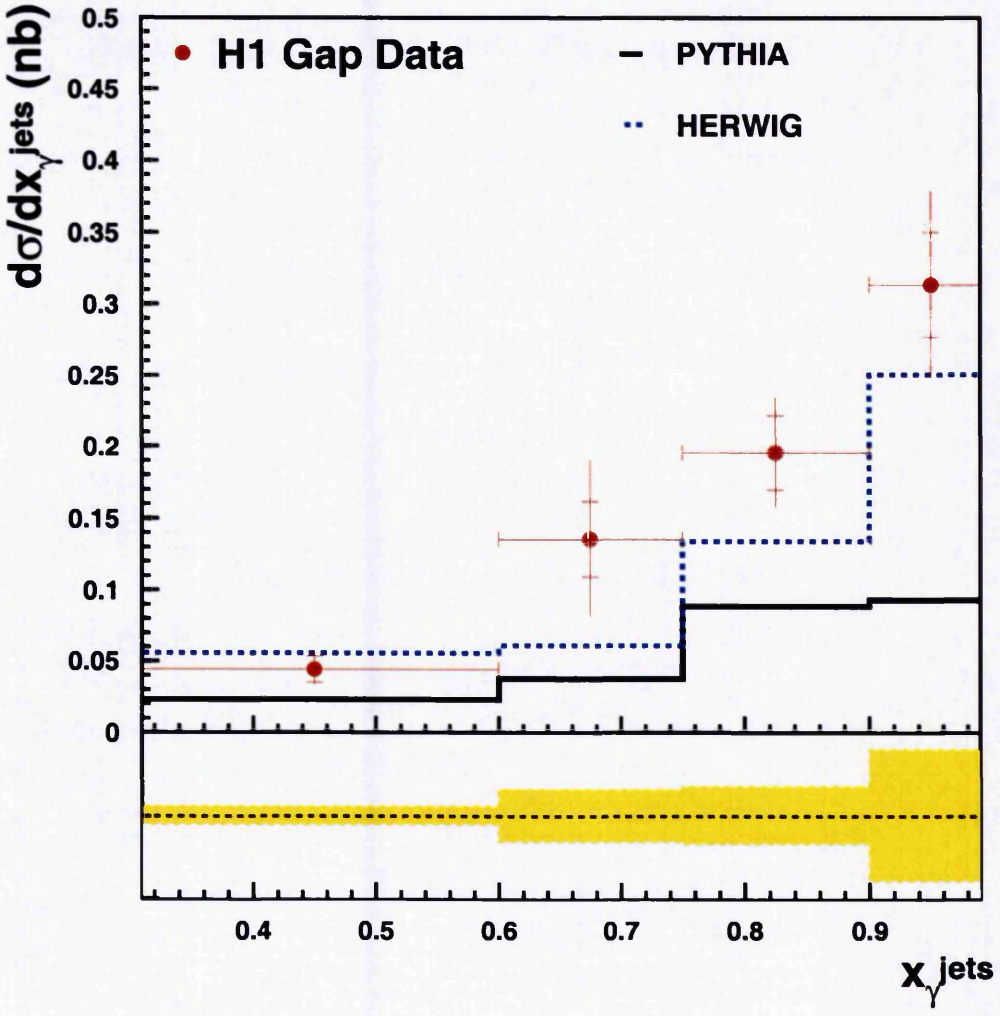

Figure 7.8: The dijet cross section differential in x_γ^{jets}, with the additional requirement that $E_T^{gap} < 1.0$ GeV. The solid line shows the prediction of PYTHIA and the dashed line that of HERWIG.

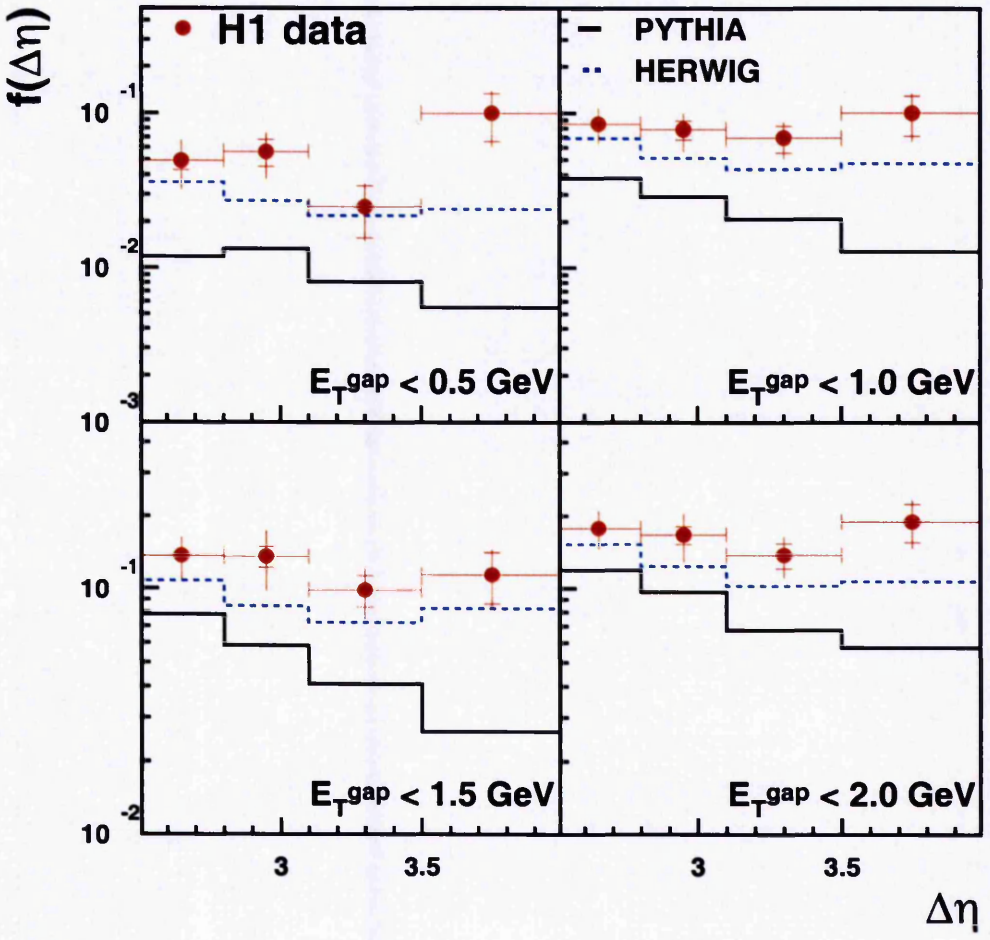

Figure 7.9: The gap fraction differential in $\Delta\eta$. Gap events are defined for four values of E_T^{gap}, shown in the figure. The inner error bars represent the statistical error and the outer error bars represent the statistical, non-correlated systematic errors and correlated systematic errors added in quadrature. The solid line shows the prediction of PYTHIA and the dashed line that of HERWIG.

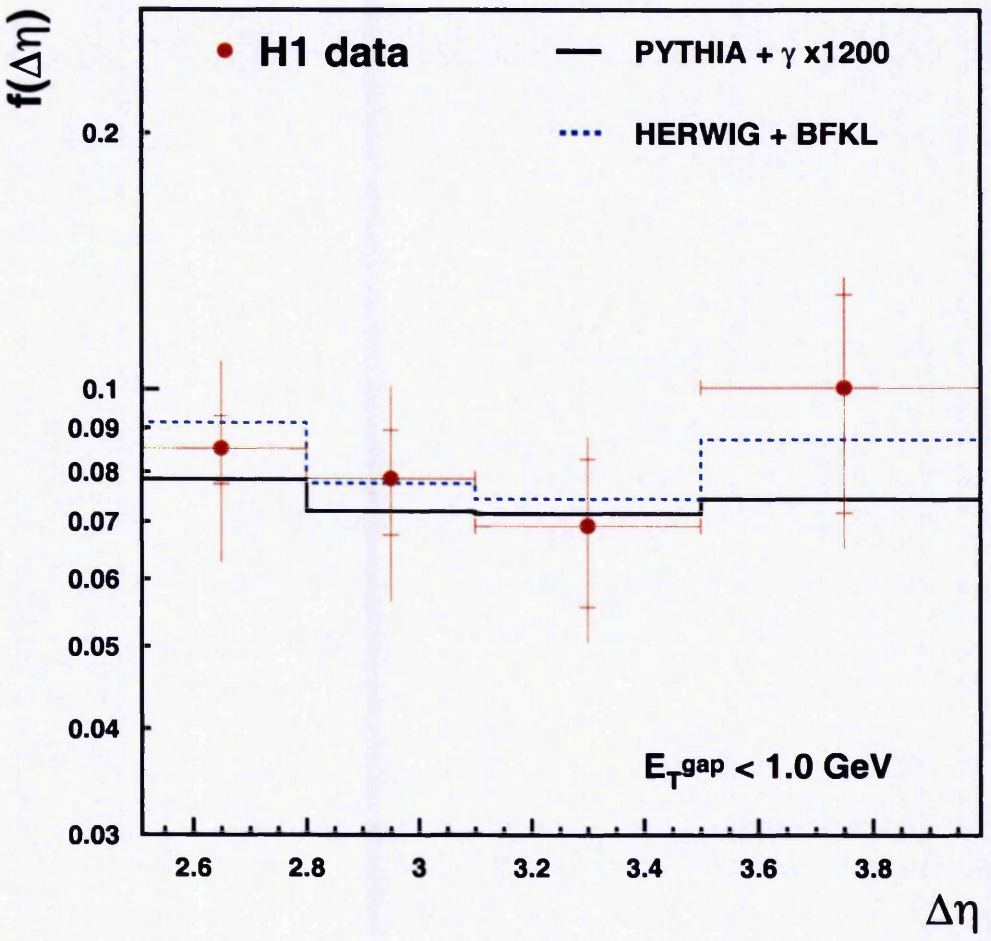

Figure 7.10: The gap fraction differential in $\Delta\eta$ for $E_T^{gap} < 1.0$ GeV and compared to different models of colour singlet exchange. The solid line shows the prediction of PYTHIA + high-$|t|$ γ exchange and the dashed line shows the prediction of the HERWIG + BFKL model.

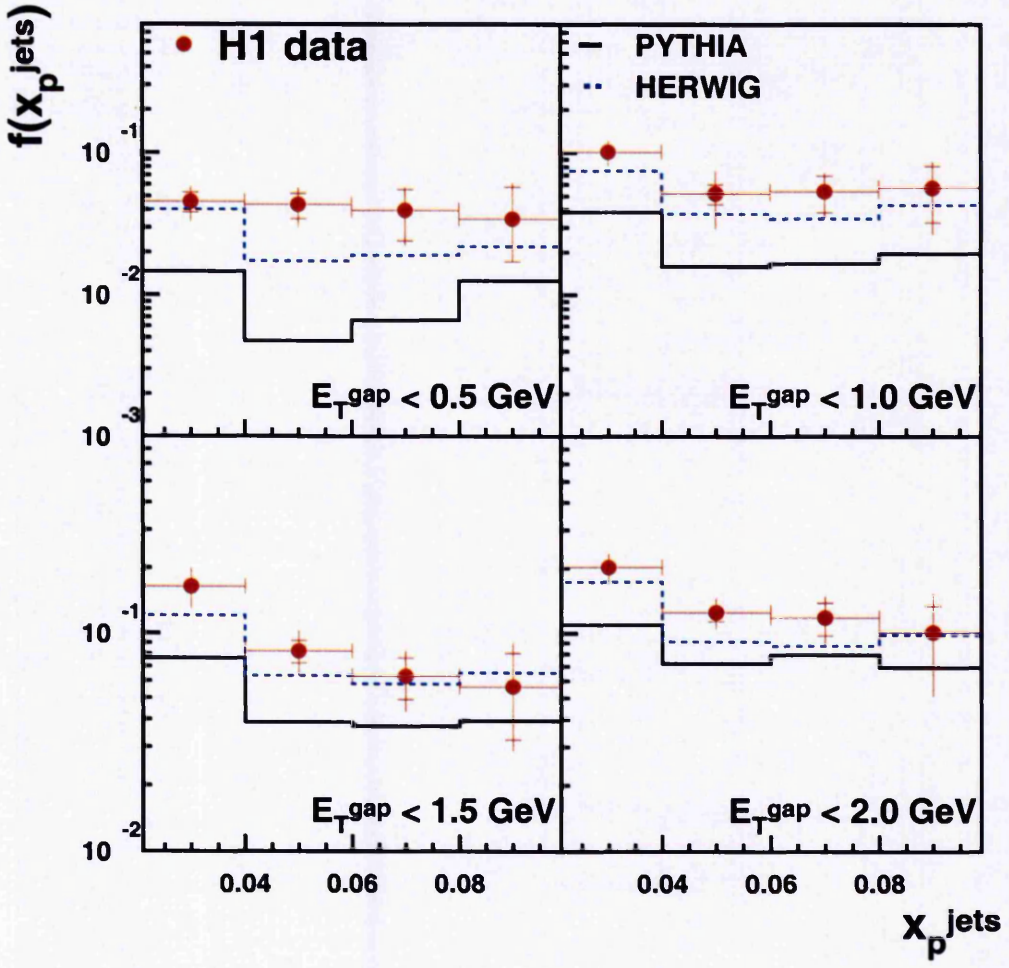

Figure 7.11: The gap fraction differential in x_p^{jets}. Gap events are defined for four values of E_T^{gap}, shown in the figure. The solid line shows the prediction of PYTHIA and the dashed line that of HERWIG.

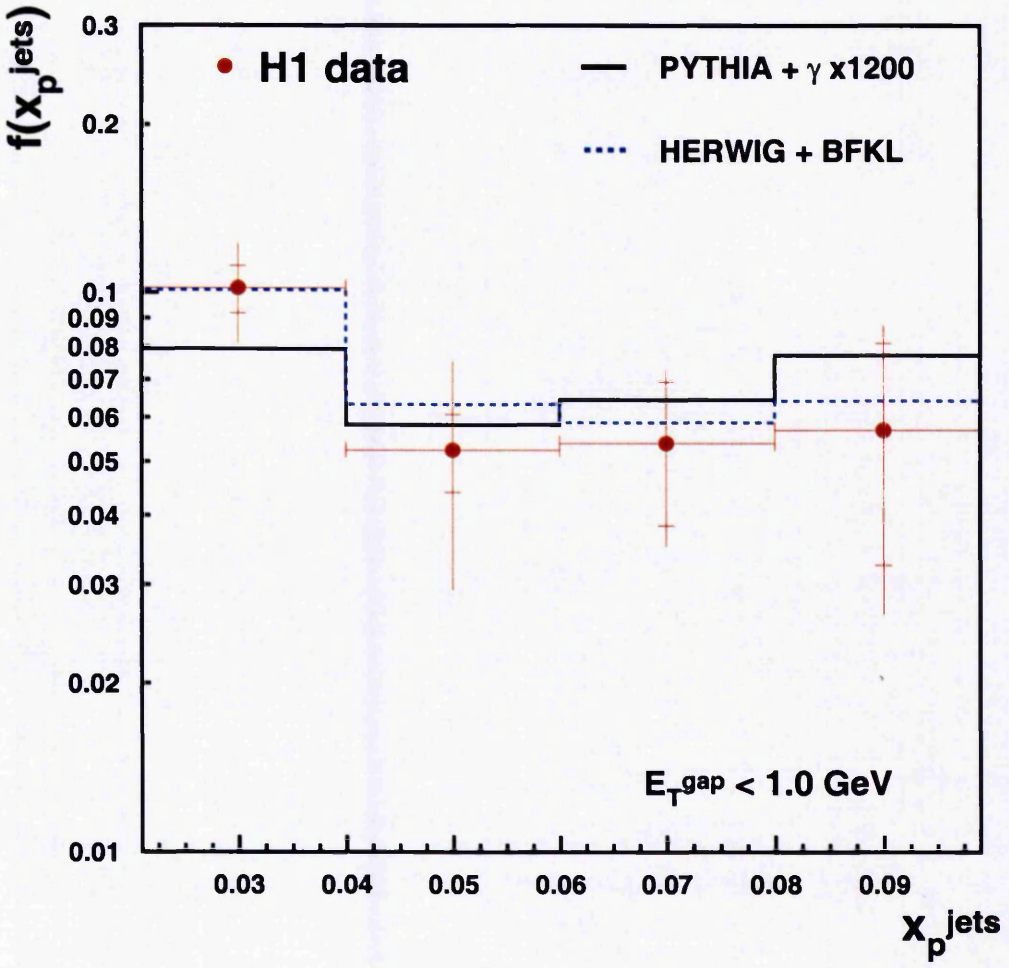

Figure 7.12: The gap fraction differential in x_p^{jets} for $E_T^{gap} < 1.0$ GeV and compared to different models of colour singlet exchange. The solid line shows the prediction of PYTHIA + high-$|t|$ γ exchange and the dashed line shows the prediction of the HERWIG + BFKL model.

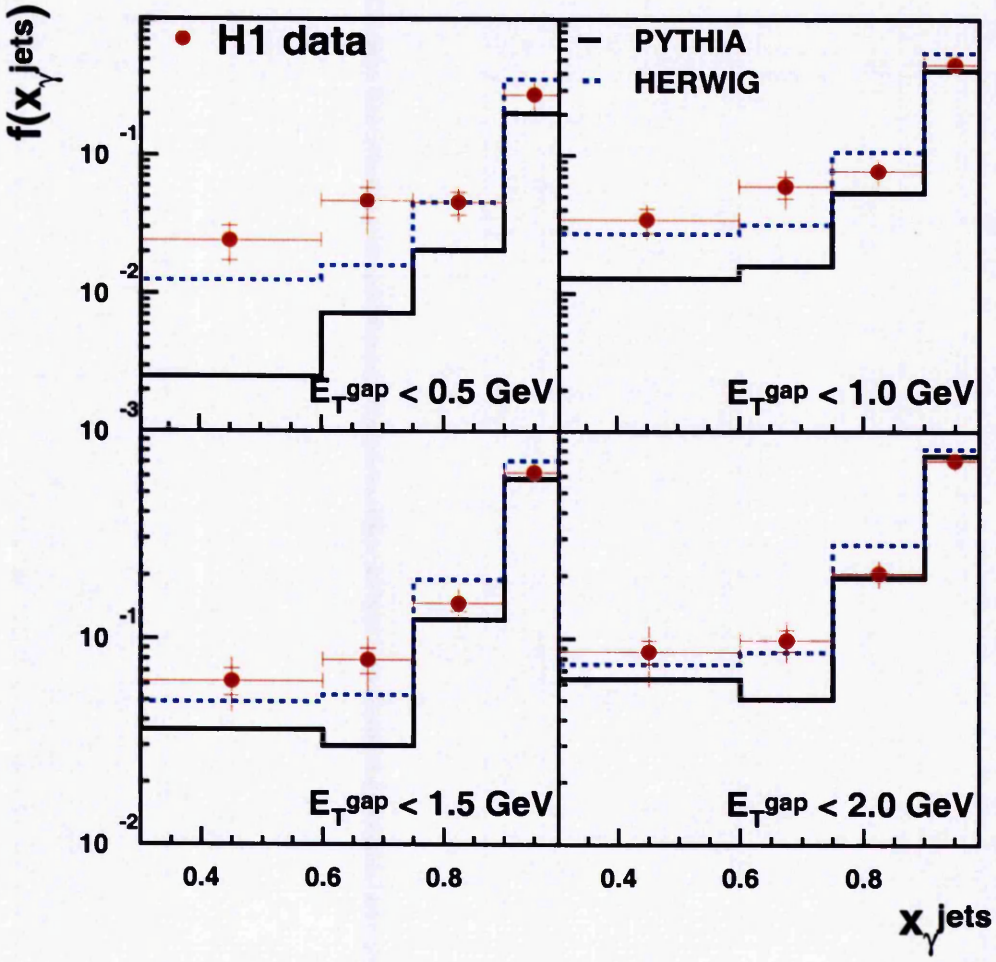

Figure 7.13: The gap fraction differential in x_γ^{jets}. Gap events are defined for four values of E_T^{gap}, shown in the figure. The solid line shows the prediction of PYTHIA and the dashed line that of HERWIG.

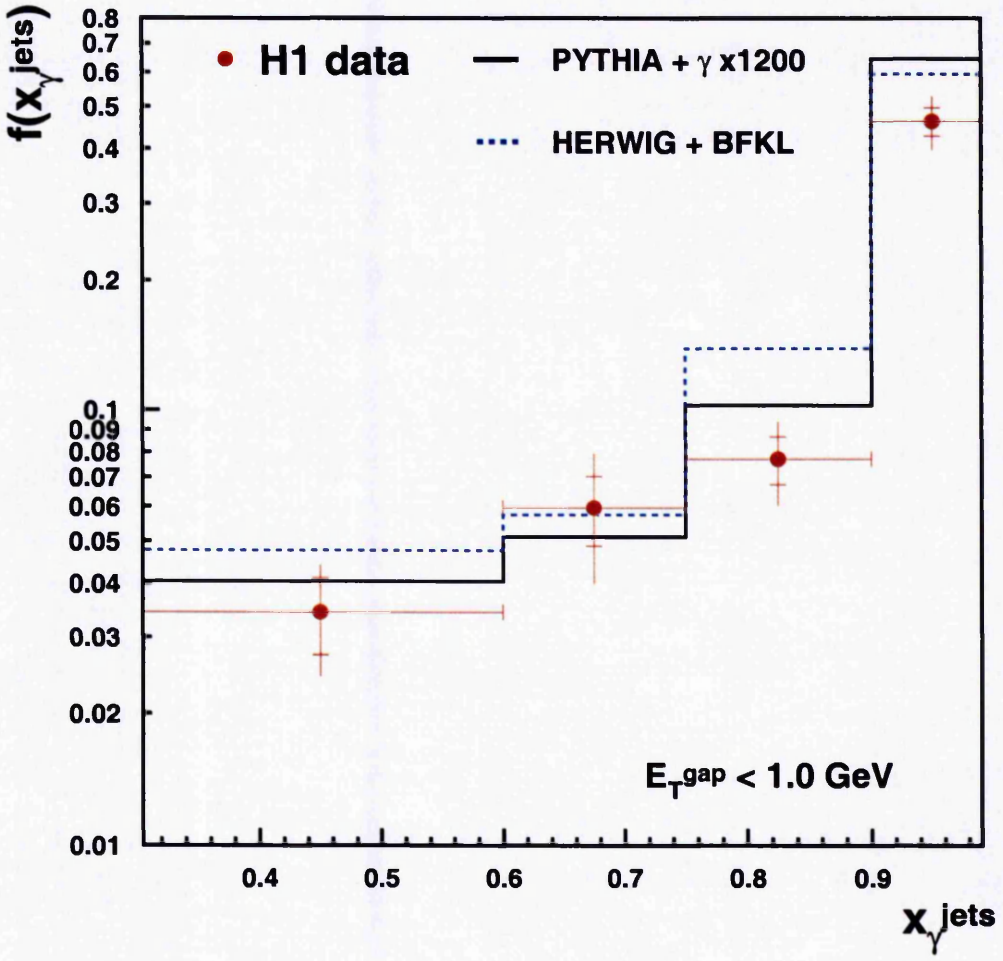

Figure 7.14: The gap fraction differential in $\Delta\eta$ for $E_T^{gap} < 1.0$ GeV and compared to different models of colour singlet exchange. The solid line shows the prediction of PYTHIA + high-$|t|$ γ exchange and the dashed line shows the prediction of the HERWIG + BFKL model.

Chapter 8

Summary

Diffractive processes in which the rapidity gap is produced at short distances can be studied by analysing events with rapidity gaps between jets. The hard scale involved in the process may enable pQCD calculations to be made. A significantly improved method of defining these events was used, for the first time, in the analysis presented in this thesis. This method reduces the background from non-colour singlet events, is relatively insensitive to activity at the edge of the gap, is infra-red safe and may enable perturbative calculations to be made of all the energy flow between the jets.

Photoproduction events were studied using the longitudinally invariant k_t algorithm to define jets. The dijet cross section was measured differentially in $\Delta\eta$, x_p^{jets}, x_γ^{jets} and E_T^{gap} in the kinematic range $P_T^{jet1} > 6$ GeV, $P_T^{jet2} > 5$ GeV, $\eta^{jets1,2} < 2.65$, $2.5 < \Delta\eta < 4.0$, $0.3 < y < 0.65$ and $Q^2 < 0.01$ GeV^2. This is the first time the dijet cross section has been measured differentially in x_p^{jets} and x_γ^{jets} in this kinematic region (large $\Delta\eta$) at HERA. The measurements were compared to the predictions of the PYTHIA and HERWIG event generators. A good agreement was found for the measurements differential in $\Delta\eta$ and x_p^{jets}, however the x_γ^{jets} distribution is poorly described by both generators.

An excess of events with small E_T^{gap} is observed over that predicted by the standard

photoproduction HERWIG and PYTHIA models. This is consistent with the presence of a strongly interacting colour singlet exchange. Events with low E_T^{gap} were studied further by measuring their cross section and the gap fraction differential in $\Delta\eta$, x_p^{jets} and x_γ^{jets}. The results were compared with two colour singlet models; high-t photon exchange, scaled up by three orders of magnitude, and BFKL exchange. Unfortunately, there was little sensitivity to the underlying dynamics of the model.

The fact that the data can be described by the addition of the leading order BFKL pomeron with a choice of $\alpha_s = 0.18$ is interesting, since this model was also able to describe the Tevatron data on gaps between jets. However, large uncertainties both in the standard photoproduction model and in the BFKL model prevent drawing strong conclusions. The differences between the HERWIG and PYTHIA models show the uncertainty in the hadronisation and multiple interaction models used. These differences must be understood in order to gain a good understanding of the colour singlet exchange events.

Future measurements will be able to use the large luminosity that will be available after the HERA luminosity upgrade. This will improve the precision of the measurements, which particularly at large x_p^{jets} and $\Delta\eta$ have large statistical errors. Higher P_T jets could also then be used, which would improve the systematic errors. These measurements may then be able to distinguish between colour singlet models, which will aid our understanding of the nature of the colour singlet exchange in high-t diffractive events.

Appendix A

The k_t Clustering Algorithm

The k_t clustering algorithm [55] is used in the inclusive mode [105] in this analysis. The algorithm starts by taking a list of particles and then merges pairs of particles that are close together in phase-space to form new pseudo-particles. This process is iterated until there are a few well separated pseudo-particles which are the output jets.

Starting from a list of particles the following algorithm is used:

1. For every pair of particles, i and j, define

$$d_{ij} = \min(E_{Ti}^2, E_{Tj}^2)\,\frac{R_{ij}^2}{R_0^2}, \quad R_{ij}^2 = \Delta\eta_{ij}^2 + \Delta\phi_{ij}^2 \tag{A.1}$$

where R_0 is an adjustable parameter, here set to $R_0 = 1$. Note that for $R_{ij}^2 \ll 1$

$$\min(E_{Ti}^2, E_{Tj}^2)R_{ij}^2 \approx \min(E_{Ti}^2, E_{Tj}^2)\theta_{ij}^2 \approx k_t^2. \tag{A.2}$$

2. For every particle, define

$$d_i = E_{Ti}^2. \tag{A.3}$$

3. If $\min(d_{ij}) < \min(d_i)$ then merge particles i and j, according to the given recombination scheme, forming a new pseudo-particle. Add the new particle to the particle list and remove i and j.

4. Else, if $\min(d_i) < \min(d_{ij})$ then jet i is complete. Remove the pseudo-particle from the particle list and add it to the list of jets.

5. The procedure is complete when the list of particles is empty. Every particle is assigned to a single jet.

The recombination of particles into jets is not unique. Different schemes are used to merge the two particles. Here, the p_t scheme is used which results in massless jets:

$$E_{Tij} = E_{Ti} + E_{Tj} \tag{A.4}$$

$$\eta_{ij} = (E_{Ti}\eta_i + E_{Tj}\eta_j)/E_{Tij} \tag{A.5}$$

$$\phi_{ij} = (E_{Ti}\phi_i + E_{Tj}\phi_j)/E_{Tij}. \tag{A.6}$$

In the final list of jets all opening angles within each jet are $R_{ij} < R_0$ and all opening angles between jets are $> R_0$. The value $R_0 = 1$ is strongly preferred theoretically since it sets initial and final state radiation on the same footing [54].

The advantages of this algorithm are that, firstly, every particle is unambiguously assigned to a jet so problems of overlapping jets are avoided and secondly that the algorithm is less sensitive to perturbations from soft particles (infra-red safe).

Appendix B

Tables of Results

x_γ^{jets}	$d\sigma/dx_\gamma^{jets}$ (nb)	δ_{stat} (nb)	δ_{uncor} (nb)	δ_{corr} (nb)
0.30 - 0.60	1.29	0.03	0.19	0.28
0.60 - 0.75	2.27	0.06	0.16	0.41
0.75 - 0.90	2.53	0.07	0.29	0.31
0.90 - 1.00	0.68	0.05	0.07	0.07
x_p^{jets}	$d\sigma/dx_p^{jets}$ (nb)	δ_{stat} (nb)	δ_{uncor} (nb)	δ_{corr} (nb)
0.02 - 0.04	22.3	0.5	2.0	3.9
0.04 - 0.06	23.2	0.6	2.2	3.9
0.06 - 0.08	08.6	0.3	0.9	1.7
0.08 - 0.10	02.8	0.2	0.5	0.8
$\Delta\eta$	$d\sigma/d\Delta\eta$ (nb)	δ_{stat} (nb)	δ_{uncor} (nb)	δ_{corr} (nb)
2.5 - 2.8	1.72	0.04	0.14	0.28
2.8 - 3.1	1.16	0.03	0.09	0.21
3.1 - 3.5	0.67	0.02	0.08	0.13
3.5 - 4.0	0.17	0.01	0.02	0.03
E_T^{gap} (GeV)	$d\sigma/dE_T^{gap}$ (nb/GeV)	δ_{stat} (nb/GeV)	δ_{uncor} (nb/GeV)	δ_{corr} (nb/GeV)
0.0 - 0.50	0.122	0.013	0.016	0.015
0.5 - 1.50	0.089	0.006	0.013	0.008
1.5 - 3.50	0.141	0.005	0.027	0.016
3.5 - 7.00	0.124	0.003	0.014	0.018
7.0 - 12.0	0.054	0.001	0.009	0.012

Table B.1: The dijet cross section differential in x_γ^{jets}, x_p^{jets}, $\Delta\eta$ and E_t^{gap}. The statistical error, δ_{stat}, uncorrelated systematic error, δ_{uncor}, and correlated systematic error, δ_{corr}, on each measurement are given.

E_T^{cut} (GeV)	x_γ^{jets}	$d\sigma/dx_\gamma^{jets}$ (nb)	δ_{stat} (nb)	δ_{uncor} (nb)	δ_{corr} (nb)	$f(x_\gamma^{jets})$	δ_{stat}	δ_{syst}
0.5	0.30 - 0.60	0.031	0.009	0.005	0.004	0.024	0.007	0.009
0.5	0.60 - 0.75	0.105	0.027	0.058	0.017	0.046	0.011	0.021
0.5	0.75 - 0.90	0.115	0.022	0.022	0.014	0.045	0.008	0.013
0.5	0.90 - 1.00	0.188	0.030	0.040	0.027	0.277	0.035	0.065
1.0	0.30 - 0.60	0.044	0.009	0.006	0.006	0.034	0.007	0.010
1.0	0.60 - 0.75	0.135	0.026	0.049	0.018	0.060	0.011	0.020
1.0	0.75 - 0.90	0.195	0.026	0.030	0.020	0.077	0.010	0.017
1.0	0.90 - 1.00	0.313	0.037	0.054	0.046	0.462	0.034	0.068
1.5	0.30 - 0.60	0.080	0.013	0.027	0.010	0.062	0.009	0.019
1.5	0.60 - 0.75	0.178	0.027	0.061	0.019	0.079	0.011	0.024
1.5	0.75 - 0.90	0.373	0.037	0.052	0.029	0.147	0.013	0.025
1.5	0.90 - 1.00	0.423	0.041	0.056	0.054	0.623	0.028	0.065
2.0	0.30 - 0.60	0.111	0.015	0.047	0.017	0.086	0.011	0.028
2.0	0.60 - 0.75	0.223	0.028	0.054	0.033	0.098	0.012	0.023
2.0	0.75 - 0.90	0.520	0.040	0.069	0.044	0.205	0.013	0.031
2.0	0.90 - 1.00	0.483	0.042	0.072	0.060	0.712	0.024	0.078

Table B.2: The dijet cross section differential in x_γ^{jets}, with the additional requirement that $E_t^{gap} < E_t^{cut}$. Also shown are the gap fractions, $f(x_\gamma^{jets})$, defined as the fraction of all dijet events with $E_t^{gap} < E_t^{cut}$, and their associated statistical, δ_{stat}, and total systematic, δ_{syst}, errors.

E_T^{cut} (GeV)	x_p^{jets}	$d\sigma/dx_p^{jets}$ (nb)	δ_{stat} (nb)	δ_{uncor} (nb)	δ_{corr} (nb)	$f(x_p^{jets})$	δ_{stat}	δ_{syst}
0.5	0.02 - 0.04	1.02	0.17	0.22	0.09	0.046	0.007	0.013
0.5	0.04 - 0.06	1.01	0.21	0.18	0.12	0.044	0.009	0.014
0.5	0.06 - 0.08	0.34	0.14	0.06	0.04	0.040	0.016	0.018
0.5	0.08 - 0.10	0.10	0.07	0.03	0.01	0.034	0.024	0.028
1.0	0.02 - 0.04	2.27	0.24	0.48	0.23	0.102	0.010	0.021
1.0	0.04 - 0.06	1.21	0.20	0.32	0.14	0.052	0.008	0.023
1.0	0.06 - 0.08	0.46	0.14	0.07	0.05	0.054	0.015	0.019
1.0	0.08 - 0.10	0.16	0.07	0.04	0.02	0.057	0.024	0.030
1.5	0.02 - 0.04	3.67	0.32	1.06	0.43	0.165	0.012	0.036
1.5	0.04 - 0.06	1.92	0.25	0.24	0.15	0.083	0.010	0.020
1.5	0.06 - 0.08	0.54	0.12	0.10	0.09	0.063	0.014	0.020
1.5	0.08 - 0.10	0.16	0.07	0.03	0.01	0.057	0.024	0.034
2.0	0.02 - 0.04	4.52	0.33	0.79	0.48	0.202	0.012	0.033
2.0	0.04 - 0.06	2.91	0.30	0.40	0.32	0.125	0.011	0.021
2.0	0.06 - 0.08	1.02	0.20	0.26	0.14	0.118	0.020	0.032
2.0	0.08 - 0.10	0.28	0.10	0.06	0.02	0.101	0.033	0.052

Table B.3: The dijet cross section differential in x_p^{jets}, with the additional requirement that $E_t^{gap} < E_t^{cut}$. Also shown are the gap fractions, $f(x_p^{jets})$, defined as the fraction of all dijet events with $E_t^{gap} < E_t^{cut}$, and their associated statistical, δ_{stat}, and total systematic, δ_{syst}, errors.

E_T^{cut} (GeV)	$\Delta\eta$	$d\sigma/d\Delta\eta$ (nb)	δ_{stat} (nb)	δ_{uncor} (nb)	δ_{corr} (nb)	$f(\Delta\eta)$	δ_{stat}	δ_{syst}
0.5	2.5 - 2.8	0.085	0.011	0.023	0.012	0.050	0.006	0.018
0.5	2.8 - 3.1	0.065	0.014	0.024	0.009	0.056	0.011	0.019
0.5	3.1 - 3.5	0.017	0.006	0.003	0.002	0.025	0.009	0.010
0.5	3.5 - 4.0	0.017	0.007	0.004	0.002	0.100	0.034	0.039
1.0	2.5 - 2.8	0.146	0.014	0.029	0.019	0.085	0.008	0.023
1.0	2.8 - 3.1	0.091	0.014	0.030	0.011	0.079	0.011	0.022
1.0	3.1 - 3.5	0.046	0.010	0.004	0.005	0.069	0.014	0.019
1.0	3.5 - 4.0	0.017	0.006	0.004	0.002	0.101	0.029	0.035
1.5	2.5 - 2.8	0.234	0.019	0.030	0.021	0.137	0.010	0.027
1.5	2.8 - 3.1	0.157	0.018	0.058	0.020	0.136	0.014	0.038
1.5	3.1 - 3.5	0.066	0.011	0.006	0.007	0.099	0.014	0.024
1.5	3.5 - 4.0	0.020	0.005	0.002	0.002	0.114	0.027	0.032
2.0	2.5 - 2.8	0.305	0.020	0.038	0.030	0.178	0.010	0.033
2.0	2.8 - 3.1	0.193	0.019	0.054	0.022	0.167	0.014	0.039
2.0	3.1 - 3.5	0.092	0.012	0.013	0.010	0.137	0.016	0.027
2.0	3.5 - 4.0	0.033	0.007	0.006	0.005	0.189	0.034	0.044

Table B.4: The dijet cross section differential in $\Delta\eta$, with the additional requirement that $E_t^{gap} < E_t^{cut}$. Also shown are the gap fractions, $f(\Delta\eta)$, defined as the fraction of all dijet events with $E_t^{gap} < E_t^{cut}$, and their associated statistical, δ_{stat}, and total systematic, δ_{syst}, errors.

References

[1] I. Abt *et al.* [H1 Collaboration], Nucl. Instrum. Meth. A **386** (1997) 310; 348.

[2] B. Andrieu *et al.* [H1 Calorimeter Group Collaboration], Nucl. Instrum. Meth. A **336**, (1993) 460.

[3] B. Andrieu *et al.* [H1 Calorimeter Group Collaboration], Nucl. Instrum. Meth. A **344** (1994) 492.

[4] H.P. Wellisch, J.P. Kubenka, H. Oberlack, P.Schacht, *Hadronic Calibration of the H1 LAr Calorimeter using Software Weighting Techniques*, **H1-02/94-346** (1994).

[5] B. Andrieu *et al.* [H1 Calorimeter Group Collaboration], Nucl. Instrum. Meth. A **350** (1994) 57.

[6] B. Andrieu *et al.* [H1 Calorimeter Group Collaboration], Nucl. Instrum. Meth. A **336** (1993) 499.

[7] B. Heineman, *Measurement of Charged Current snd Neutral Current Cross sections in Positron-Proton Collisions at* $\sqrt{s} \simeq 300\,\mathrm{GeV}$, Ph.D. thesis, University of Hamburg (1999).

[8] M. Wobisch, *Measurement and QCD Analysis of Jet Cross Sections in Deep-Inelastic Positron-Proton Collisions at* $\sqrt{s} \simeq 300\,\mathrm{GeV}$, Ph.D. thesis, Aachen (2000).

[9] R. D. Appuhn *et al.* [H1 SPACAL Group Collaboration], Nucl. Instrum. Meth. A **386** (1997) 397.

[10] R. D. Appuhn *et al.* [H1 SPACAL GROUP Collaboration], Nucl. Instrum. Meth. A **382** (1996) 395.

[11] T. Nicholls *et al.* [H1 SPACAL Group Collaboration], Nucl. Instrum. Meth. A **374** (1996) 149.

[12] R. D. Appuhn *et al.* [H1 SPACAL Group Collaboration], DESY-96-013.

[13] A. A. Glazov, *Measurement of the Proton Structure Functions* $F_2(x, Q^2)$ *and* $F_L(x, Q^2)$ *with the H1 Detector at HERA.*, Ph.D. thesis, University of Berlin (1998).

[14] J. Burger *et al.*, Nucl. Instrum. Meth. A **279** (1989) 217.

[15] S. Egli, C. A. Meyer, P. Robmann, U. Straumann, P. Truol, R. Eichler and R. Holzreuter, Nucl. Instrum. Meth. A **283** (1989) 487.

[16] K. Muller *et al.*, Nucl. Instrum. Meth. A **312** (1992) 457.

[17] S. Burger *et al.*, RAL **95-037**, DESY **95-132**.

[18] P. Biddulph *et al.*, Nucl. Instrum. Meth. A **340**, (1994) 304.

[19] H. Bethe, W. Heitler, Proc. Roy. Soc. **A146** (1934) 83.

[20] T. Ahmed *et al.* [H1 Collaboration], Z. Phys. **C66** (1995) 529.

[21] H1 Collaboration, *Luminosity Measurement in the H1 Experiment at HERA*, ICHEP 96-Warsaw, (1996), 17-26.

[22] E. Elsen, *The H1 Trigger and Data Acquisition.* Proc. of the 'International Symposium on Electronic Instrumentation in Physics', Dubna, May 1991. **H1-93-262**.

F. Sefkow *et al.*, *Experience with the First Level Trigger of H1.* Proc of the 1994 IEEE Nuclear Science Symposium, Norfolk, Virginia. **H1-94-407.**

[23] S. Eichenberger *et al.*, Nucl. Instrum. Meth. A **323** (1992) 532.

[24] R. Brun *et al*, GEANT3 User's guide, CERN-DD/EE-84-1 (1987).

[25] T. Sjostrand, Comput. Phys. Commun. **82** (1994) 74.

[26] G. Marchesini, B. R. Webber, G. Abbiendi, I. G. Knowles, M. H. Seymour and L. Stanco, Comput. Phys. Commun. **67** (1992) 465.

[27] C. Adloff *et al.* [H1 Collaboration], Eur. Phys. J. C **13** (2000) 609.

[28] C. Adloff *et al.* [H1 Collaboration], Eur. Phys. J. C **19** (2001) 269.

[29] F. Halzen and A. Martin, *Quarks and Leptons*, John Wiley (1984).

[30] C. Adloff *et al.* [H1 Collaboration], hep-ex/0012053.

[31] A. C. Benvenuti *et al.* [BCDMS Collaboration], Phys. Lett. B **223** (1989) 485.

[32] M. Arneodo *et al.* [New Muon Collaboration], Phys. Lett. B **309** (1993) 222.

[33] E. D. Bloom *et al.*, Phys. Rev. Lett. **23** (1969) 930;
M. Breidenbach *et al.*, Phys. Rev. Lett. **23** (1969) 935;
J. I. Freidman and H. W. Kendall, Ann. Rev. Nucl. Part. Sci. **22** (1972) 203.

[34] J. D. Bjorken Phys. Rev. **179** (1969) 1547.

[35] R. P. Feynman, Phys. Rev. Lett. **23** (1969) 1415;
J. D. Bjorken and E. A. Paschos, Phys. Rev. **185** (1969) 1975.

[36] C. G. Callan and D. J. Gross, Phys. Rev. Lett. **22** (1969) 156.

[37] G. Moreno *et al.*, Phys. Rev. D **43** (1991) 2815.

[38] G. Altarelli and G. Martinelli, Phys. Lett. B **76** (1978) 89;
M. Gluck and E. Reya, Nucl. Phys. B **145** (1978) 24.

[39] S. Aid *et al.* [H1 Collaboration], Nucl. Phys. **B470** (1996) 3.

[40] M. Derrick *et al.*, Z. Phys. **C72** (1996) 399.

[41] Y. L. Dokshitzer, Sov. Phys. JETP **46** (1977) 641;
V. N. Gribov and L. N. Lipatov, Sov. J. Nucl. Phys. **15** (1972) 438 and 675;
G. Altarelli and G. Parisi, Nucl. Phys. B **126** (1977) 298.

[42] G. Curci, W. Furmanski and R. Petronzio, Nucl. Phys. B **175** (1980) 27;
W. Furmanski and R. Petronzio, Phys. Lett. B **97** (1980) 437.

[43] A. D. Martin, R. G. Roberts, W. J. Stirling and R. S. Thorne, Eur. Phys. J. C **4** (1998) 463.

[44] E. A. Kuraev, L. N. Lipatov and V. S. Fadin, Sov. Phys. JETP **45** (1977) 199;
I. I. Balitsky and L. N. Lipatov, Sov. J. Nucl. Phys. **28** (1978) 822.

[45] V. S. Fadin and L. N. Lipatov, Phys. Lett. B **429** (1998) 127.

[46] S. Aid *et al.* [H1 Collaboration], Nucl. Phys. B **470** (1996) 3.

[47] C. Adloff *et al.* [H1 Collaboration], Nucl. Phys. B **538** (1999) 3.

[48] J. Breitweg *et al.* [ZEUS Collaboration], Phys. Lett. B **487** (2000) 53;
C. Adloff *et al.* [H1 Collaboration], submitted to Phys. Lett. B (2001).

[49] C. Weizsäcker, Z. Phys. **88** (1934) 612;
E. Williams, Phys. Rev. **45** (1934) 729.

[50] M. Krawczyk, A. Zembrzuski and M. Staszel, Phys. Rept. **345** (2001) 265.

[51] C. Adloff *et al.* [H1 Collaboration], Phys. Lett. B **483** (2000) 36.

[52] C. Adloff *et al.* [H1 Collaboration], Eur. Phys. J. **C10** (1999) 363.

[53] M. Gluck, E. Reya, A. Vogt, Phys. Rev. **D46** (1992) 1973;
M. Gluck, E. Reya,A. Vogt, Z. Phys. **C53** (1992) 127;
H. Abramowicz, K. Charchula, A. Levy, Phys. Lett. B **269** (1991) 458;
M. Gluck, E. Reya, I. Schienbein, Phys. Rev. **D60** (1999) 54019;
G. A. Schuler, T. Sjöstrand, Phys. Lett. B **376** (1996) 193.

[54] M. H. Seymour, Talk given at 10th Topical Workshop on Proton-Antiproton Collider Physics, Batavia, IL, 9-13 May 1995, hep-ph/9506421.

[55] S. Catani, Y. L. Dokshitzer, M. H. Seymour and B. R. Webber, Nucl. Phys. B **406** (1993) 187.

[56] B. Andersson, G. Gustafson, G. Ingelman and T. Sjostrand, Phys. Rept. **97** (1983) 31.

[57] T. Sjostrand and M. Bengtsson, Comput. Phys. Commun. **43** (1987) 367.

[58] B. R. Webber, Nucl. Phys. B **238** (1984) 492.

[59] I. Abt *et al.* [H1 Collaboration], Phys. Lett. B **314** (1993) 436;
T. Ahmed *et al.* [H1 Collaboration], Nucl. Phys. B **445** (1995) 195.

[60] J. M. Butterworth, J. R. Forshaw and M. H. Seymour, Z. Phys. C **72** (1996) 637.

[61] S. Aid *et al.* [H1 Collaboration], Z. Phys. C **70** (1996) 17.

[62] S. D. Ellis, hep-ph/9306280.

[63] C. Adloff *et al.* [H1 Collaboration], Eur. Phys. J. C **1** (1998) 97.

[64] T. Sjostrand and M. van Zijl, Phys. Rev. D **36** (1987) 2019.

[65] T. Regge, Nuovo Cim. **14** (1959) 951;
T. Regge, Nuovo Cim. **18** (1960) 947.

[66] J. R. Forshaw and D. A. Ross. *Quantum Chromodynamics and the Pomeron*, Cambridge University Press (1997).

[67] A. C. Irving and R. P. Worden, Phys. Rept. **34** (1977) 117;
P. D. B. Collins, *Introduction to Regge Theory and High Energy Physics*, Cambridge University Press (1977).

[68] A. Donnachie and P. V. Landshoff, Phys. Lett. B **437** (1998) 408.

[69] A. Sommerfeld, *Partial Differential Equations in Physics*, Academic Press (1949).

[70] G. N. Watson, Proc. Roy. Soc. **95** (1918) 83.

[71] G. F. Chew and S. C. Frautschi, Phys. Rev. Lett. **7** (1961) 394;
G. F. Chew and S. C. Frautschi, Phys. Rev. Lett. **8** (1962) 41.

[72] A. V. Barnes *et al.*, Phys. Rev. Lett. **37** (1976) 76.

[73] I. Y. Pomeranchuk, Sov. Phys. **3** (1956) 306;
L. B. Okun and I. Y. Pomeranchuk, Sov. Phys. JETP **3** (1956) 307.

[74] L. F. Foldy and R. F. Peierls, Phys. Rev. **130** (1963) 1585.

[75] A. S. Carroll *et al.*, Phys. Lett. B **80** (1979) 423;
G. Carboni *et al.*, Phys. Lett. B **113** (1982) 87.

[76] I. Y. Pomeranchuk, Sov. Phys. **7** (1958) 499.

[77] A. Donnachie and P. V. Landshoff, Phys. Lett. B **296** (1992) 227.

[78] S. Aid *et al.* [H1 Collaboration], Z. Phys. C **69** (1995) 27.

[79] P. Newman [H1 Collaboration], hep-ex/9901026.

[80] J. Breitweg *et al.* [ZEUS Collaboration], Eur. Phys. J. C **2** (1998) 247;
S. Aid *et al.* [H1 Collaboration], Nucl. Phys. B **463** (1996) 3;
M. Derrick *et al.* [ZEUS Collaboration], Z. Phys. C **73** (1996) 73;
J. Breitweg *et al.* [ZEUS Collaboration], Phys. Lett. B **437** (1998) 432;
H1 Collaboration, Conf paper 574, 29^{th} Intern. Conf. on HEP, Vancouver, Canada (1998);
M. Derrick *et al.* [ZEUS Collaboration], Phys. Lett. B **377** (1996) 259;
S. Aid *et al.* [H1 Collaboration], Nucl. Phys. B **472** (1996) 3;
J. Breitweg *et al.* [ZEUS Collaboration], Z. Phys. C **75** (1997) 215;
H1 Collaboration, Conf paper 572, 29^{th} Intern. Conf. on HEP, Vancouver, Canada (1998).

[81] M. Derrick *et al.* [ZEUS Collaboration], Phys. Lett. B **315** (1993) 481;
T. Ahmed *et al.* [H1 Collaboration], Nucl. Phys. B **429** (1994) 477.

[82] J. Collins, Phys. Rev. **D 57** (1998) 3051.

[83] G. Ingelman and P. Schlein, Phys. Lett. B **152** (1985) 256.

[84] C. Adloff *et al.* [H1 Collaboration], Z. Phys. C **76** (1997) 613.

[85] C. Adloff *et al.* [H1 Collaboration], Z. Phys. C **74** (1997) 221.

[86] C. Adloff *et al.* [H1 Collaboration], Phys. Lett. B **428** (1998) 206.

[87] C. Adloff *et al.* [H1 Collaboration], Eur. Phys. J. C **1** (1998) 495.

[88] C. Adloff *et al.* [H1 Collaboration], Eur. Phys. J. C **20** (2001) 29.

[89] K. Goulianos [CDF Collaboration], Nucl. Phys. Proc. Suppl. **99A** (2001) 37.

[90] B. E. Cox, K. Goulianos, L. Lonnblad and J. J. Whitmore, J. Phys. G **G26** (2000) 667.

[91] J. R. Forshaw and P.J. Sutton, Eur. Phys. J. C **1** (1998) 285.

[92] A. H. Mueller and W. K. Tang, Phys. Lett. B **284** (1992) 123.

[93] J. D. Bjorken, Phys. Rev. D **47** (1993) 101.

[94] M. Derrick *et al.* [ZEUS Collaboration], Phys. Lett. B **369** (1996) 55.

[95] H1 Collaboration, "Rapidity gaps between jets in Photoproduction at HERA", contribution to the International Europhysics Conference on High Energy Physics, August 1997, Jerusalem, Israel.

[96] B. Abbott *et al.* [D0 Collaboration], Phys. Lett. B **440** (1998) 189;
S. Abachi *et al.* [D0 Collaboration], Phys. Rev. Lett. **76** (1996) 734;
S. Abachi *et al.* [D0 Collaboration], Phys. Rev. Lett. **72** (1994) 2332.

[97] F. Abe *et al.* [CDF Collaboration], Phys. Rev. Lett. **81** (1998) 5278;
F. Abe *et al.* [CDF Collaboration], Phys. Rev. Lett. **80** (1998) 1156;
F. Abe *et al.* [CDF Collaboration], Phys. Rev. Lett. **74** (1995) 855.

[98] G. Oderda and G. Sterman, Phys. Rev. Lett. **81** (1998) 3591.

[99] B. E. Cox, J. Forshaw and L. Lonnblad, JHEP **9910** (1999) 023.

[100] B. E. Cox, Nucl. Phys. Proc. Suppl. **79** (1999) 315.

[101] G. Oderda, Phys. Rev. D **61** (2000) 014004.

[102] P. Bate, *High Transverse Momentum 2-Jet and 3-Jet Cross Section Measurements in Photoproduction*, Ph. D. thesis, University of Manchester (1999).

[103] M. Gluck, E. Reya and A. Vogt, Phys. Rev. D **46** (1992) 1973.

[104] M. Gluck, E. Reya and A. Vogt, Z. Phys. C **53** (1992) 127.

[105] S. D. Ellis and D. E. Soper, Phys. Rev. D **48** (1993) 3160.

Acknowledgements

There are many people that I would like to thank for their help and support throughout the course of my Ph.D. studies.

Firstly, I wish to thank my supervisor Robin Marshall for his encouragement in finding a thesis topic that I would enjoy and for giving me the both the support I needed and the freedom to follow my interests. Also, many thanks to Fred Loebinger for encouraging me to, eventually, start my Ph.D.

Special thanks must go to Brian Cox, with whom I have been working on this analysis. I have learnt a lot and it has been great fun to work with someone with such enthusiasm.

I would like to thank Jeff Forshaw and Mike Seymour for their many useful ideas and discussions that were essential in developing the theoretical basis for this analysis.

Thanks to Sergey Levonian, Pierre Van Mechelen, Peter Schleper, Steve Maxfield and Jacek Turnau for their patience and useful advice while we finished the analysis.

Many thanks to all those in Hamburg who made my time there such an enjoyable experience: Paul Bate, Anna Burrage, Beate Heinemann, John Kennedy, Paul Laycock, Nick Malden, Andy Mehta, Julian Phillips, Eram Rizvi, Dave South, Paul Thompson and Ben Waugh. I am also very grateful to Ben Waugh for reading my thesis.

Jamie Boyd, Steve Dallison, Tom Marchant and all the HEP group have helped make Manchester a great place to be.

Life throughout the course of my Ph.D. has been made richer through the love and friendship of William Venters.

Finally, I want to thank all my family, and in particular my parents, for their love and support through it all.